https://ntrs.nasa.gov/search.jsp?R=19710026872 2020-03-11T22:19:06+00:00Z

CONSTRUCTION AND TEST OF A DUAL PATCH MULTI-ELEMENT RADIANT COOLER

R. V. Annable and J. F. Lodder

ITT Aerospace/Optical Division
Electro-Optical Operations
Fort Wayne, Indiana 46803

SEP 1971
RECEIVED
NASA STI FACILITY
INPUT BRANCH

June 1971

Final Report for Period 17 September 1970 to 30 June 1971

Prepared for

GODDARD SPACE FLIGHT CENTER
Greenbelt, Maryland 20771

Reproduced by
NATIONAL TECHNICAL
INFORMATION SERVICE
Springfield, Va. 22151

FACILITY FORM 602

N71-36348 (ACCESSION NUMBER)
157 (PAGES)
CR-121854 (NASA CR OR TMX OR AD NUMBER)
(THRU)
G3 (CODE)
33 (CATEGORY)

1. Report No.	2. Government Accession No.	3. Recipient's Catalog No.
4. Title and Subtitle CONSTRUCTION AND TEST OF A DUAL PATCH MULTI-ELEMENT RADIANT COOLER		5. Report Date July 1971 6. Performing Organization Code
7. Author(s) R. V. Annable and J. F. Lodder		8. Performing Organization Report No.
9. Performing Organization Name and Address ITT Aerospace/Optical Division Electro-Optical Operations Fort Wayne, Indiana 46803		10. Work Unit No. 11. Contract or Grant No. NAS5-21132
12. Sponsoring Agency Name and Address Goddard Space Flight Center Greenbelt, Maryland 20771 I. L. Goldberg, Code 731		13. Type of Report and Period Covered Final 17 Sept 1970 - 30 June 1971 14. Sponsoring Agency Code
15. Supplementary Notes		

16. Abstract

This report covers the construction and test of the dual patch multi-element radiant cooler described in the design study report of July 1970. During test, the patch temperatures were 112K and 95K for the InAs and HgCdTe arrays, respectively. A change in design was needed to obtain the second temperature. Cooler and other tests showed that the multilayer blankets had insulation factors from 60 to 65 and that the effective cone wall emissivity was about 0.04. Other measurements confirmed the theoretical predictions on the radiative decoupling between low-emissivity surfaces. Supporting studies revealed the need for optically finished (highly specular) cone walls. They also showed that orbital operating time is limited by contamination from the spacecraft atmosphere. Improvements in the space target and additional measurements on the cone walls are needed to improve testing accuracy.

17. Key Words	18. Distribution Statement		
19. Security Classif. (of this report)	20. Security Classif. (of this page)	21. No. of Pages	22. Price

PRECEDING PAGE BLANK NOT FILMED

PREFACE

This report covers the construction and test of a dual patch multi-element radiant cooler for earth oriented applications. The thermal and mechanical design of the cooler are described in the study report of July 1970. The cooler attained patch temperatures of 112K and 95K in tests simulating operation in a circular 9:30 AM orbit at an altitude of 450 n mi. The construction was made realistic by including (a) a dual patch assembly that survived sinusoidal vibration at 20 G's, (b) electrical and optical connections for a 14 element InAs array at the higher temperature and a 4 element HgCdTe array at the lower temperature, and (c) anti-frost devices. The tests were made realistic by including (a) an outgassing period, (b) a cone thermal load equal to the in-orbit value, and (c) a non-black space target that produced an input at least as great as the in-orbit input from the diffuse cone coupling of the earth and cooler patches. Analysis of the tests showed that the cone and warmer patch had (rear area) insulation factors from 60 to 65. However, a change in the design was needed to obtain sufficient radiative insulation of the cooler patch. The effective specular emissivity of the cone walls was estimated to be 0.04. Emissivities in this vicinity were also obtained in separate tests on a special cone.

The construction and test of the radiant cooler were supported by theoretical and experimental studies of cone surfaces, radiative insulation, and anti-frost techniques. The first study demonstrated the need for optically finished cone walls to provide highly specular surfaces. A non-specular component of wall reflection increases the cone to patch radiative coupling and provides an indirect earth to patch coupling during orbital operation. Separate tests of insulation blankets confirmed the results obtained during the cooler tests. In addition, tests of close-spaced low-emissivity surfaces of emissivity ϵ showed that they had the expected insulation factor of $2/\epsilon$. The anti-frost study revealed that the time between decontaminations in a properly designed and operated radiant cooler is limited by contamination from the spacecraft atmosphere.

Finally, improvements in the space target and measurements of the non-specular cone reflections (infrared and solar) are recommended to improve the accuracy and confidence level of the thermal testing.

Dual Patch Radiant Cooler Summary

	Patch 1[a]	Patch 2[b]
Temperature	112.4 K	92.5 K
Power Radiated	35.5 mW	16.3 mW
Radiator Area	6.4 in^2	6.4 in^2
Conductive Input Power	14.9 mW	2.8 mW
Cone Radiant Input Power	5.5 mW	4.0 mW
Radiant Input Through Multilayer[c]	11.0 mW	2.6 mW
Radiant Input Through Optics	3.1 mW	3.1 mW
dT/dP	0.74 K/mW	1.18 K/mW

	Housing	Shield	Cone
Temperature	24.6°C	14.0°C	178.6 K
Surface Material	Anodize	Electroless Ni[d]	Electroless Ni[d]
Structural Material	6061-T6A1	6061-T6A1	6061-T6A1

Cooler Overall Dimensions	12" x 8.5" x 11" with shield deployed
Cooler Weight	10 lbs

Note: dT/dP is the rate of change of patch temperature with input power at the patch temperature shown above.

(a) The balance of 1.0 mW is estimated to be 3.8 mW from the non-black space target minus 2.8 mW lost to patch 2 by conduction.

(b) The balance of 3.8 mW is estimated to be the radiant input from the non-black space target. The addition of 2 mW bias power would increase the patch temperature to 95 K.

(c) Input to patch 1 includes that to the attached shield; input to patch 2 includes that from the shield attached to patch 1.

(d) Inner surfaces optically polished and over coated with chromium and gold.

TABLE OF CONTENTS

		Page
1.0	CONSTRUCTION	1-1
1.1	Mechanical Design	1-4
1.2	Cone Surface Properties	1-61
1.2.1	Directional Emissivity of a Metallic Reflector	1-62
1.2.2	Relation Between Surface Roughness and Specular Reflectance	1-67
1.2.3	References	1-72
1.3	Anti-Frost Design	1-74
1.3.1	Outgassing of Patch Insulation	1-76
1.3.2	Trapping of Spacecraft Contaminants	1-78
1.3.3	Anti-Frost Devices	1-79
1.3.4	Optical Port Design	1-81
1.3.5	Multilayer Insulation - A Review	1-82
2.0	TEST	2-1
2.1	Radiant Cooler Thermal Tests	2-2
2.2	Analysis of Cooler Tests	2-9
2.2.1	Cone Insulation	2-10
2.2.2	Patch Conductive Coupling	2-11
2.2.3	Patch Radiative Coupling	2-14
2.2.4	The Effects of a Diffuse Component of Cone Wall Reflection	2-18
2.3	Chamber Test Equipment	2-21
2.3.1	Cold Targets	2-21
2.3.2	Heaters	2-22
2.3.3	Corrections for the Non-Black Space Target	2-24
2.4	Radiative Insulation Tests	2-29
2.4.1	Multilayer Insulation Tests	2-29
2.4.2	Radiative Decoupling	2-34
2.5	Cone Emissivity Measurements	2-39
2.5.1	Effective Cone Wall Emissivity	2-39
2.5.2	Hemispherical Emissivity	2-47
2.6	Analysis of Emissivity Measurements	2-50
2.6.1	Estimate of Emissivity Increase	2-50
2.6.2	Sensitivity of Cone Designs to Diffuse Reflection	2-51
3.0	NEW TECHNOLOGY	3-1
4.0	RECOMMENDATIONS	4-1
5.0	CONCLUSIONS	5-1
APPENDIX	SPECIFICATION FOR COOLER CONE WALL PROCESSING	A-1

LIST OF ILLUSTRATIONS

		Page
Figure 1-1	Dual Patch Multi-Element Radiant Cooler	1-2
Figure 1-2	Front View of Cooler Showing Image Arrays of Dual Patch and Cone Radiator	1-3
Figure 1-3	Vibration Fixture and Dual Patch Assembly	1-5
Figure 1-4	MERC Radiant Cooler Assembly	1-10
Figure 1-5	Housing, Front Plate - Assembly	1-11
Figure 1-6	Plate, Support - Cold Space Target	1-12
Figure 1-7	Shroud, Thermo - LN2	1-13
Figure 1-8	Plate, Back - Shield	1-14
Figure 1-9	Shield Assembly	1-15
Figure 1-10	Plate, Back-Cone Housing	1-16
Figure 1-11	Plate, Bottom - Cone Housing	1-17
Figure 1-12	Plate, Top-Cone Housing	1-18
Figure 1-13	Plate, Serrated	1-19
Figure 1-14	Patch, 120 Degrees	1-20
Figure 1-15	Patch, 90 Degrees	1-21
Figure 1-16	Plate, Housing Back	1-22
Figure 1-17	Plate, Housing Bottom	1-23
Figure 1-18	Plate, Housing Top	1-24
Figure 1-19	Housing Assembly Cone	1-25
Figure 1-20	Cone, 45 degrees LA Cooler	1-26
Figure 1-21	Cooler Assembly, 45 Degree Angle	1-27
Figure 1-22	Actuator Assembly	1-28
Figure 1-23	Plate, Face-Cold Space Target	1-29
Figure 1-24	Plate, Slide-Cold Space Target	1-30
Figure 1-25	Suspension-Dual Patch	1-31
Figure 1-26	Patch Assembly	1-32
Figure 1-27	Plate, Side-MERC Cone	1-33
Figure 1-28	Plate, Back-MERC Cone	1-34
Figure 1-29	Cone Assembly MERC	1-35
Figure 1-30	Plate, Side-Shield	1-36
Figure 1-31	Cover, Side-Cone Housing, Left	1-37
Figure 1-32	Cover, Side-Cone Housing, Right	1-38
Figure 1-33	Cone, Anti-Icing, 90 Degrees K	1-39
Figure 1-34	Mount, 90 Degree Anti-Icing Cone	1-40
Figure 1-35	Cone Assembly - Anti-Icing 90 Degrees K	1-41
Figure 1-36	Cone - Anti-Icing 120 Degrees K	1-42
Figure 1-37	Mount, 120 Degrees Anti-Icing Cone	1-43
Figure 1-38	Cone Assembly, Anti-Icing, 120 Degrees K	1-44
Figure 1-39	Retainer, Irtran 2 Window	1-45
Figure 1-40	Retainer, Iratran 2 Window	1-46
Figure 1-41	Plate Side-Actuator	1-47
Figure 1-42	Plate, Support - 45 Degree LA Cooler	1-48

LIST OF ILLUSTRATIONS (Cont.)

		Page
Figure 1-43	Patch - 45 Degree LA Cooler	1-49
Figure 1-44	Plate, Cone Wall - 45 Degree LA Cooler	1-50
Figure 1-45	Block, Tapered - Patch Support MERC	1-51
Figure 1-46	Clamp - Patch Support MERC	1-52
Figure 1-47	Ring, Lens Retainer	1-53
Figure 1-48	Foot Mounting MERC	1-54
Figure 1-49	Baffle, Insulation	1-55
Figure 1-50	Plate, End Actuator	1-56
Figure 1-51	Bracket, Bottom - 45 Degree LA Cooler	1-57
Figure 1-52	Tube, Support - 45 Degree LA Cooler	1-58
Figure 1-53	Bracket, Top - 45 Degree LA Cooler	1-59
Figure 1-54	Angle, Support - 45 Degree LA Cooler	1-60
Figure 1-55	Reflectance Distribution Curves	1-70
Figure 1-56	Anti-Frost Design	1-80
Figure 2-1	Thermal Test No. 3	2-5
Figure 2-2	Thermal Test No. 7	2-8
Figure 2-3	Multilayer Insulation Test Apparatus	2-30
Figure 2-4	Multilayer Insulation Test Fixture Modification 1	2-33
Figure 2-5	Patch Support and Coaxial Shield	2-38
Figure 2-6	Insulation Box and Support Enclosure	2-40
Figure 2-7	Polished, Hard Coated Aluminum Inner Surfaces of Cone	2-41
Figure 2-8	Cone Wall Base For Emissionmeter (Dimensions in Inches)	2-48

LIST OF TABLES

		Page
Table 1-1	Dual Patch Assembly Resonant Frequencies	1-4
Table 1-2	Directional Emissivity of UHV Aluminum	1-65
Table 1-3	Partial Hemispherical Emissivity of UHV Aluminum	1-66
Table 1-4	Surface Quality Required For Specified Specularity	1-66
Table 1-5	Fraction of Cone Wall Radiation Beyond 20 μm	1-71
Table 1-6	Required Surface Irregularity in the Visible For Specified Specularity at 20 μm	1-71
Table 1-7	Time to Saturate a Cold Trap with a 0.1 cm Gap	1-79
Table 2-1	Thermal Test 1	2-2
Table 2-2	Thermal Test 2	2-3
Table 2-3	Thermal Test 3	2-4
Table 2-4	Thermal Test 4	2-6
Table 2-5	Thermal Test 5	2-6
Table 2-6	Thermal Test 6	2-7
Table 2-7	Thermal Test 7	2-9
Table 2-8	Connections Between Housing and Cone	2-10
Table 2-9	Connections Between Cone and Patch 1	2-12
Table 2-10	Connections Between Patches	2-12
Table 2-11	Heater Circuit Parameters	2-13
Table 2-12	Total Patch-Cone Radiative Coupling for Patch 1	2-14
Table 2-13	Corrected Radiative Coupling Factors for Patch 1	2-15
Table 2-14	Total Patch-Cone Radiative Coupling for Patch 2	2-16
Table 2-15	Corrected Values of Cone Coupling Factors from Second Patch	2-17
Table 2-16	Cone Heater Power and Voltage Requirements	2-23
Table 2-17	Patch Heater Power and Voltage Requirements	2-24
Table 2-18	Hemispherical Emissivity of Honeycomb Cavity	2-25
Table 2-19	Space Target Surface Reflectivity	2-26
Table 2-20	Patch 2 Temperature Increase Produced by a Non-Black Space Target	2-28
Table 2-21	Multilayer Insulation Tests in Modified Fixture	2-34
Table 2-22	Results of Insulation Tests	2-34
Table 2-23	Test Measurements	2-36
Table 2-24	Emissivity of Gold Surfaces	2-37
Table 2-25	Test Cone Measurements	2-44
Table 2-26	Determination of ϵ_p and S_i	2-44
Table 2-27	Cone Wall Emissivities	2-45
Table 2-28	Hemispherical Emissivity Measurements	2-49
Table 2-29	Apparent Cone Wall Emissivity	2-53
Table 2-30	Required Surface Flatness	2-54
Table 2-31	Ratio of Effective to Hemispheric Emissivity for Specular Reflection	2-55

LIST OF TABLES (Cont.)

Page

Table 2-32 View Factors from the Patch ---------- 2-56
Table 2-33 Efficiency of Patch Emission for Diffuse Cone Reflection-------- 2-57
Table 2-34 Degradation Factor for Cone Wall Radiative Coupling ---------- 2-57

1.0 CONSTRUCTION

The assembled dual patch multi-element radiant cooler is shown in Figures 1-1 and 1-2. In the first photograph, we can see part of one reflection of the dual patch in the (upper) cone and of the cone end in the (lower) earth shield. The second photograph shows at least part of all five reflections (three first reflections and two second) of both the patches and cone end. The construction of the cooler is based on the results of the design study (report of July 1970 covering the period from 16 February to 16 July 1970).

The mechanical design of the radiant cooler is described in a set of detail and assembly drawings (Section 1.1). The soundness of the mechanical design was verified by sinusoidal vibration tests on the dual patch assembly.

The design and construction of the cooler were supported by studies of cone surface properties (Section 1.2) and of anti-frost requirements (Section 1.3). The first study revealed the need for optical finishing of the inner cone wall surfaces (Appendix). The second study showed that the anti-frost enclosures (Section 6.3) of the design study report should be replaced with cold traps. In addition, the second study showed that the operating time (between decontaminations) would be limited by contamination from the spacecraft atmosphere in a properly constructed and properly operated radiant cooler.

NOT REPRODUCIBLE

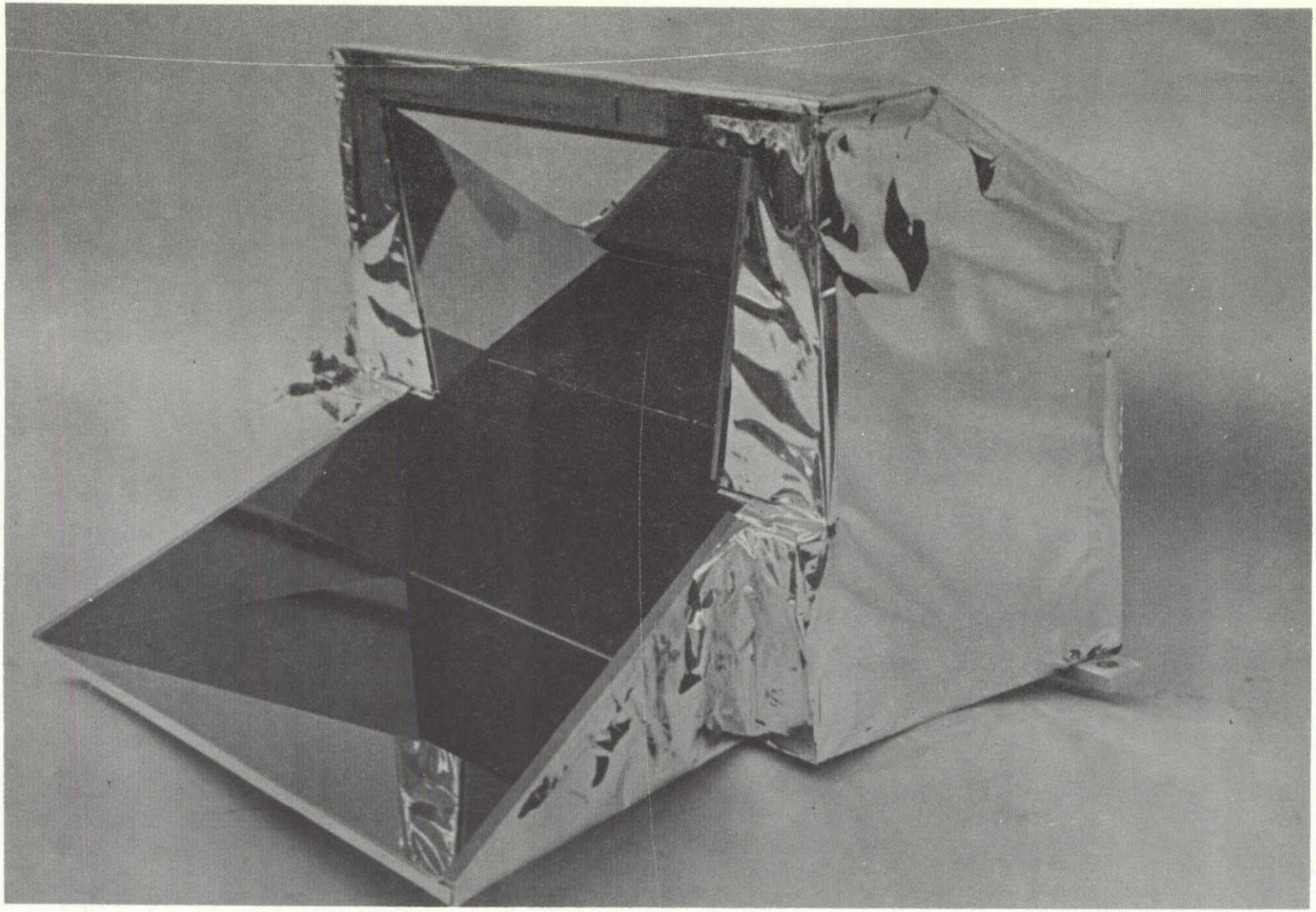

Figure 1-1 Dual Patch Multi-Element Radiant Cooler

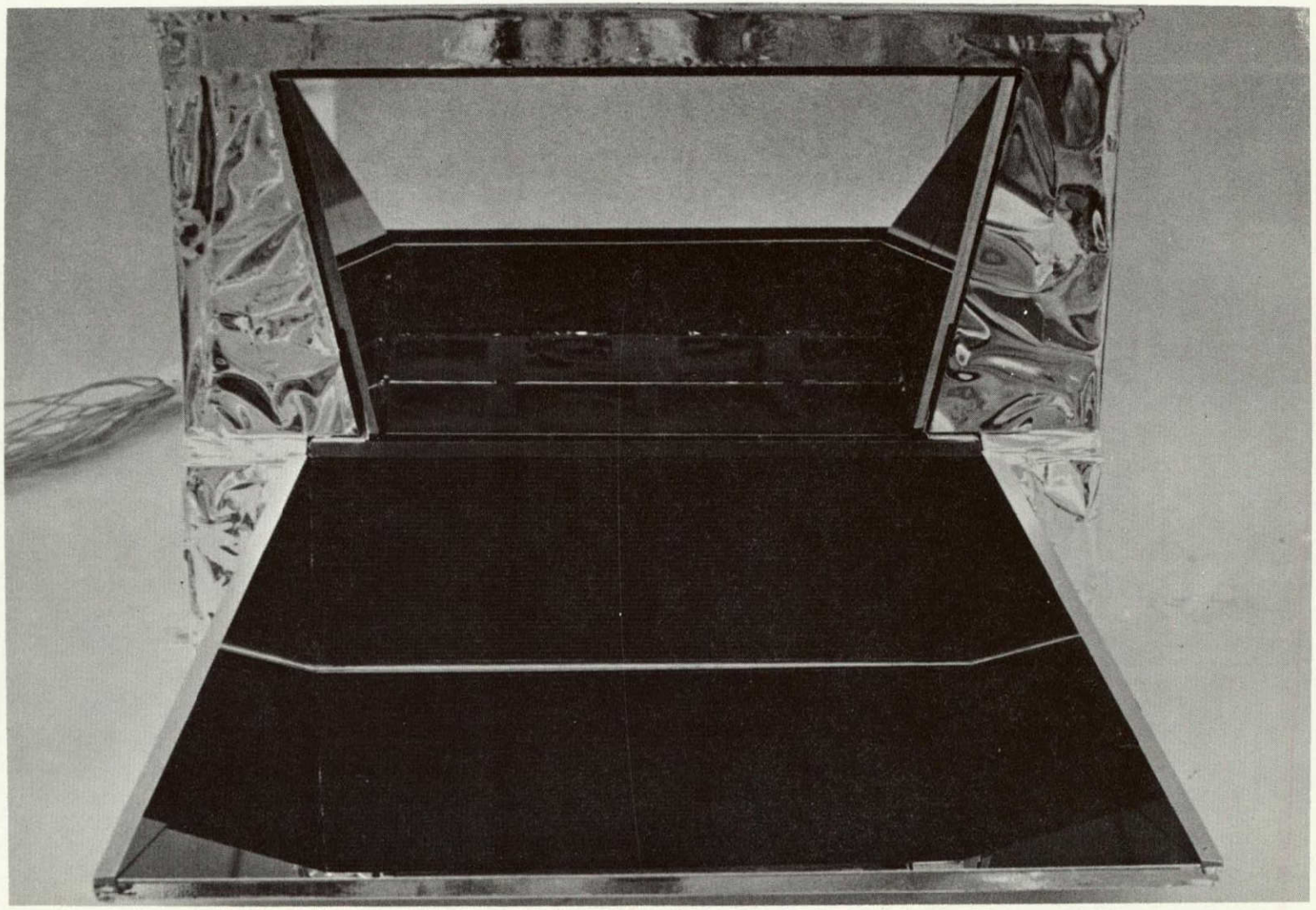

NOT REPRODUCIBLE

Figure 1-2 Front View of Cooler Showing Image Arrays of Dual Patch and Cone Radiator

1.1 Mechanical Design

The mechanical designs of the breadboard radiant cooler and the chamber cold targets are given in the detail and assembly drawings reproduced in this section. The drawings are preceded by a complete index list.

The design of the cone cover actuator was changed from that described in section 6.2 of the design study report (July 1970). The new design is shown in drawings 8114000 and 8338428. The liquid lubrication was eliminated, the electric motor was replaced with a linear solenoid using dry film lubrication, the previous bearings were replaced with no-lube teflon urethane bearings, and the gears modified to alternately mesh aluminum with self-lubricated fiber impregnated polyurethane.

A fixture for the patch vibration test was designed and fabricated, as shown in Figure 1-3 . The patch configuration is the same as that in the thermal test model. The vibration test was sinusoidal, 5 to 2000 hz, 1 octave per minute, and 20 G's for all three axes. One of the four support tubes to the first (120K) patch was found to be loose after completion of the roll axis vibration. The tube was re-cemented and the pitch axis vibration completed without incident. The total vibration time for the three axis was about 30 minutes. Resonant frequencies were noted in each axis as shown in Table 1-1 .

Table 1-1

Dual Patch Assembly Resonant Frequencies

Axis	Frequencies (Hz)
Yaw	105
Roll	30, 85
Pitch	80, 100

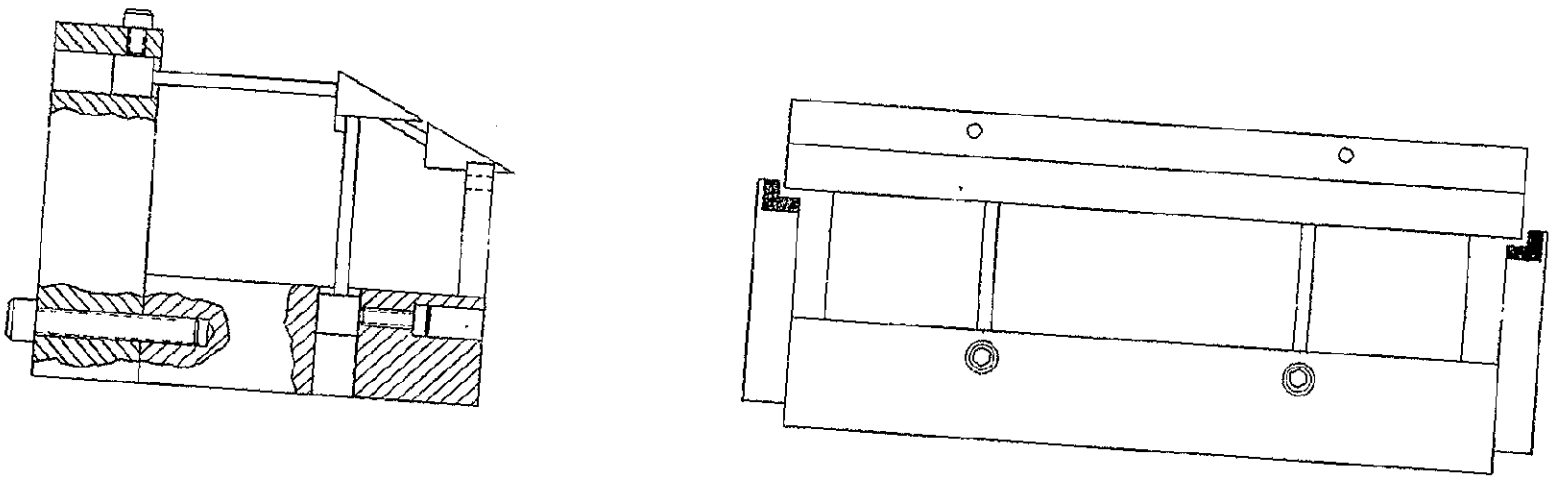

Figure 1-3 Vibration Fixture and Dual Patch Assembly

INDEX LIST

ITT AEROSPACE/OPTICAL DIVISION
FORT WAYNE, INDIANA, U.S.A.
INTERNATIONAL TELEPHONE AND TELEGRAPH CORPORATION

CONTRACT NO. NAS5-21132

CODE IDENT NO. 31550

IL 8114038

REVISION LTR DATE

LIST TITLE: DUAL PATCH MULTI-ELEMENT RADIANT COOLER

AUTHENTICATION

REV AUTH NO.

SHT 1 OF 4 SHTS

CODE IDENT NO.	DWG SIZE	LIST NUMBER	REV LTR	LIST TITLE	NO. SHTS	SYM	LINE NO.
31550	E	8114038		MERC Radiant Cooler Assy			1
	E	8116240		Housing, Front Plate - Assy			2
	D	8114041		Plate, Support - Cold Space Target			3
	D	8114049		Shroud, Thermo - LN_2			4
	D	8116056		Plate, Back - Shield			5
	D	8116058		Shield Assy			6
	D	8116060		Plate, Back - Cone Housing			7
	D	8116061		Plate, Bottom - Cone Housing			8
	D	8116062		Plate, Top - Cone Housing			9
	D	8116065		Plate, Serrated			10
	D	8116066		Patch, 120°			11
	D	8116067		Patch, 90°			12
	D	8116237		Plate, Housing Back			13
	D	8116238		Plate, Housing Bottom			14
	D	8116241		Plate, Housing Top			15
	D	8116242		Housing Assy - Cone			16

INDEX LIST	ITT AEROSPACE/OPTICAL DIVISION FORT WAYNE, INDIANA, U.S.A. INTERNATIONAL TELEPHONE AND TELEGRAPH CORPORATION	CONTRACT NO. NAS5-21132	CODE IDENT NO. 31550	IL 8114038	REVISION LTR DATE

LIST TITLE	AUTHENTICATION	REV AUTH NO.	SHT 2 OF 4 SHTS
MERC			

CODE IDENT NO.	DWG SIZE	LIST NUMBER	REV LTR	LIST TITLE	NO. SHTS	SYM	LINE NO.
31550	C	8113990		Cone, 45° L.A. Cooler			1
	C	8113998		Cooler Assy, 45° Angle			2
	C	8114000		Actuator Assy			3
	C	8114044		Plate, Face - Cold Space Target			4
	C	8114045		Plate, Side - Cold Space Target			5
	C	8114057		Suspension - Dual Patch			6
	C	8114058		Patch Assembly			7
	C	8116052		Plate, Side - MERC Cone			8
	C	8116053		Plate, Back - MERC Cone			9
	C	8116054		Cone Assy - MERC			10
	C	8116055		Plate, Side - Shield			11
	C	8116063		Cover, Side - Cone Housing, Left			12
	C	8116064		Cover, Side - Cone Housing, Right			13
	C	8116070		Cone, Anti-Icing, 90°K			14
	C	8116071		Mount, 90° Anti-Icing Cone			15
	C	8116230		Cone Assy - Anti-Icing, 90°K			16

FORM NO. FW ITTAOD D113 SYMBOL:

LINCOLN-GRAPHIC CORP 10 5155 500 6-69

INDEX LIST

ITT AEROSPACE/OPTICAL DIVISION
FORT WAYNE, INDIANA, U.S.A.
INTERNATIONAL TELEPHONE AND TELEGRAPH CORPORATION

CONTRACT NO. NAS5-21132

CODE IDENT NO. 31550

IL 8114038

REVISION LTR DATE

LIST TITLE: MERC

AUTHENTICATION

REV AUTH NO.

SHT 3 OF 4 SHTS

CODE IDENT NO.	DWG SIZE	LIST NUMBER	REV LTR	LIST TITLE	NO. SHTS	SYM	LINE NO.
31550	C	8116231		Cone - Anti-Icing 120°K			1
	C	8116232		Mount, 120° Anti-Icing Cone			2
	C	8116233		Cone Assy - Anti-Icing, 120°K			3
	C	8116235		Retainer, Irtran 2 Window			4
	C	8116236		Retainer, Irtran 2 Window			5
	C	8338428		Plate Side - Actuator			6
	B	8113992		Plate, Support - 45° L.A. Cooler			7
	B	8113994		Patch - 45° L.A. Cooler			8
	B	8113997		Plate, Cone Wall - 45° L.A. Cooler			9
	B	8116068		Block, Tapered - Patch Support MERC			10
	B	8116069		Clamp - Patch Support, MERC			11
	B	8116234		Ring, Lens Retainer			12
	B	8116239		Foot Mtg - MERC			13
	B	8116243		Baffle, Insulation			14
	B	8338429		Plate, End - Actuator			15
							16

INDEX LIST

ITT AEROSPACE/OPTICAL DIVISION
FORT WAYNE, INDIANA, U.S.A.
INTERNATIONAL TELEPHONE AND TELEGRAPH CORPORATION

CONTRACT NO. NAS5-21132

CODE IDENT NO. 31550

IL 8114038

REVISION
LTR
DATE

LIST TITLE: MERC

AUTHENTICATION

REV AUTH NO.

SHT 4 OF 4 SHTS

CODE IDENT NO.	DWG SIZE	LIST NUMBER	REV LTR	LIST TITLE	NO. SHTS	SYM	LINE NO.
31550	A	8113991		Bracket, Bottom - 45° L.A. Cooler			1
	A	8113993		Tube, Support - 45° L.A. Cooler			2
	A	8113995		Bracket, Top - 45° L.A. Cooler			3
	A	8113996		Angle, Support - 45° L.A. Cooler			4
							5
							6
							7
							8
							9
							10
							11
							12
							13
							14
							15
							16

FORM NO. FW ITTAOD D113

SYMBOL:

LINCOLN-GRAPHIC CORP
10 5155 500 6-69

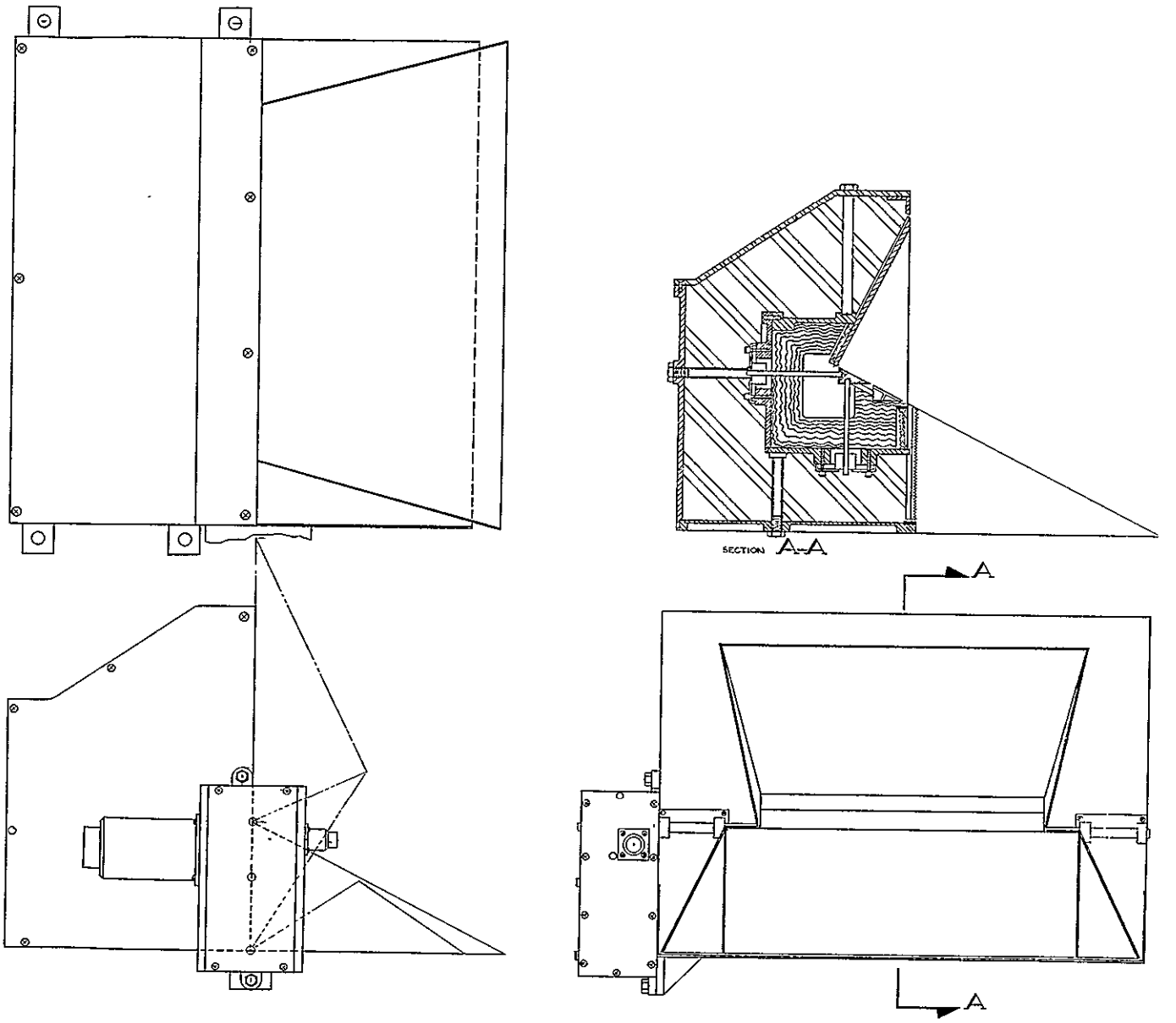

Figure 1-4 MERC Radiant Cooler Assembly 8114038

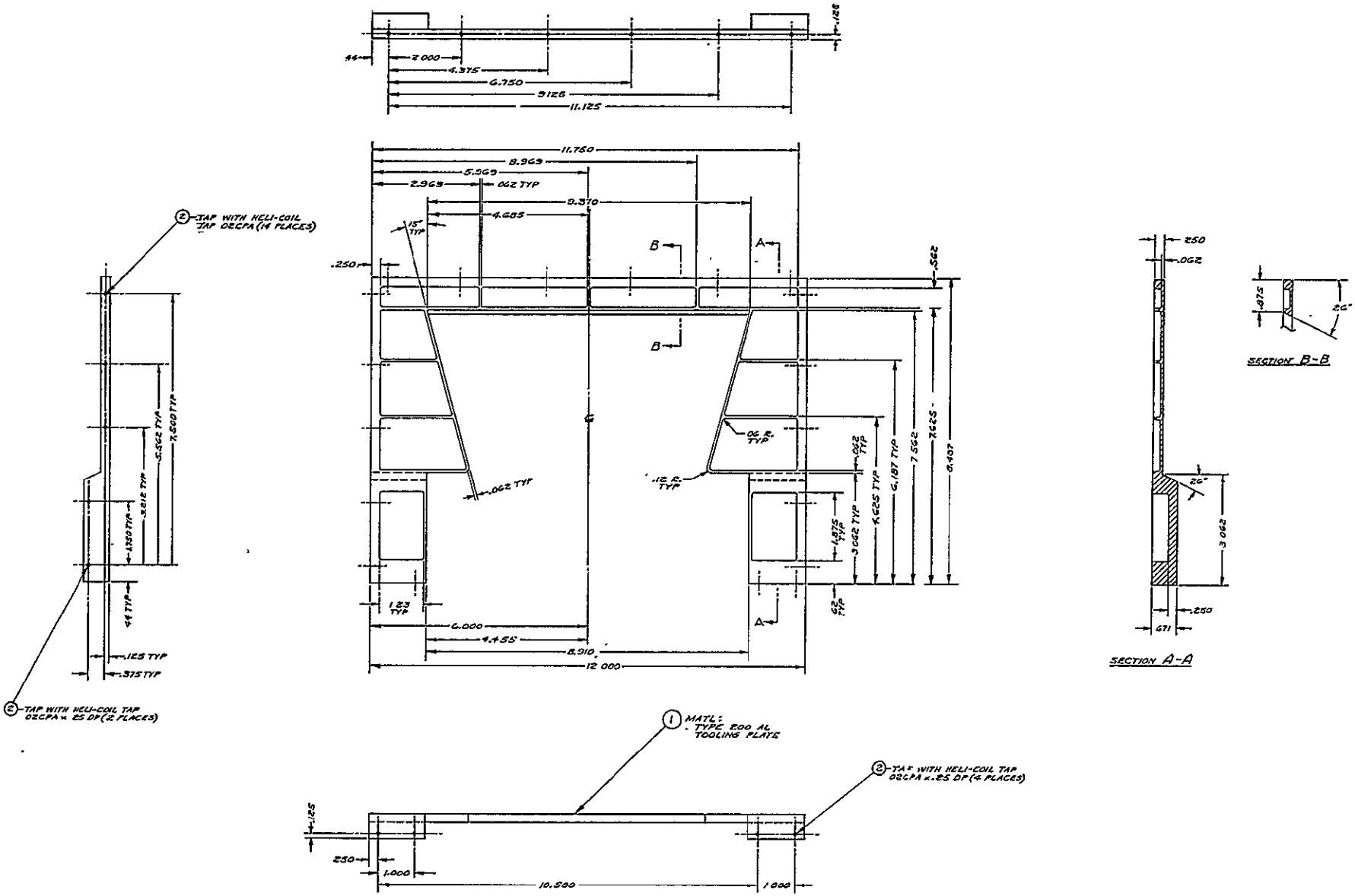

Figure 1-5 Housing, Front Plate - Assembly 8116240

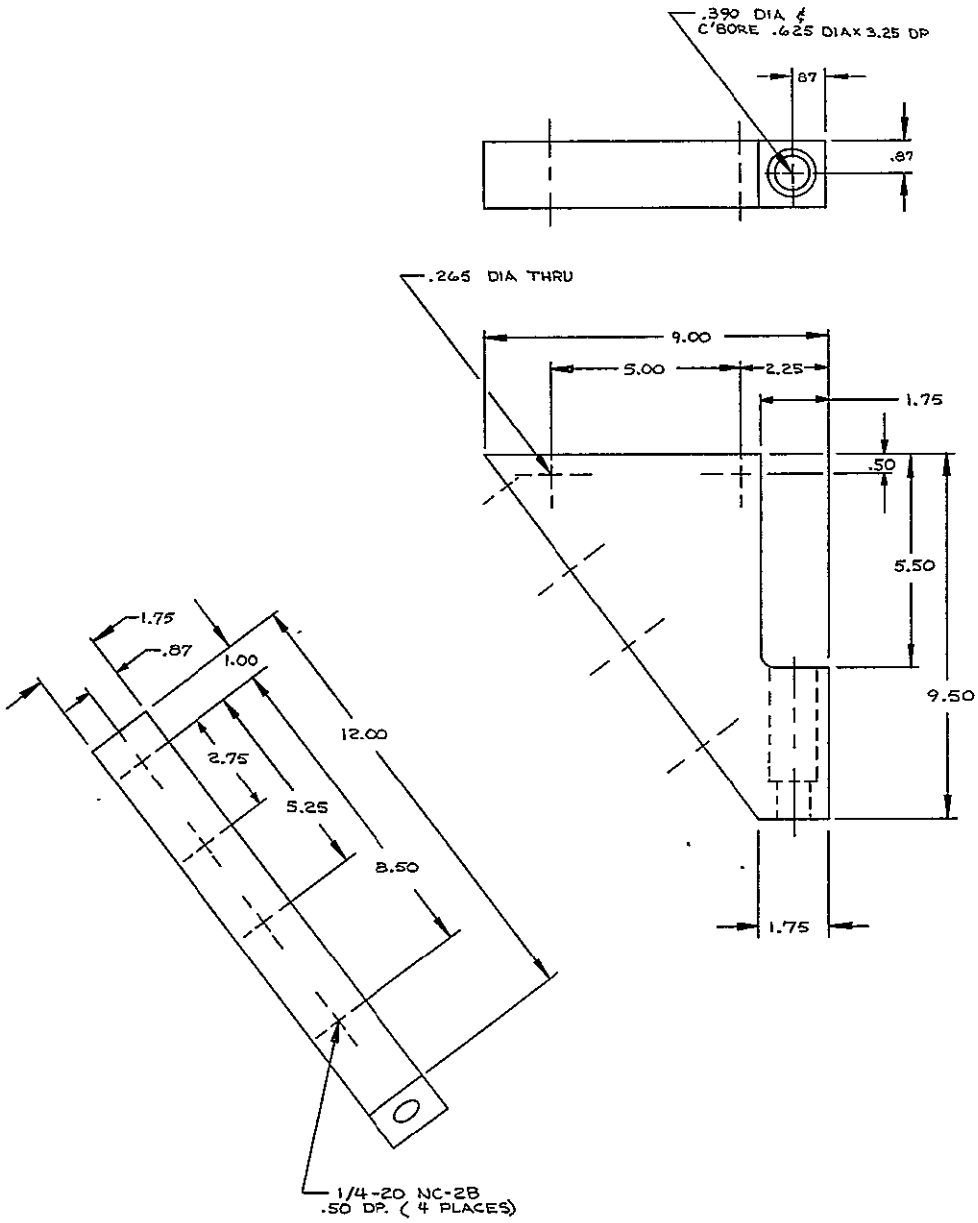

Figure 1-6 Plate, Support - Cold Space Target 8114041

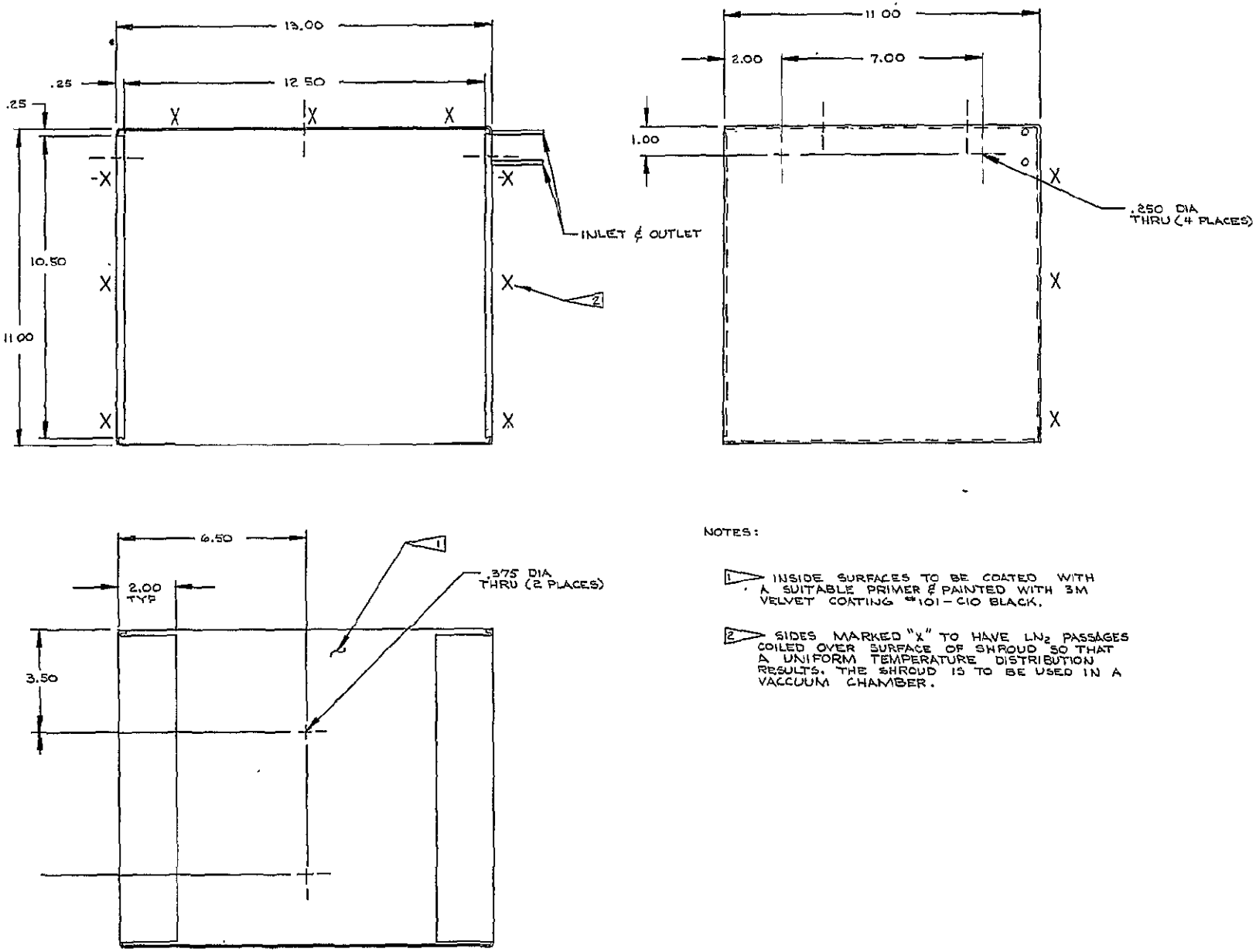

NOTES:

1. INSIDE SURFACES TO BE COATED WITH A SUITABLE PRIMER & PAINTED WITH 3M VELVET COATING #101-C10 BLACK.

2. SIDES MARKED "X" TO HAVE LN_2 PASSAGES COILED OVER SURFACE OF SHROUD SO THAT A UNIFORM TEMPERATURE DISTRIBUTION RESULTS. THE SHROUD IS TO BE USED IN A VACCUUM CHAMBER.

Figure 1-7 Shroud, Thermo - LN2

8114049

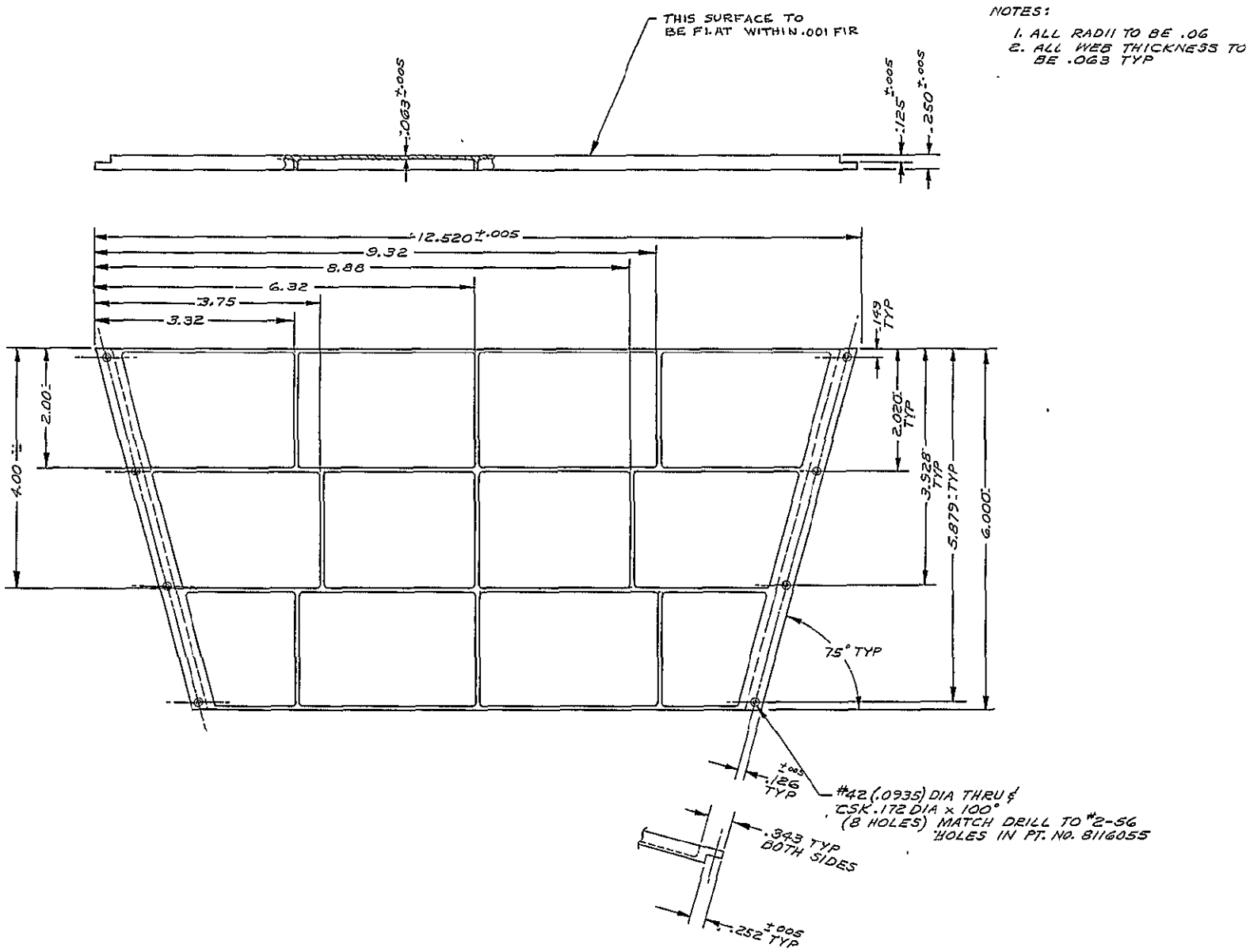

Figure 1-8 Plate, Back - Shield 8116056

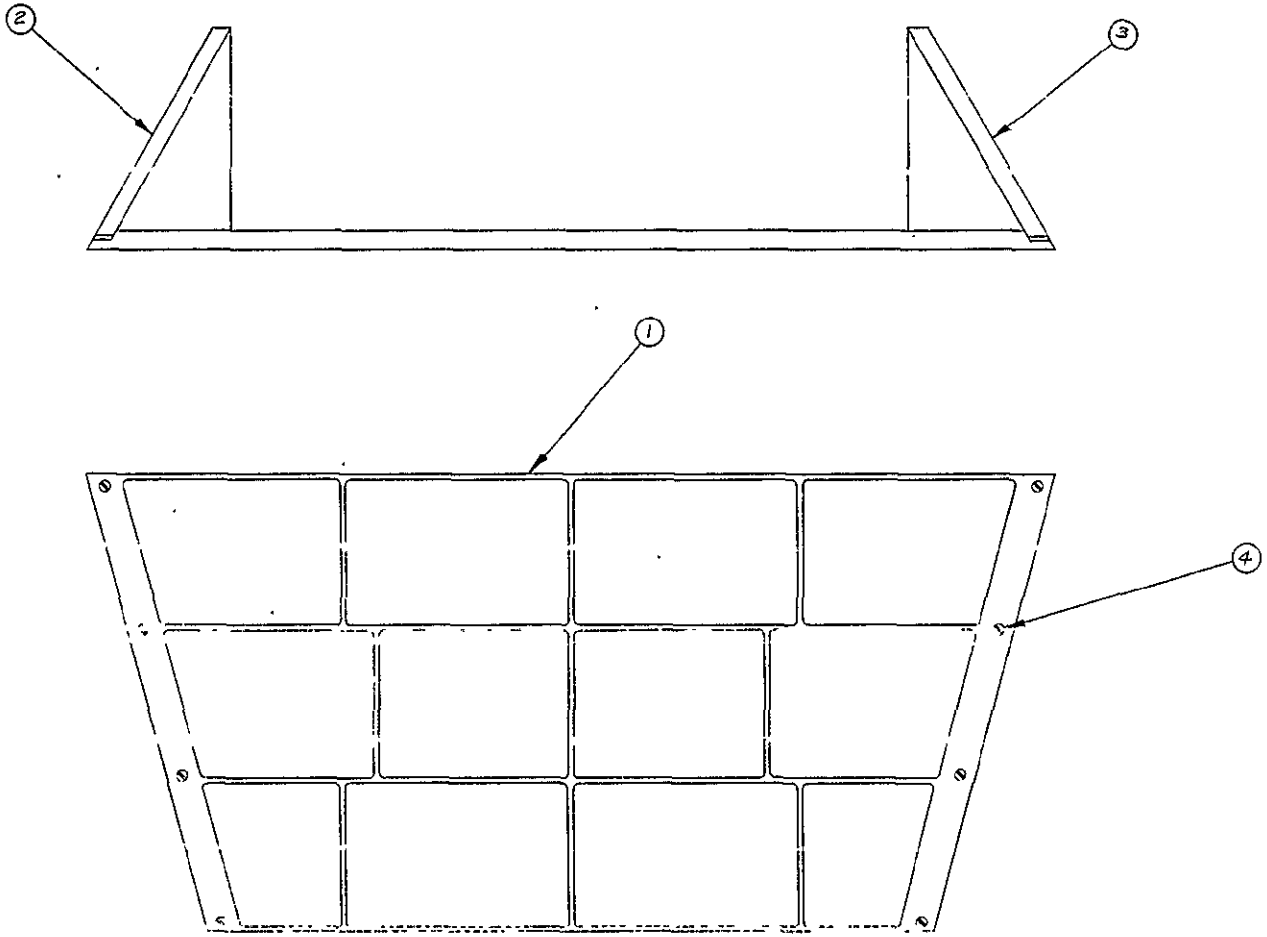

8	4		Y3-2-V	SCREW, FL HD(#2-56x3/8) PIC
1	3	C	8116055-2	PLATE, SHIELD SIDE
1	2	C	8116055-1	PLATE, SHIELD SIDE
1	1	D	8116056	PLATE, SHIELD BACK

Figure 1-9 Shield Assembly 8116058

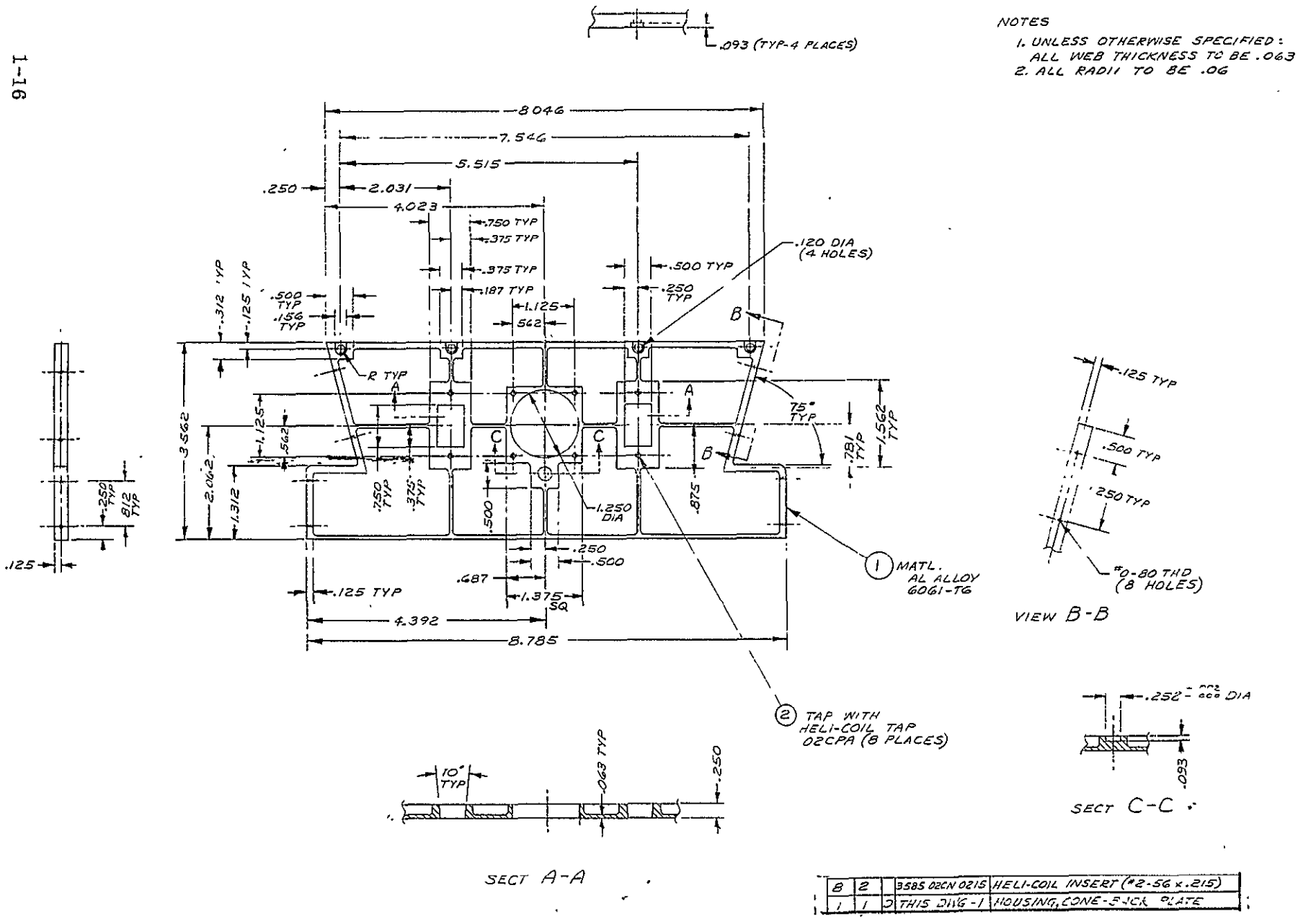

Figure 1-10 Plate, Back-Cone Housing 8116060

NOTES:
1. ALL RADII TO BE .06
2. ALL WEB THICKNESS TO BE .063

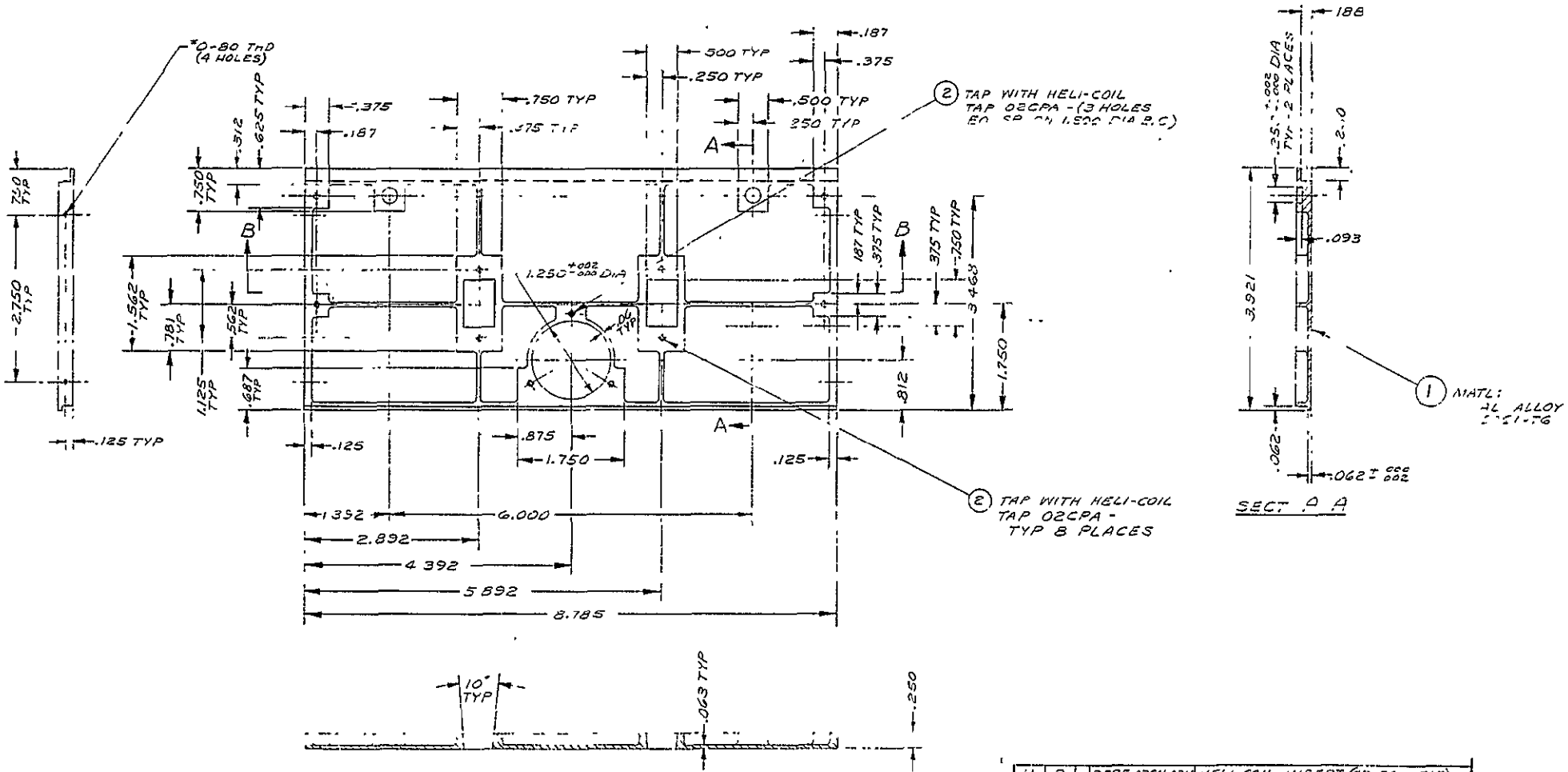

11	2		3585 02CN 0215	HELI-COIL INSERT (#2-56 x .215)
1	1	D	THIS DWG-1	HOUSING, CONE-BOTTOM PLATE

Figure 1-11 Plate, Bottom - Cone Housing

8116061

NOTES:

1. UNLESS OTHERWISE SPECIFIED: ALL WEB THICKNESS TO BE .063
2. ALL RADII TO BE .06

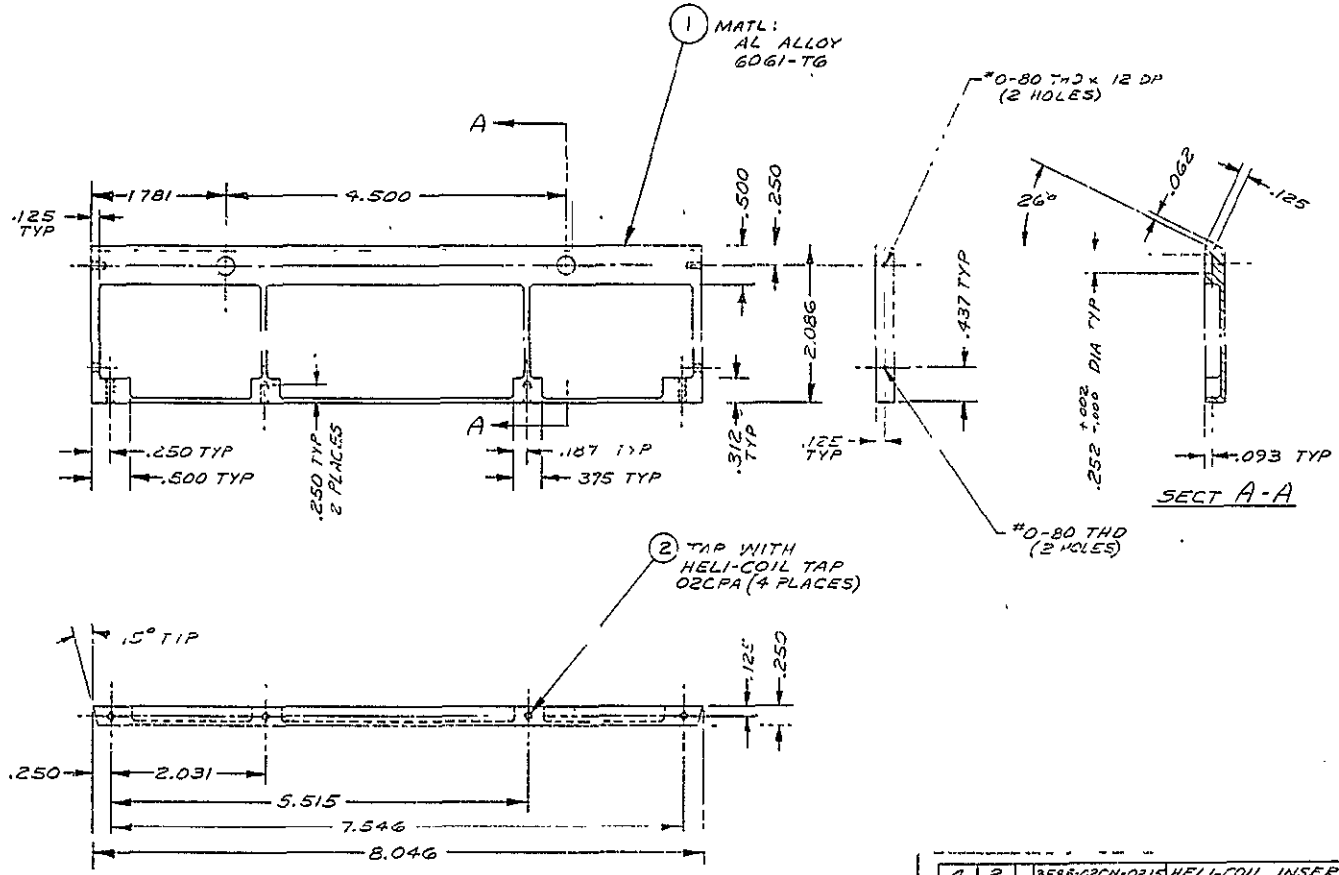

4	2		3585-02CN-0215	HELI-COIL INSERT
1	1	D	THIS DWG-1	HOUSING, CONE-TOP PLATE

Figure 1-12 Plate, Top-Cone Housing 8116062

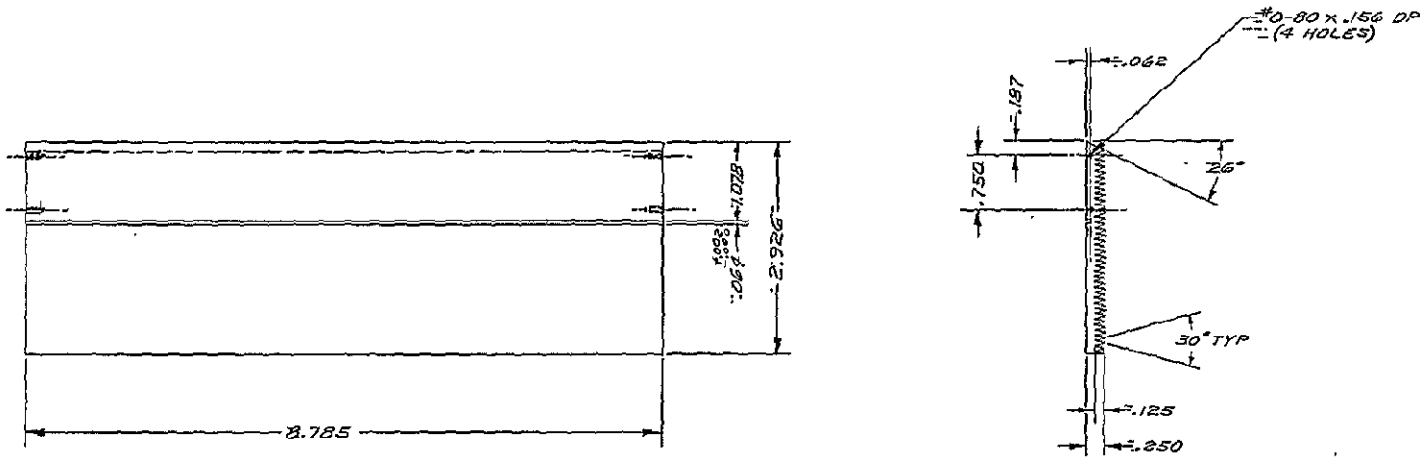

Figure 1-13 Plate, Serrated

8116065

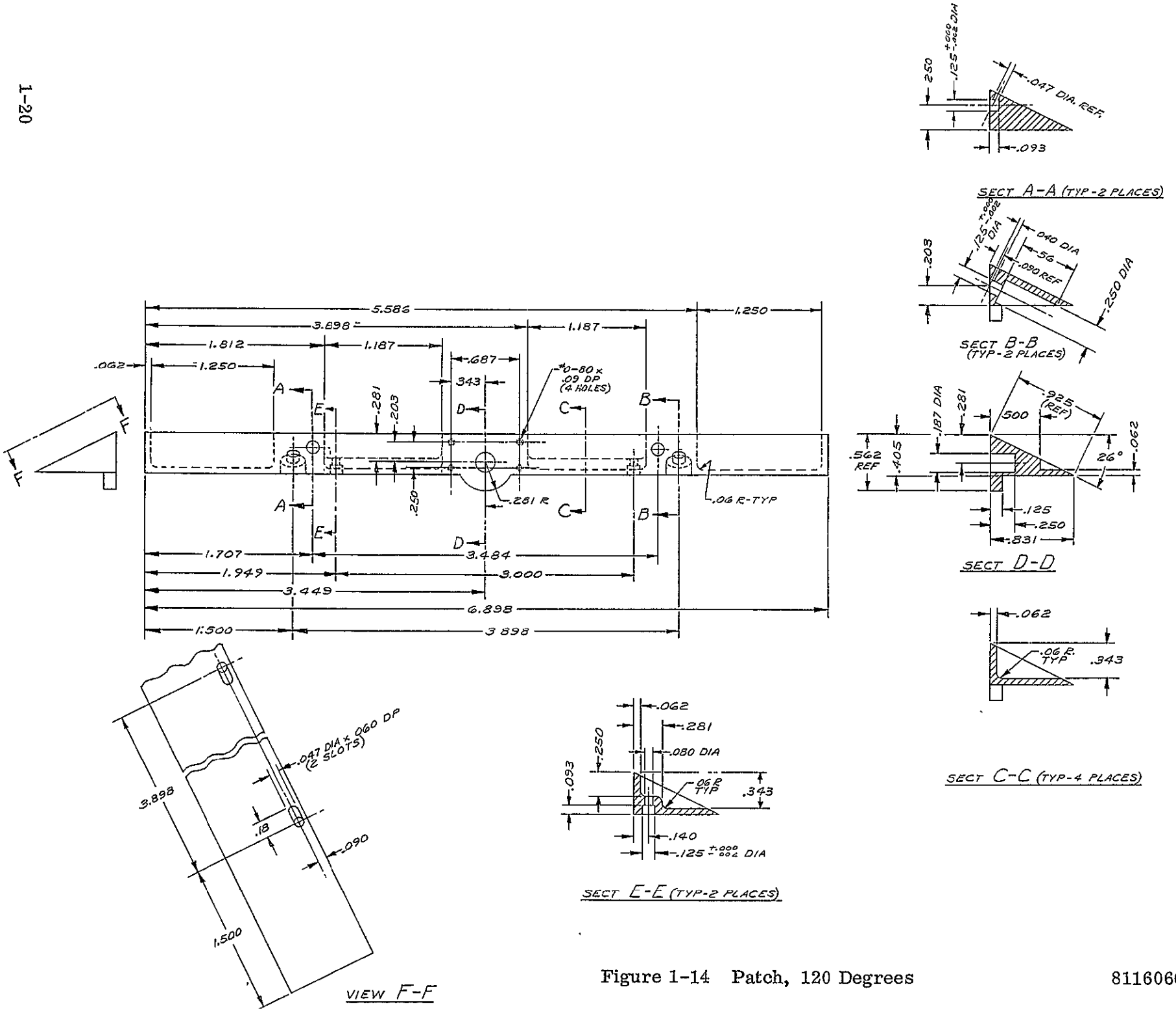

Figure 1-14 Patch, 120 Degrees

8116066

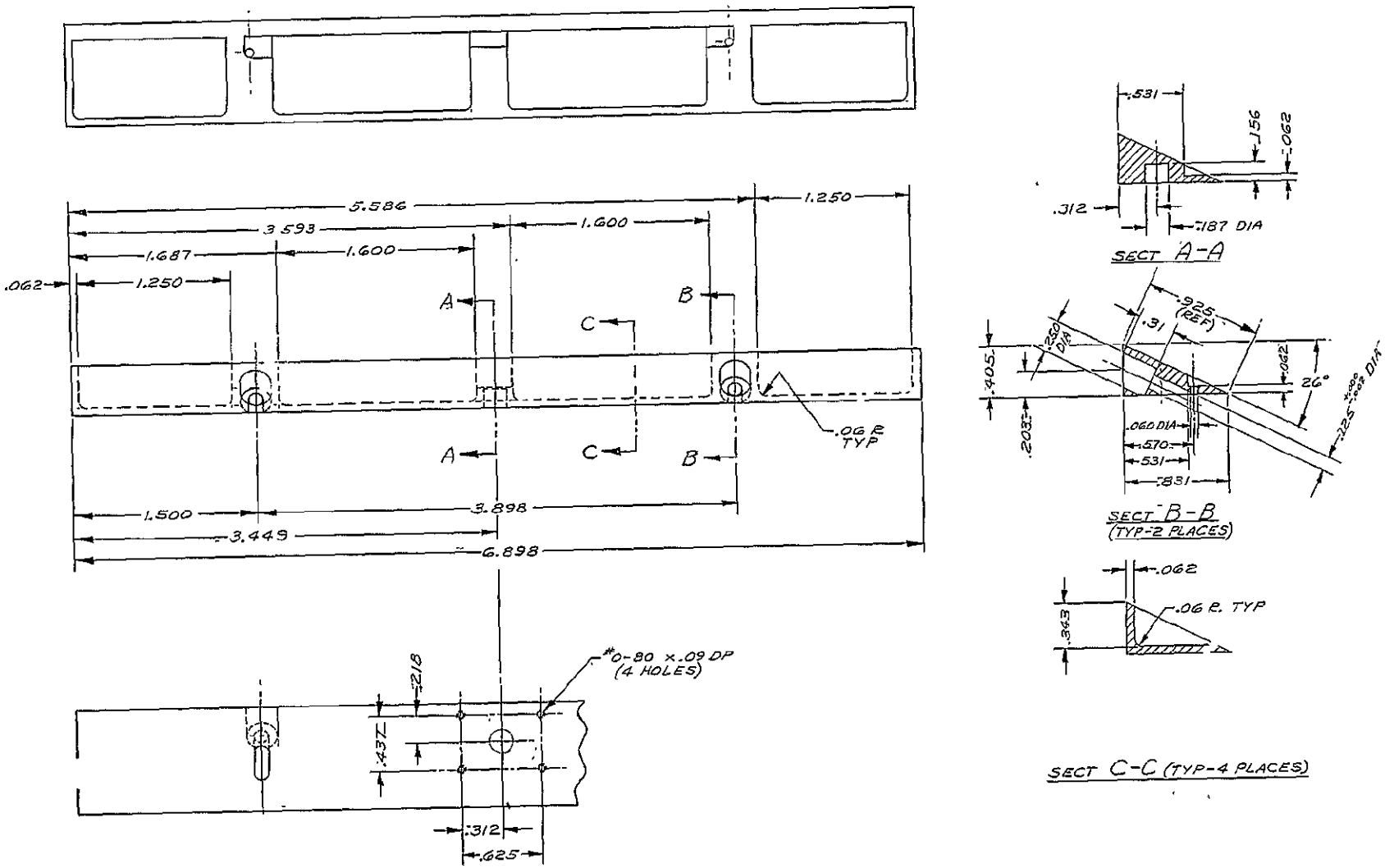

Figure 1-15 Patch, 90 Degrees

8116067

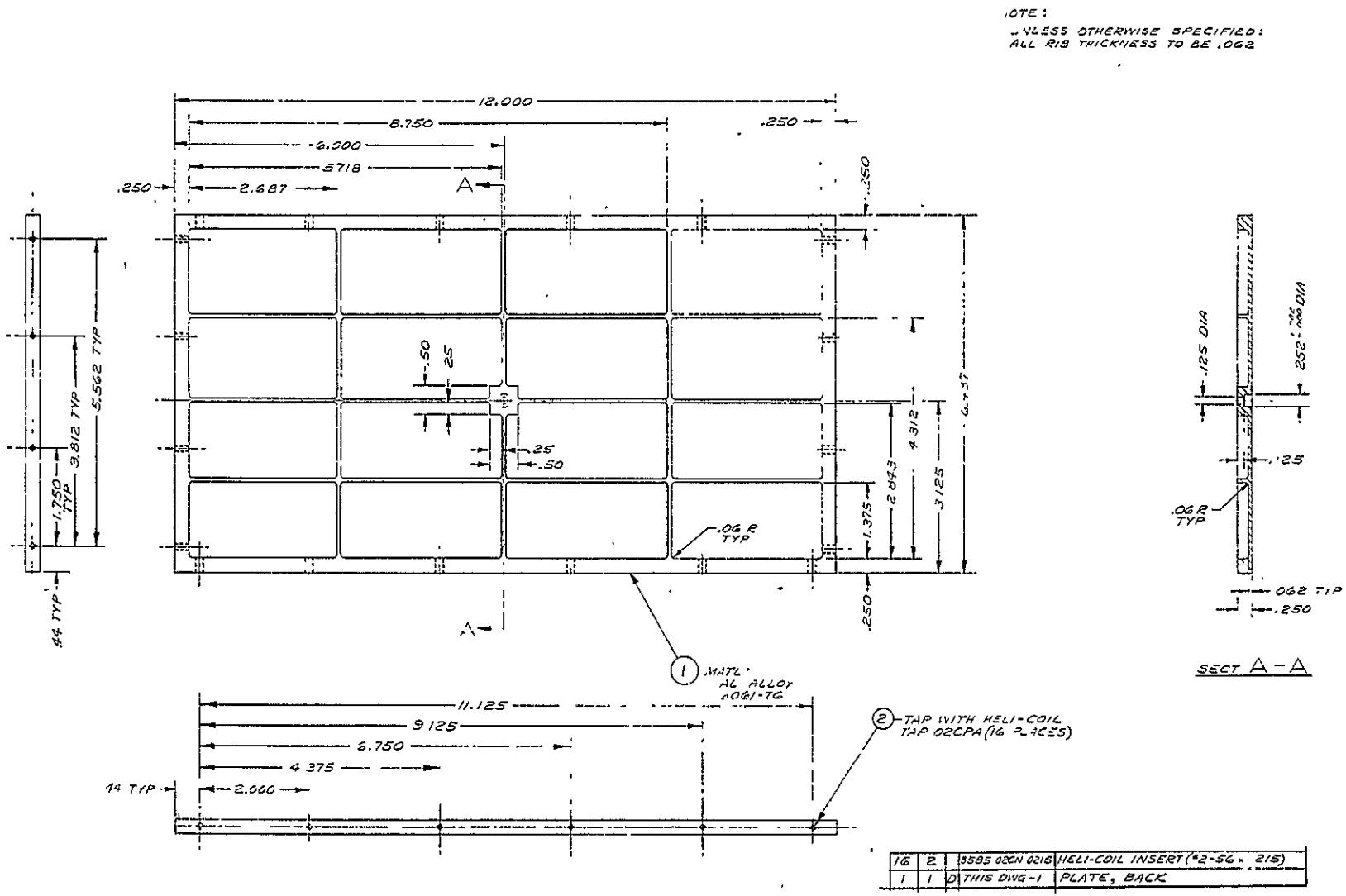

Figure 1-16 Plate, Housing Rack 8116237

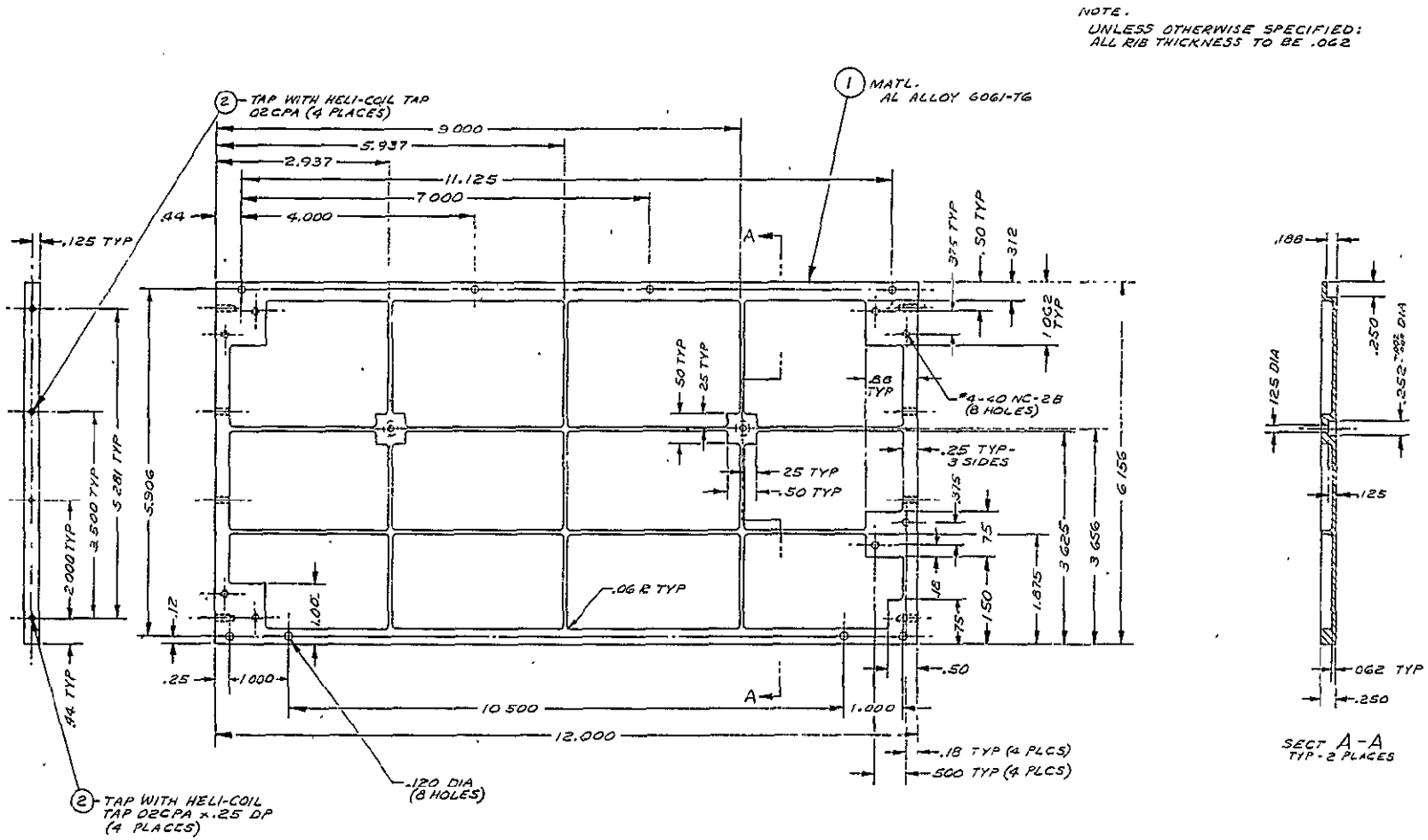

8	2		3585-02CN-0215	HELI-COIL INSERT (#2-56 x .215)
1	1	D	THIS DWG-1	PLATE, BOTTOM

Figure 1-17 Plate, Housing Bottom 8116238

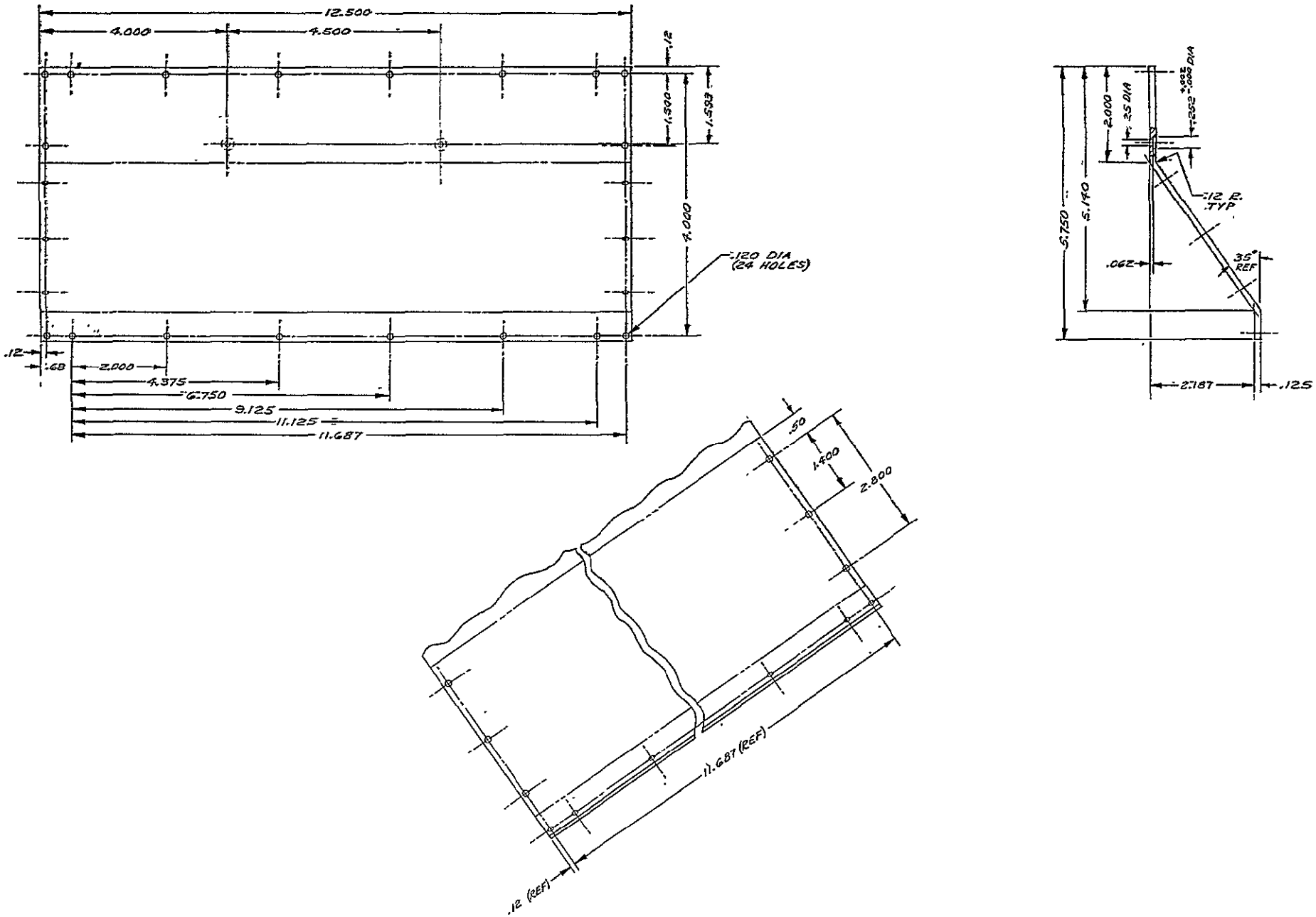

Figure 1-18 Plate, Housing Top 8116241

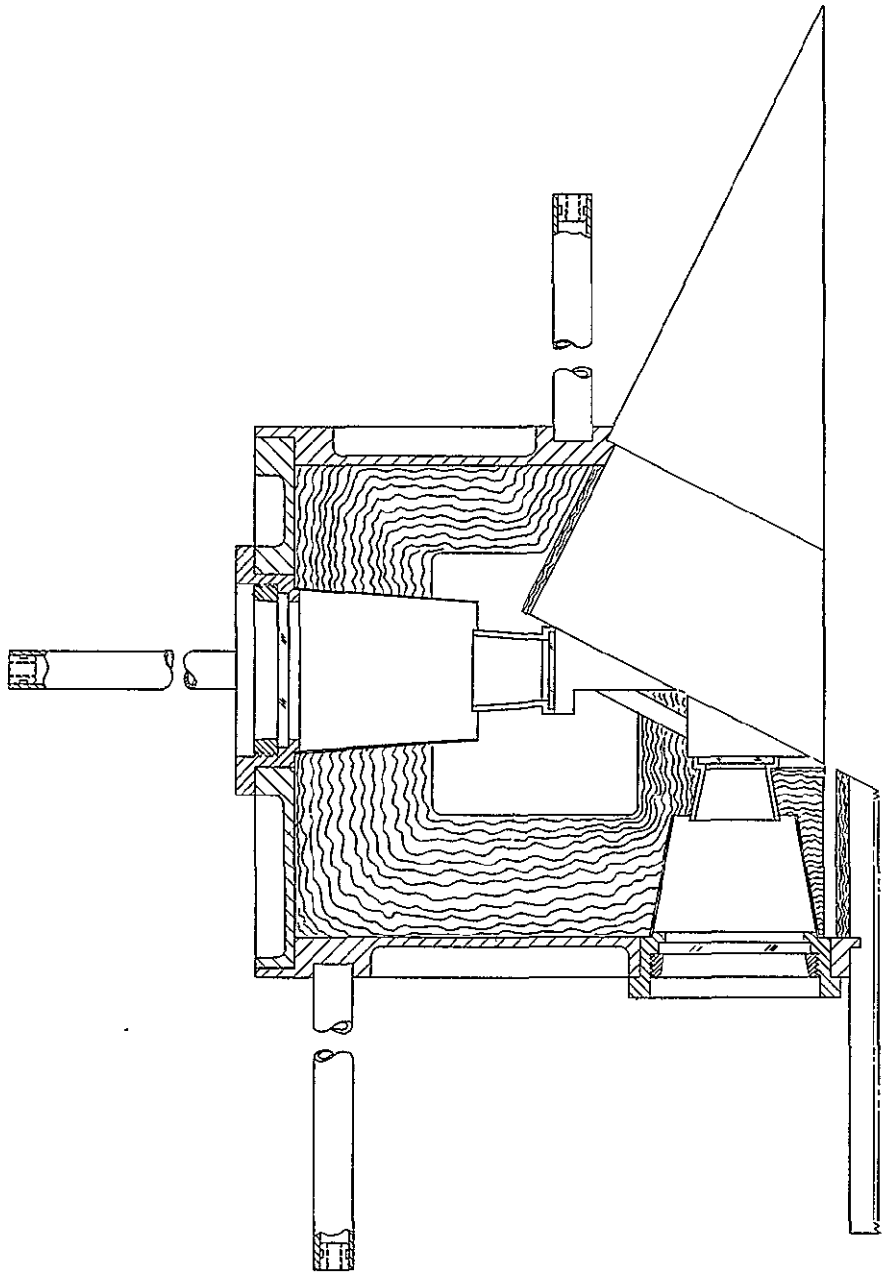

Figure 1-19 Housing Assembly Cone 8116242

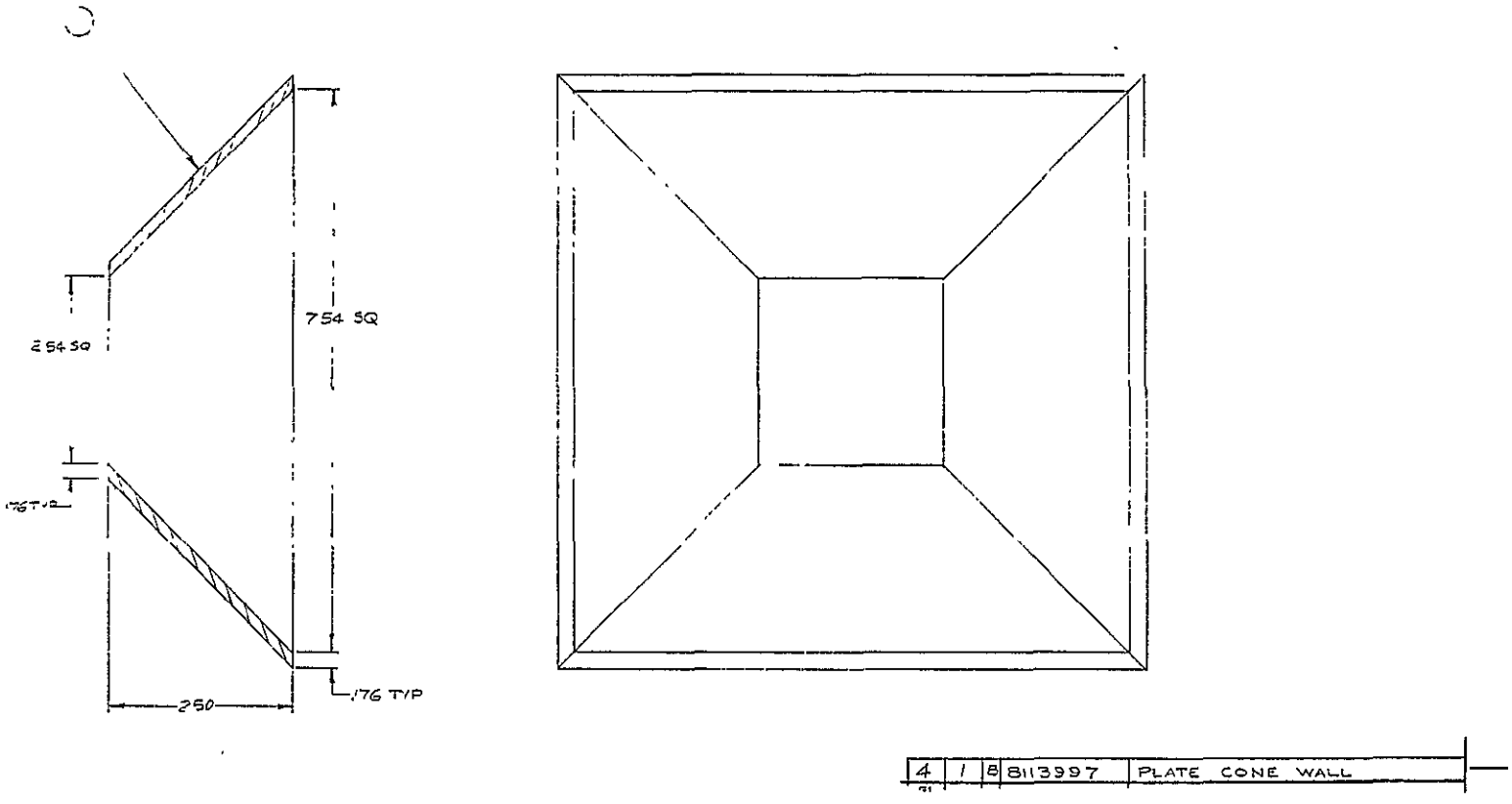

Figure 1-20 Cone, 45 degrees LA Cooler 8113990

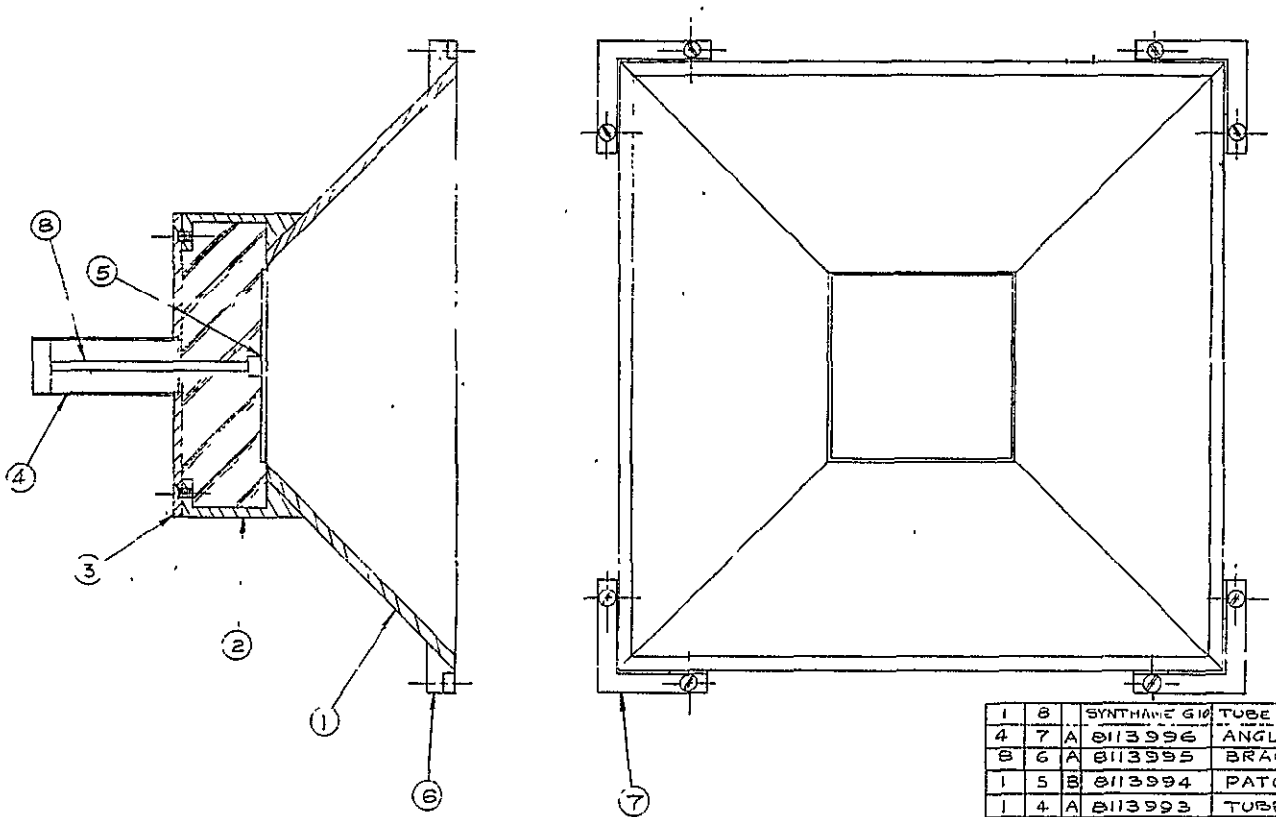

1	8		SYNTHANE G10	TUBE 1/8 OD × 3/32 ID × 3 LONG
4	7	A	8113996	ANGLE
8	6	A	8113995	BRACKET, TOP
1	5	B	8113994	PATCH
1	4	A	8113993	TUBE, SUPPORT
1	3	B	8113992	PLATE, SUPPORT
4	2	A	8113991	BRACKET, BOTTOM
1	1	C	8113990	CONE ASS'Y

Figure 1-21 Cooler Assembly, 45 degree Angle 8113998

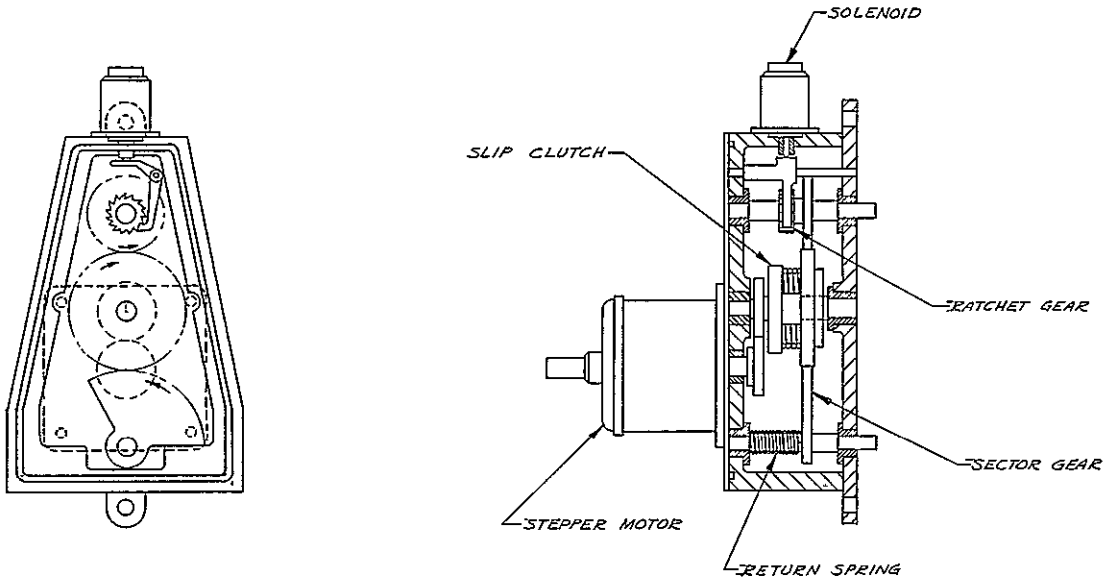

Figure 1-22 Actuator Assembly 8114000

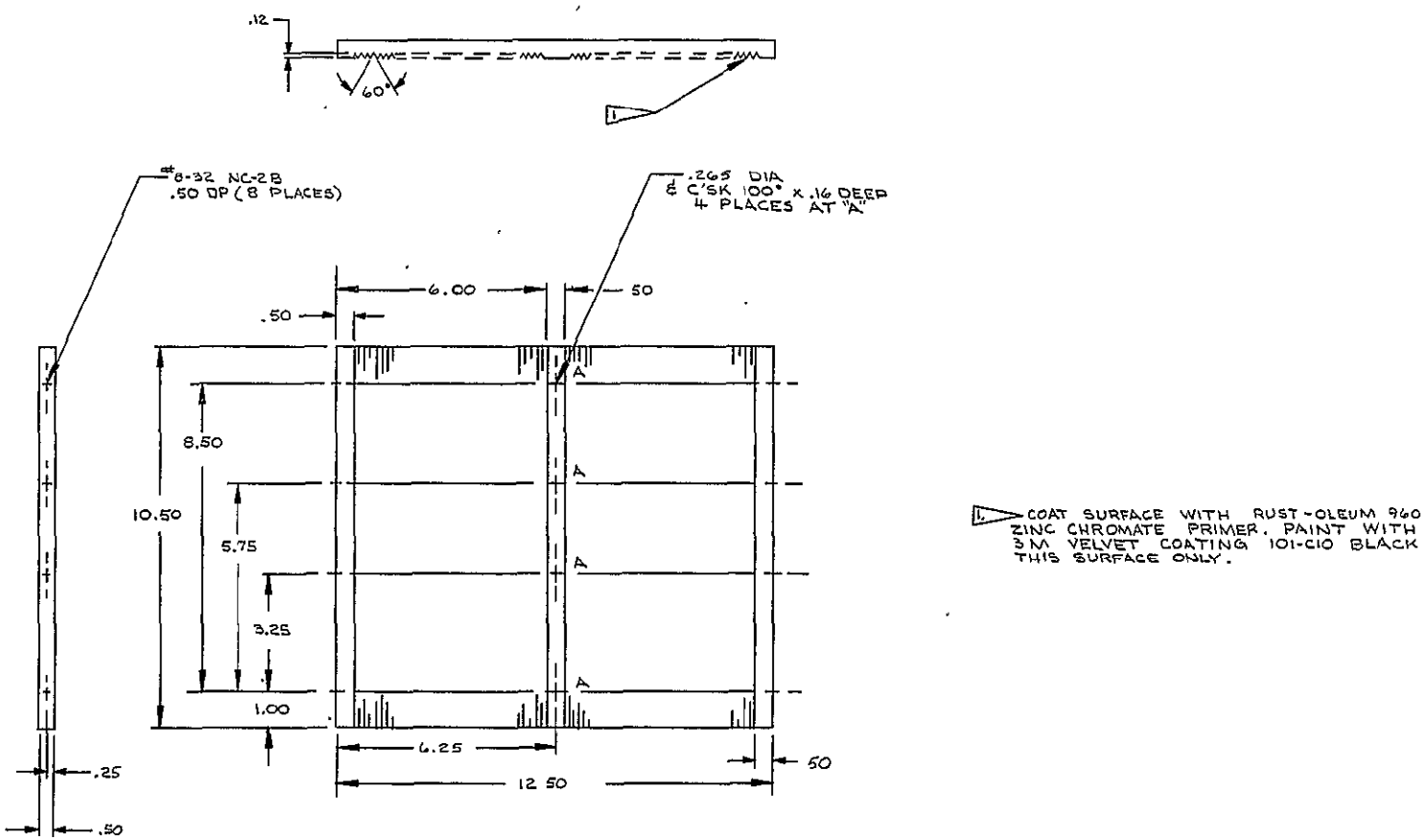

Figure 1-23 Plate, Face - Cold Space Target 8114044

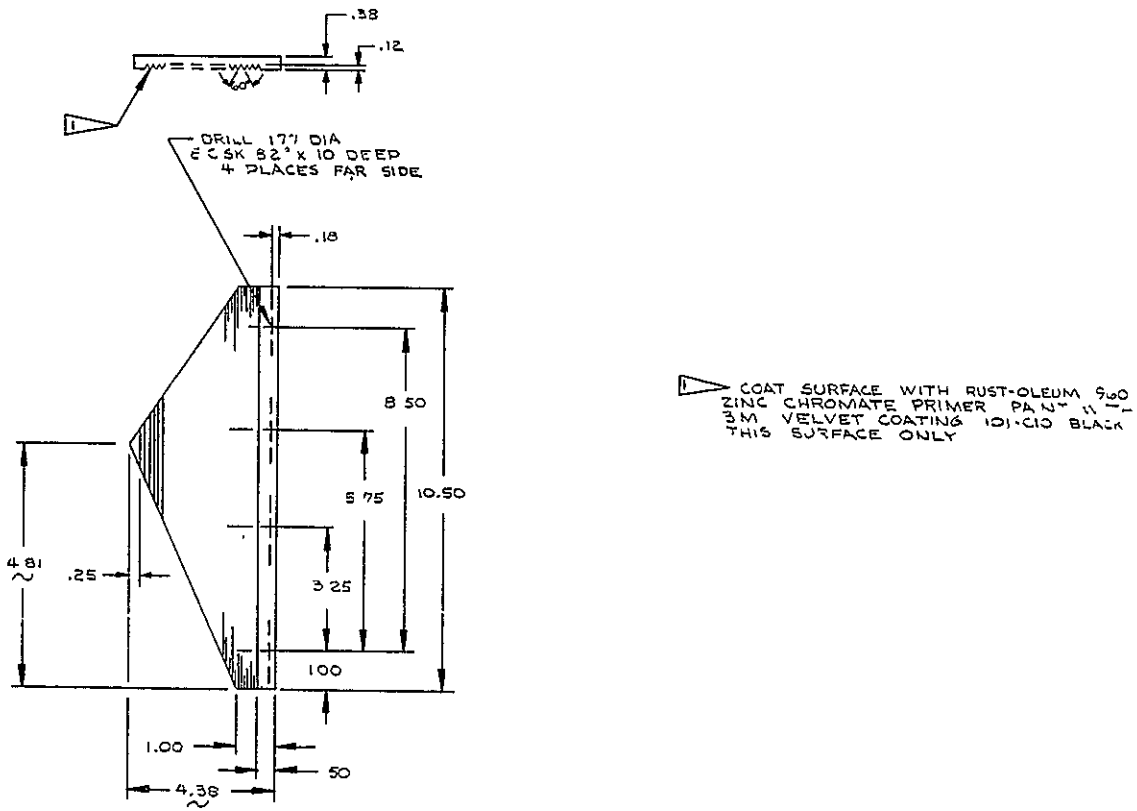

Figure 1-24 Plate, Side-Cold Space Target 8114045

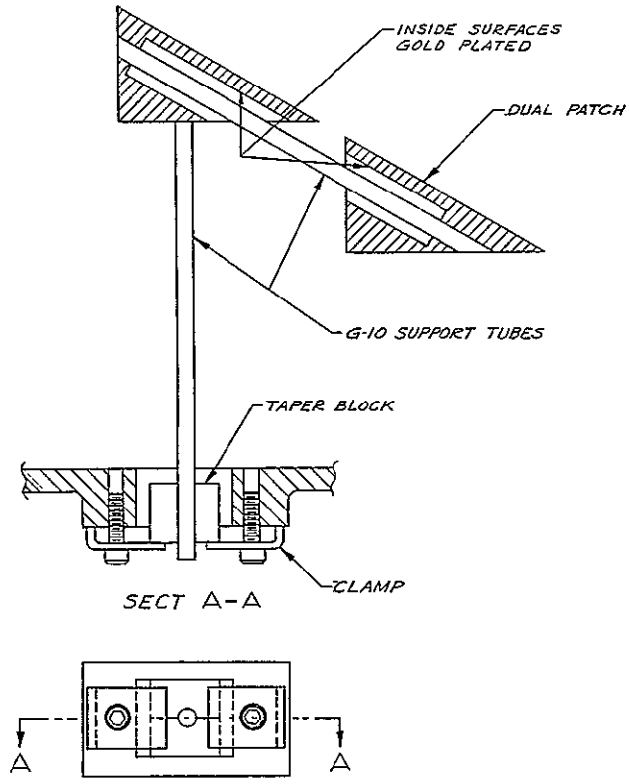

Figure 1-25 Suspension - Dual Patch 8114057

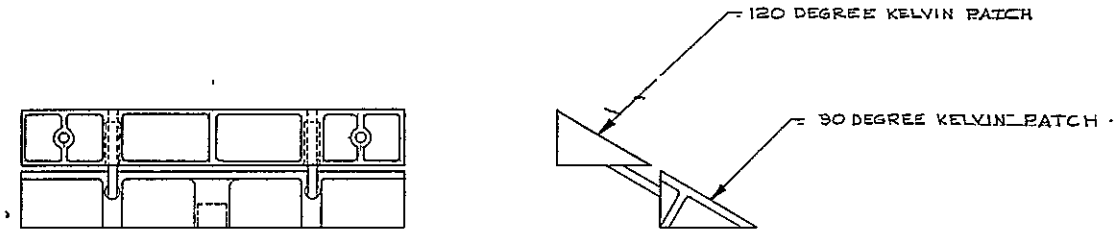

Figure 1-26 Patch Assembly 8114058

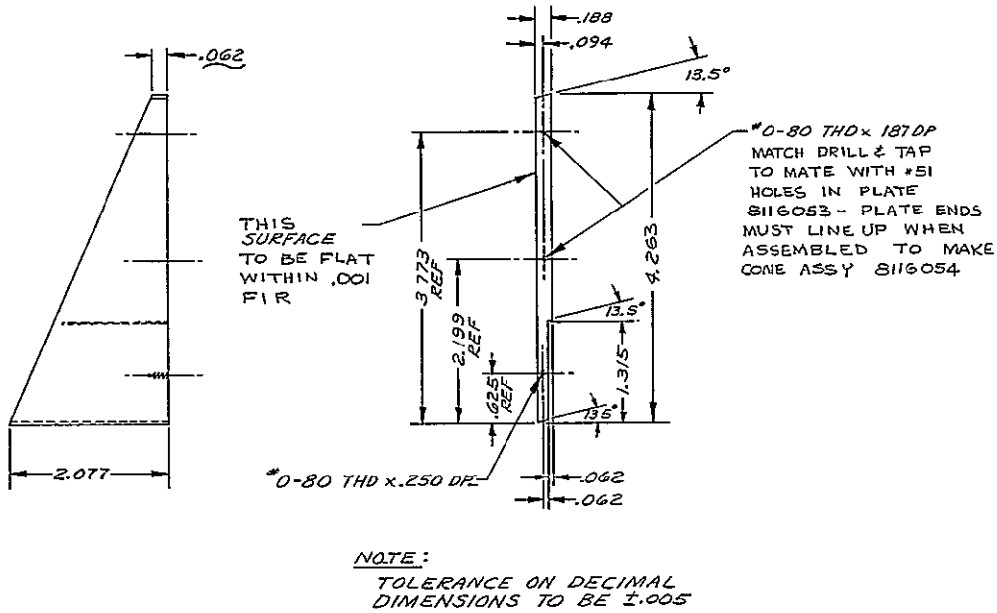

Figure 1-27 Plate, Side - MERC Cone 8116052

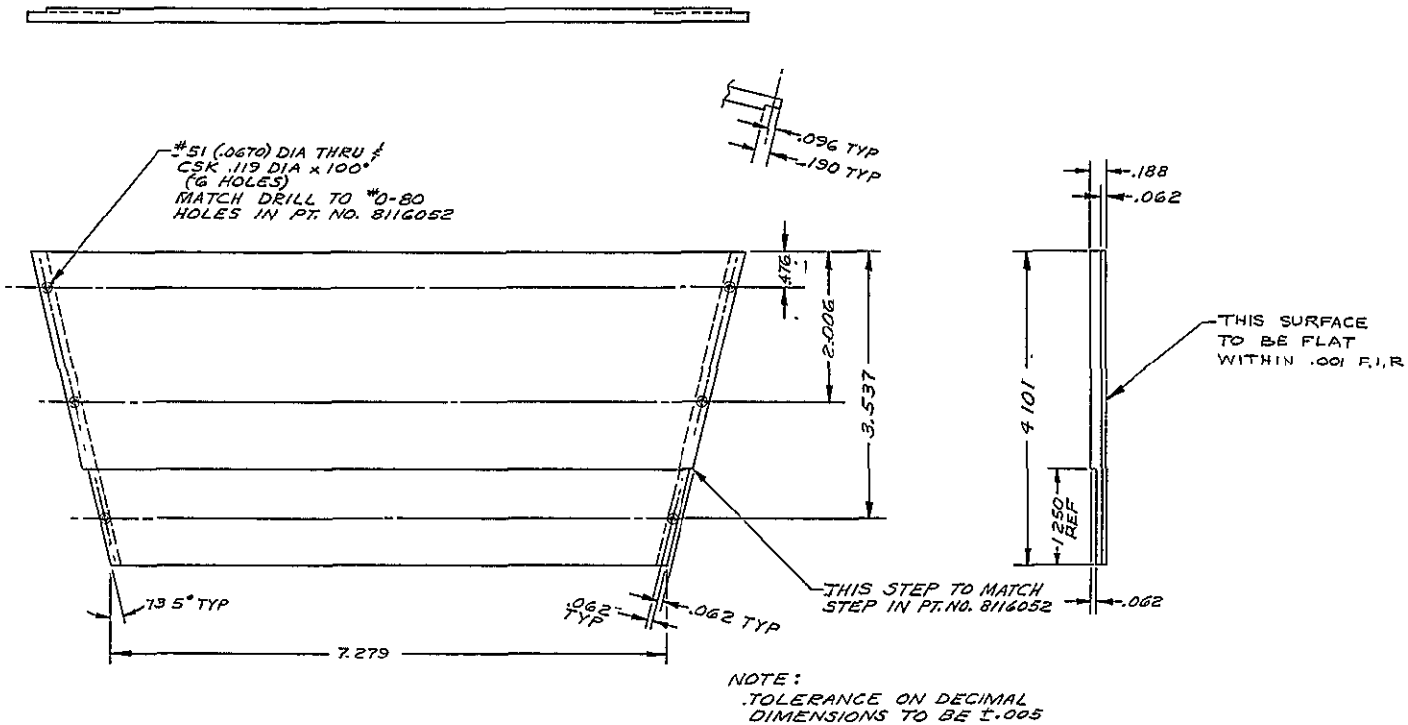

Figure 1-28 Plate, Back - MERC Cone 8116053

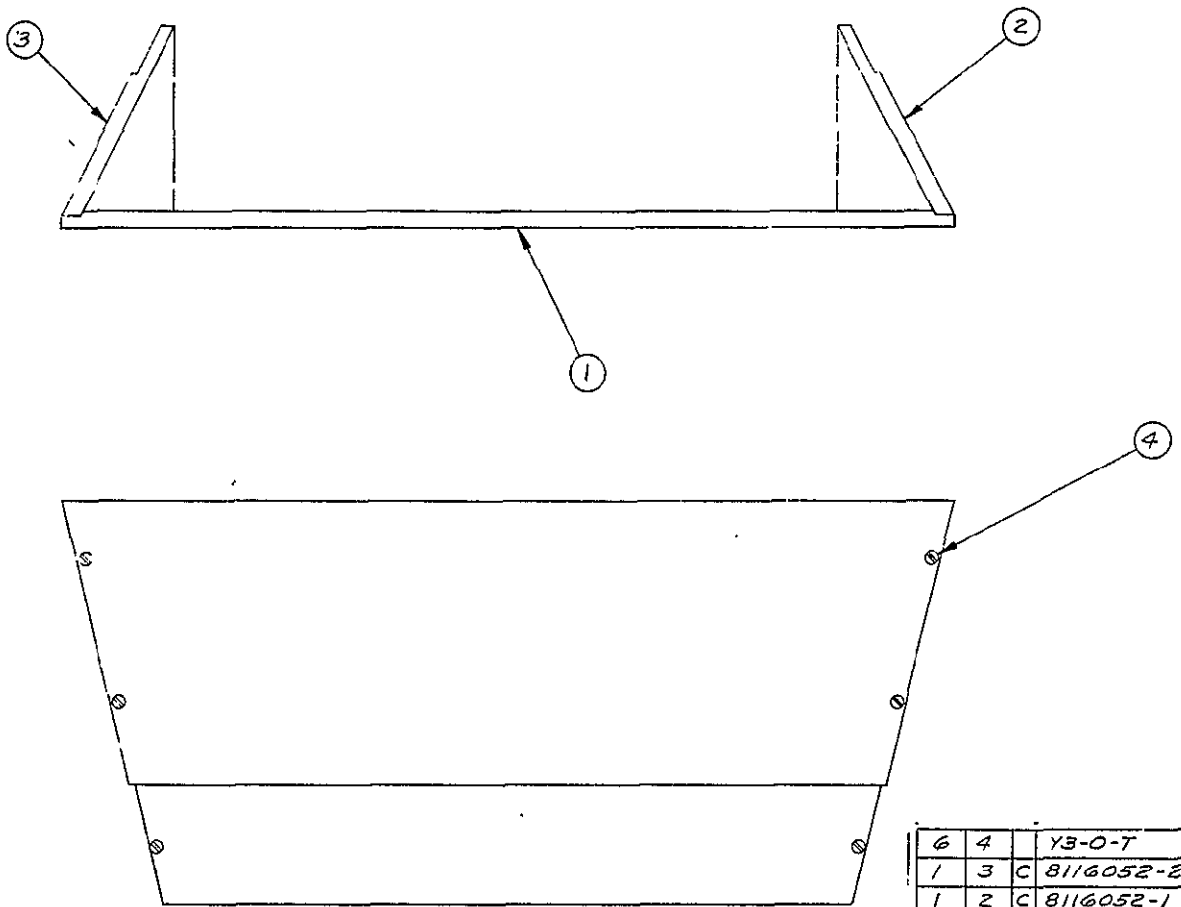

6	4		Y3-0-T	SCREW, FL HD (#0-80 x 1/4) PIC
1	3	C	8116052-2	PLATE, CONE SIDE
1	2	C	8116052-1	PLATE, CONE SIDE
1	1	C	8116053	PLATE, CONE BACK

Figure 1-29 Cone Assembly MERC - 8116054

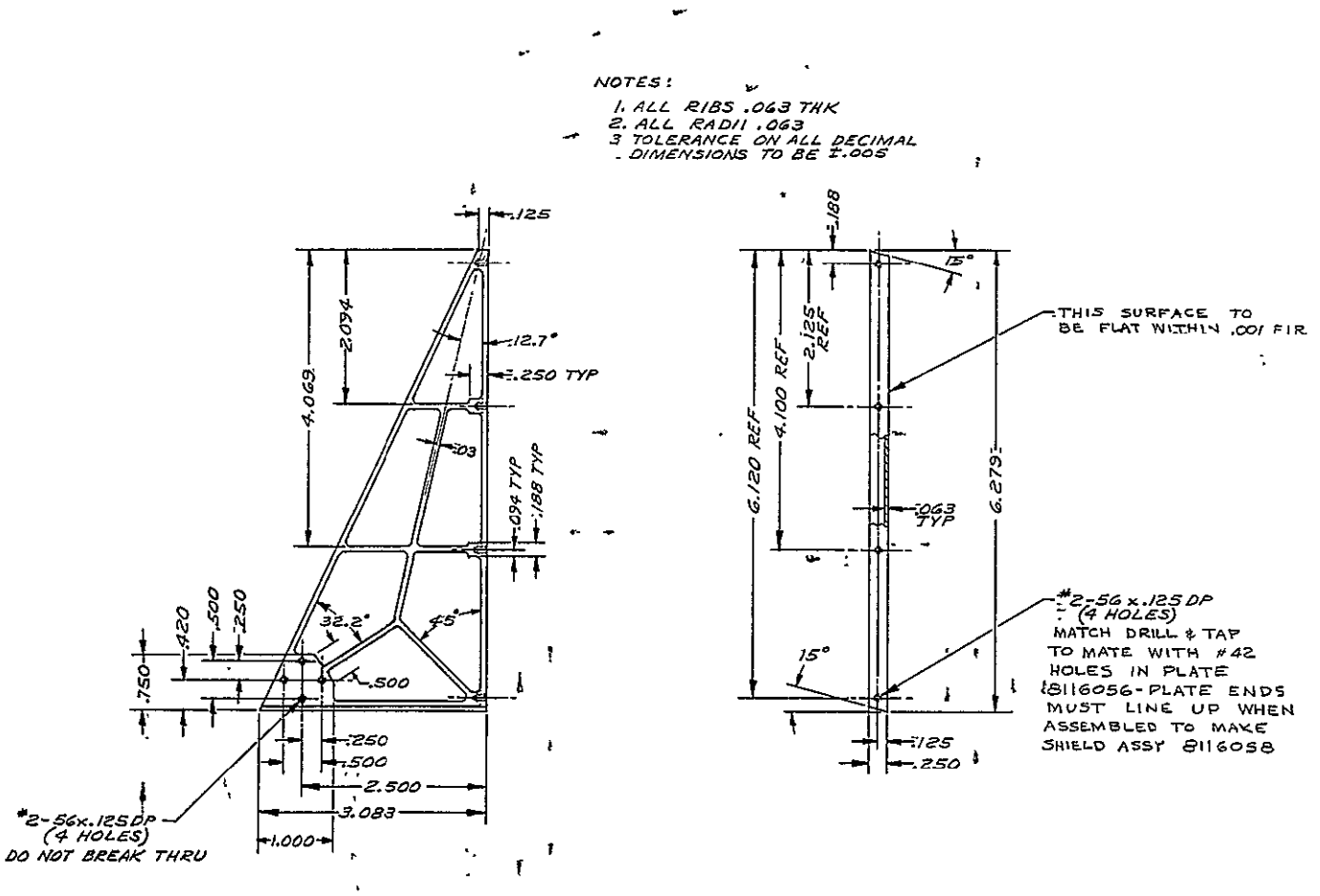

Figure 1-30 Plate, Side - Shield 8116055

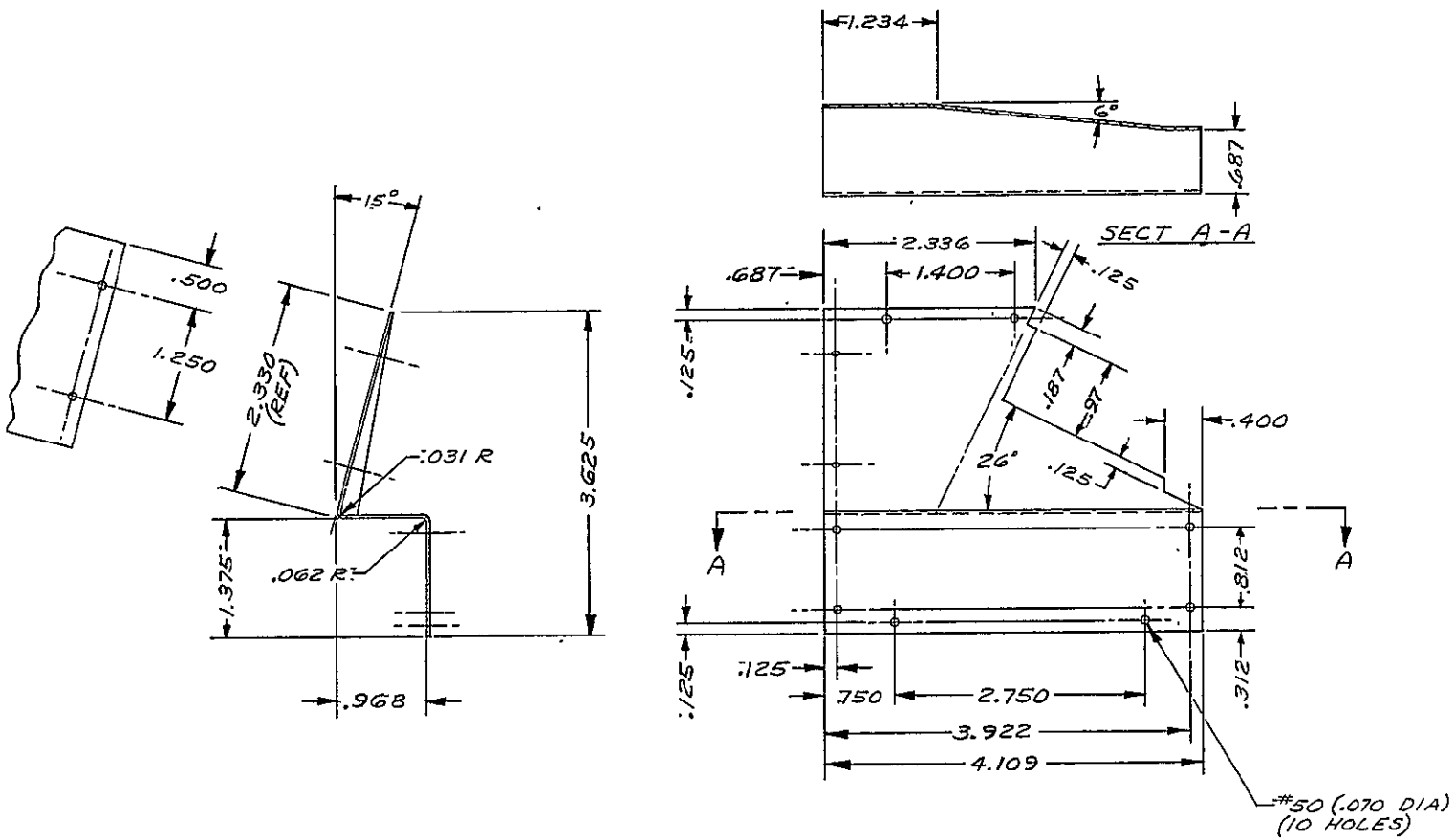

Figure 1-31 Cover, Side - Cone Housing, Left 8116063

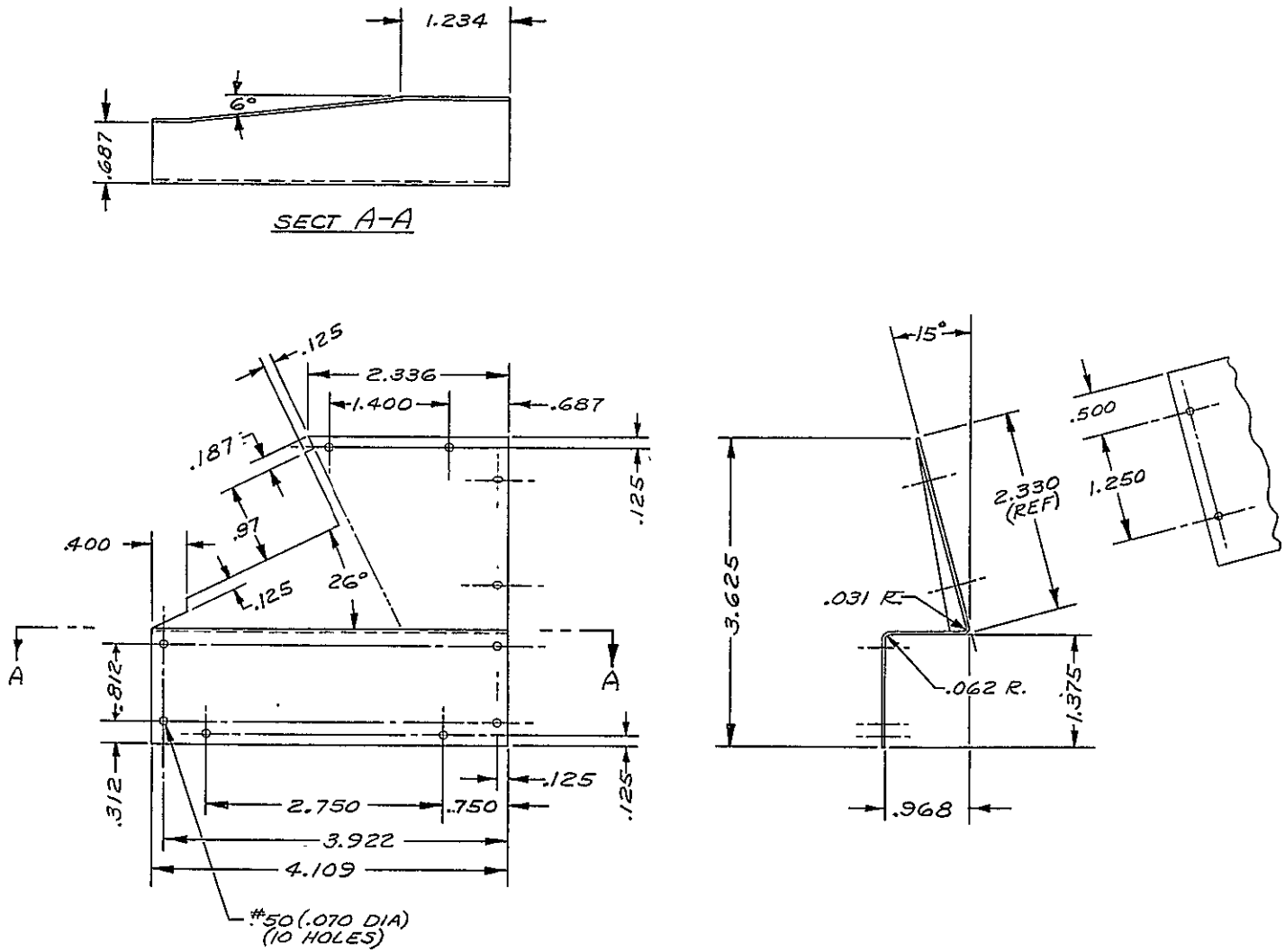

Figure 1-32 Cover, Side - Cone Housing, Right 8116064

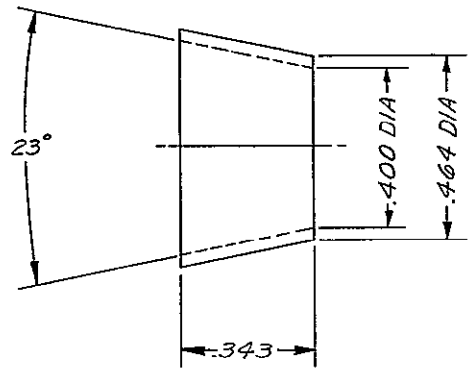

Figure 1-33 Cone, Anti-Icing, 90 Degrees K 8116070

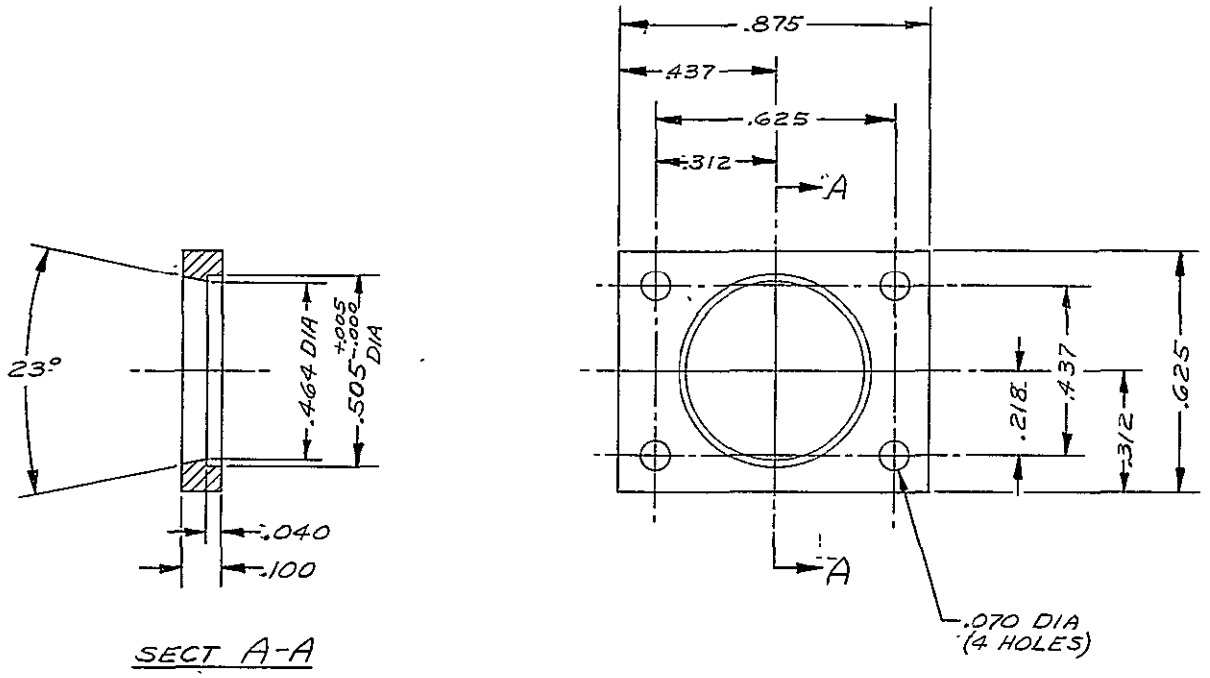

Figure 1-34 Mount, 90 Degree Anti-Icing Cone 8116071

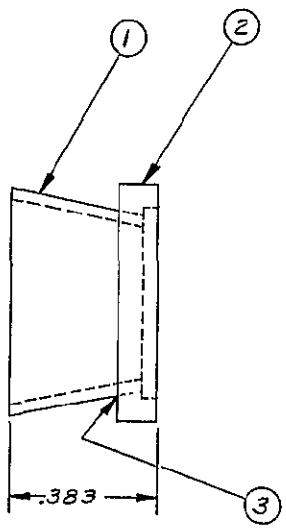

AR	3		2216	EPOXY, CLEAR AMBER (3M)
1	2	C	8116071	MOUNT, CONE
1	1	C	8116070	CONE

Figure 1-35 Cone Assembly - Anti-Icing 90 Degrees K 8116230

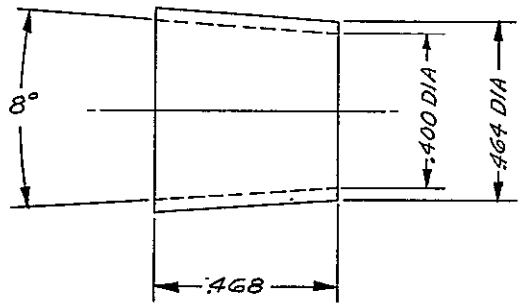

Figure 1-36 Cone - Anti-Icing 120 Degrees K 8116231

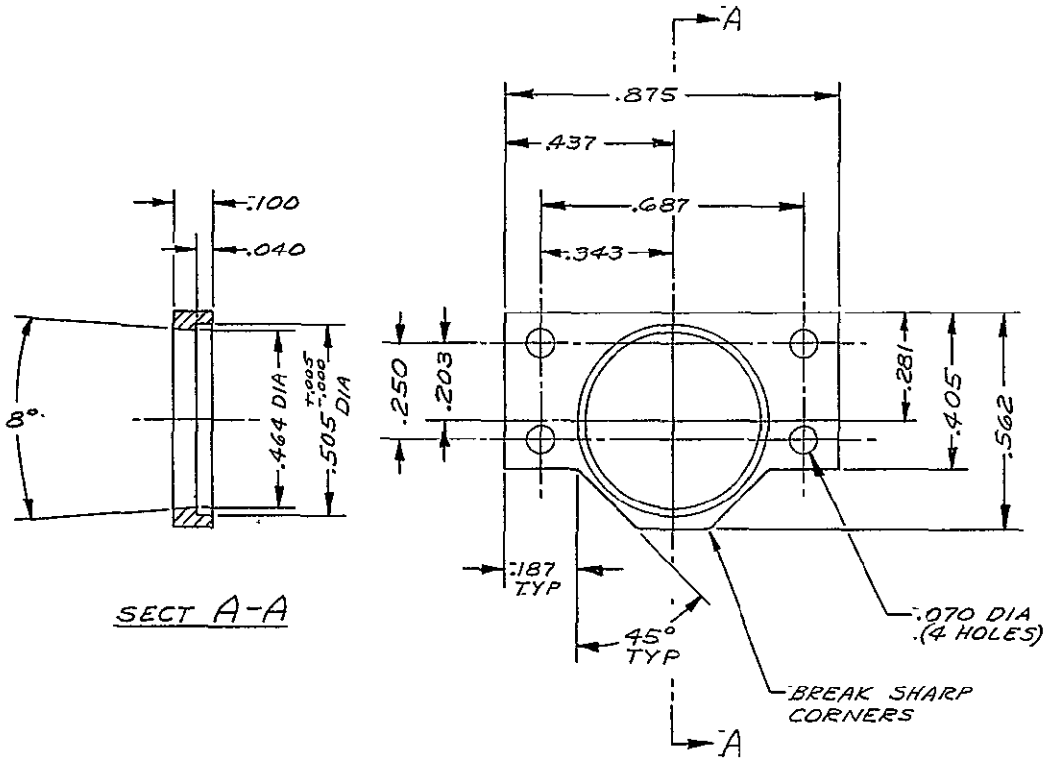

Figure 1-37 Mount, 120 Degrees Anti-Icing Cone 8116232

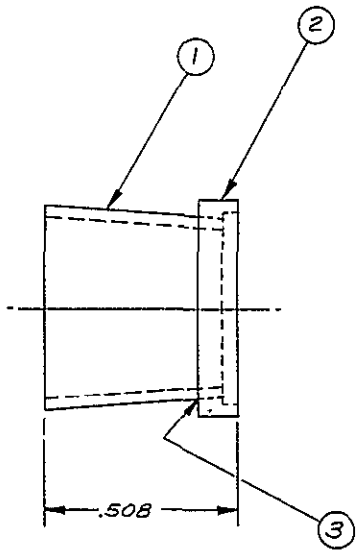

AR	3		221G	EPOXY, CLEAR AMBER (3M)
1	2	C	8116232	MOUNT, CONE
1	1	C	8116231	CONE

Figure 1-38 Cone Assembly, Anti-Icing, 120 Degrees K 8116233

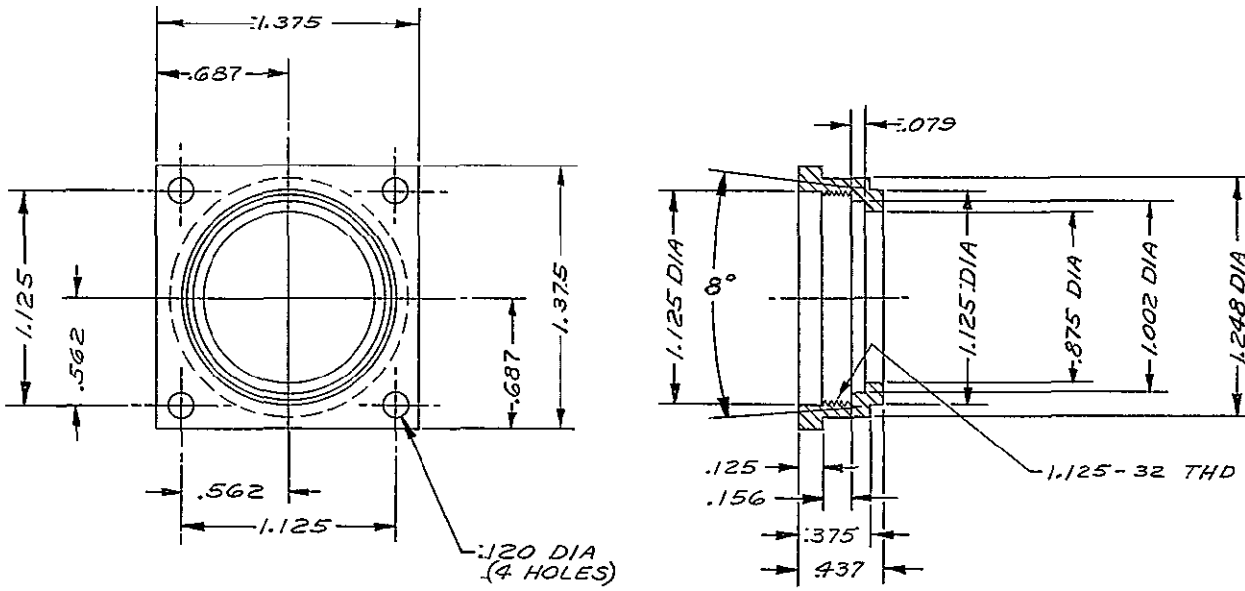

Figure 1-39 Retainer, Irtran 2 Window 8116235

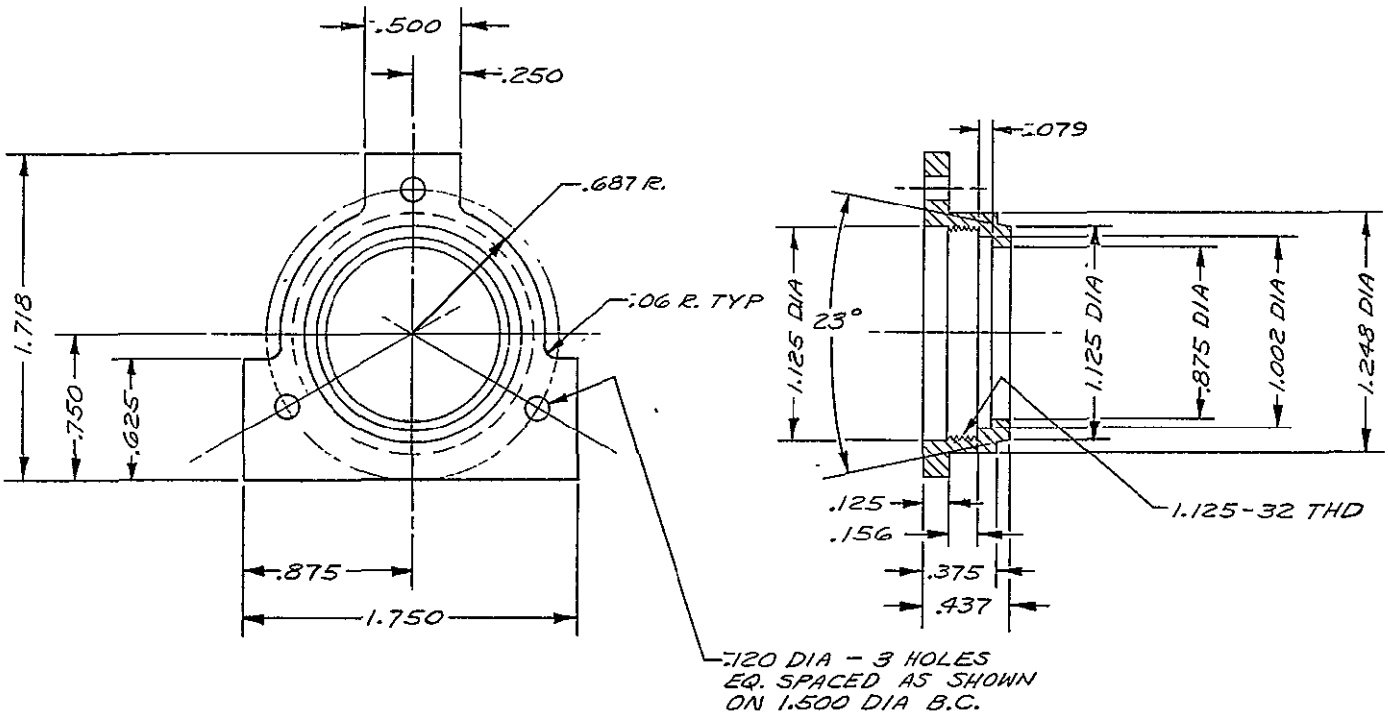

Figure 1-40 Retainer, Iratran 2 Window 8116236

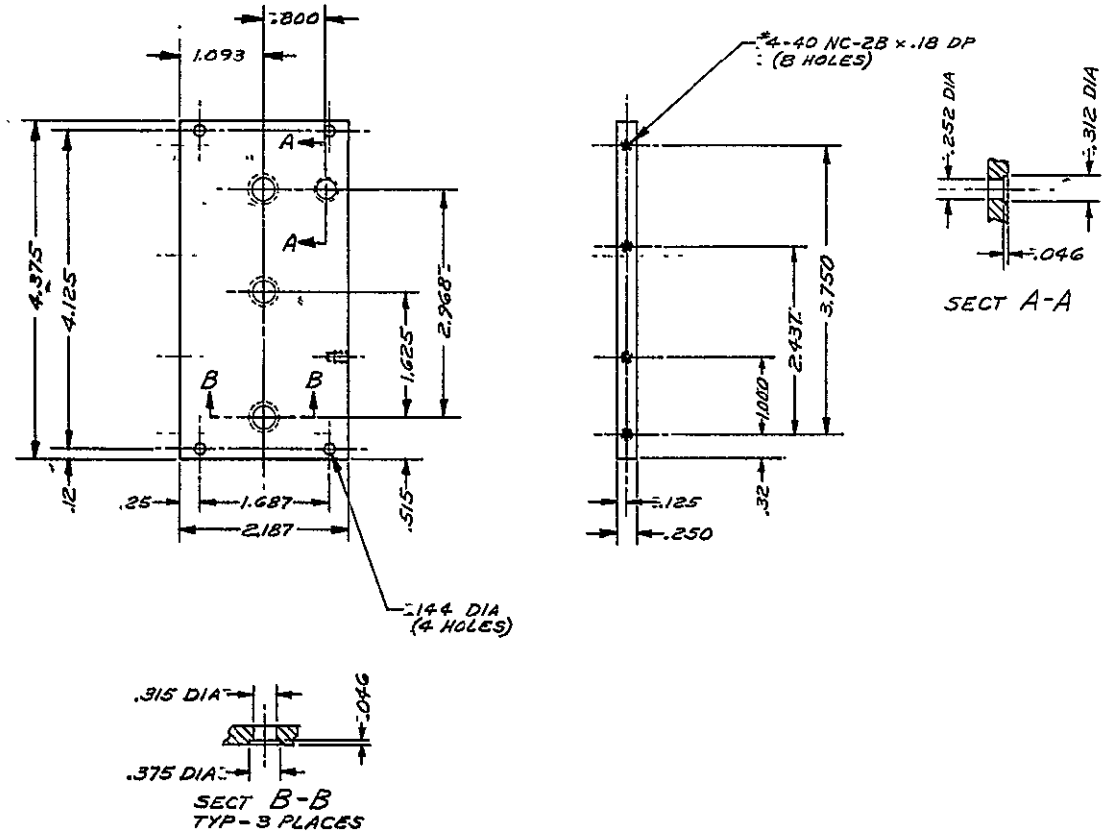

Figure 1-41 Plate Side-Actuator 8338428

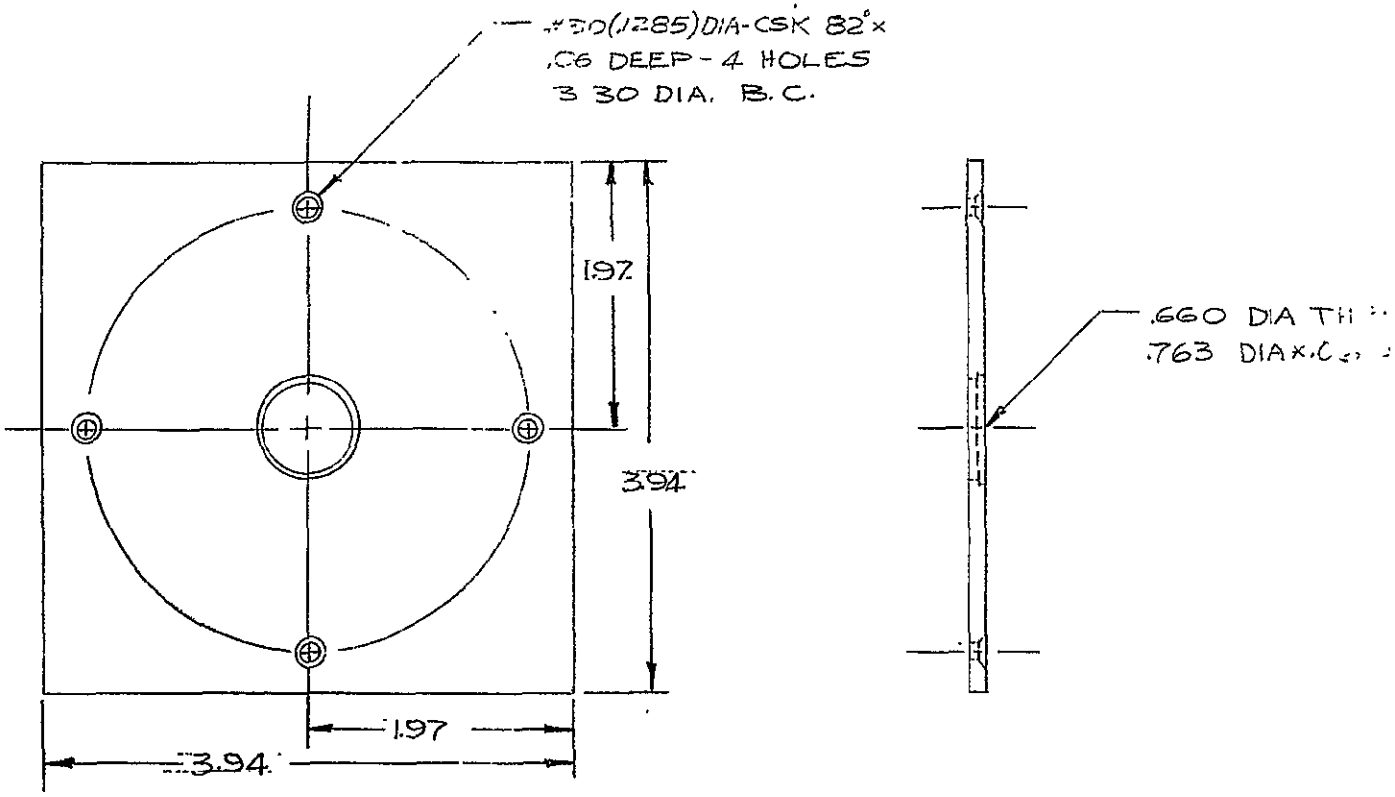

Figure 1-42 Plate, Support - 45 Degree LA Cooler 8113992

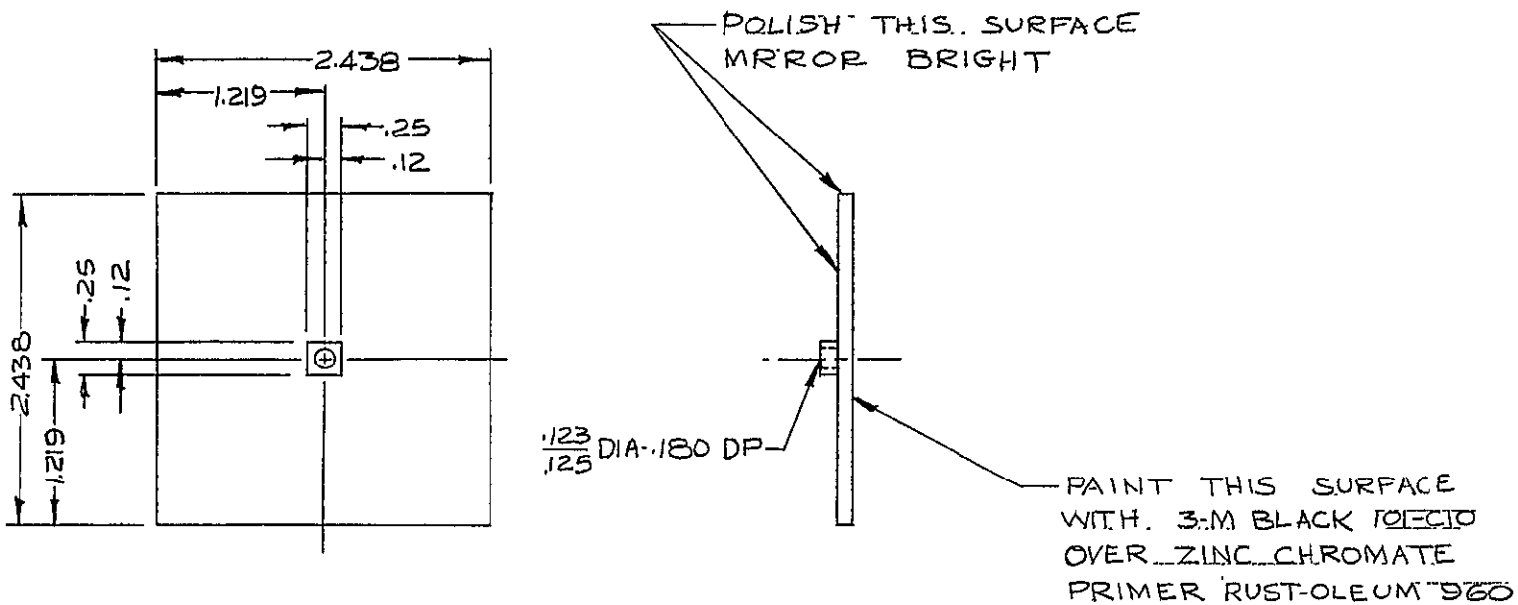

Figure 1-43 Patch - 45 Degree LA Cooler 8113994

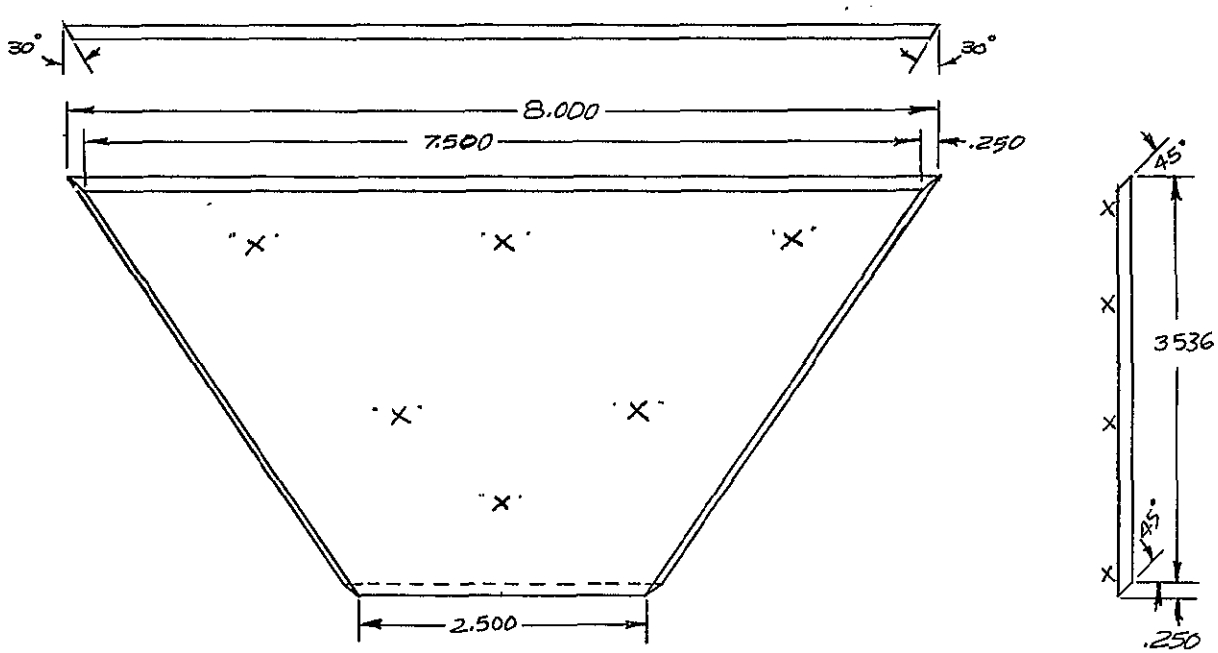

NOTES:
(1.) ELECTROLESS NICKEL PLATE ALL OVER.
(2.) SURFACE MARKED "X" TO BE GROUND & POLISHED TO WITHIN 3 FRINGES OF VISIBLE LIGHT EXCEPT FOR .062" MAX. AROUND EDGE FOR RUN OUT.
(3.) DIMENSIONS ARE FOR AFTER PLATING & POLISHING.

Figure 1-44 Plate, Cone Wall - 45 Degree LA Cooler 8113997

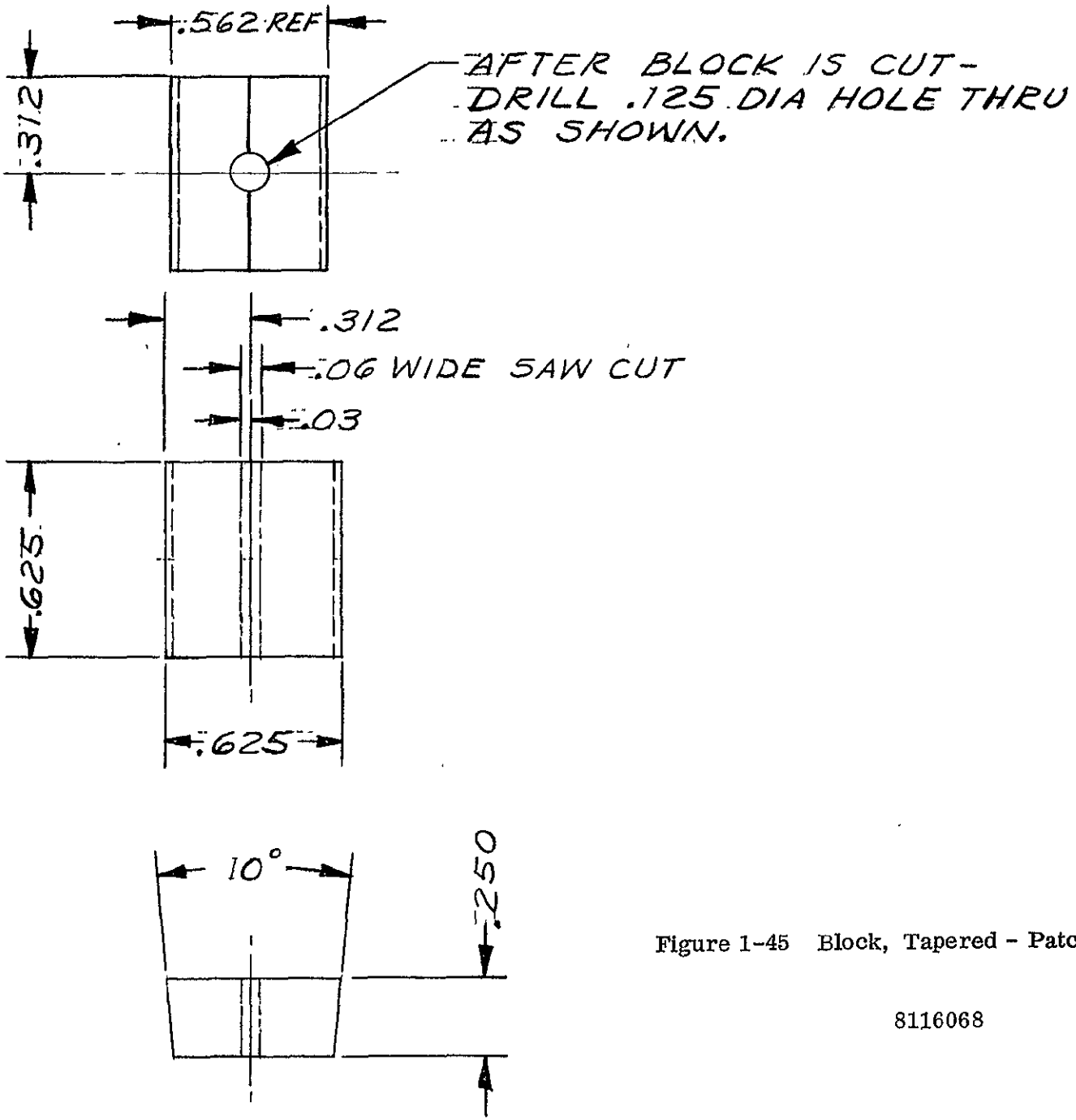

Figure 1-45 Block, Tapered - Patch Support MERC

8116068

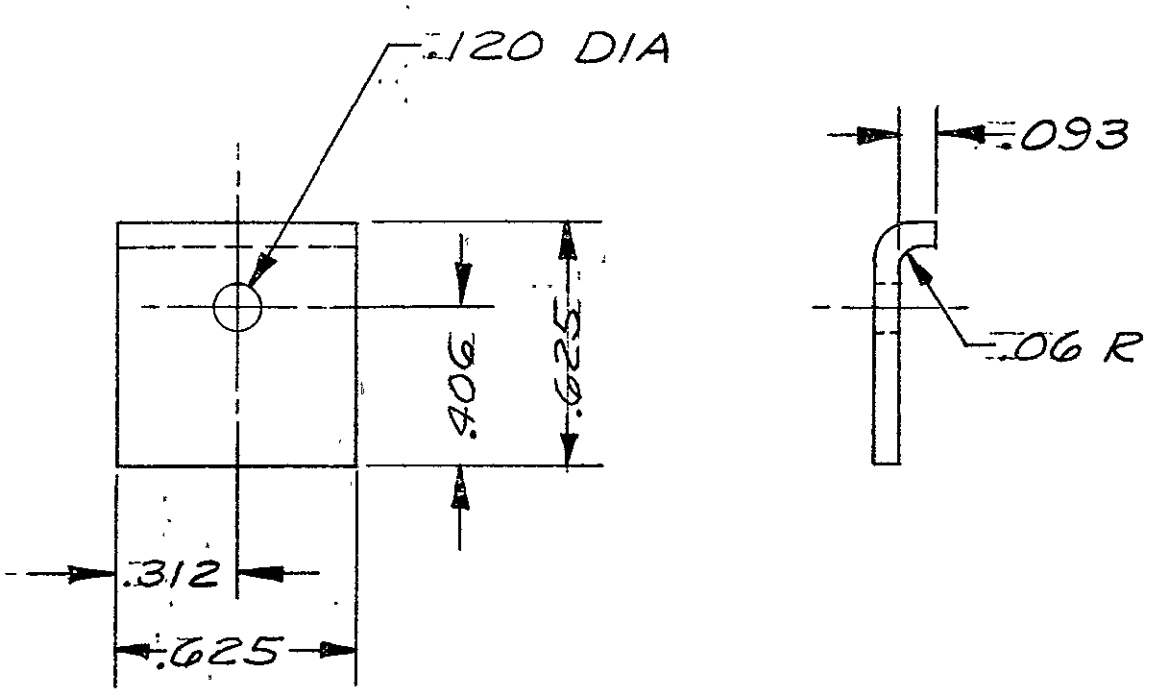

Figure 1-46 Clamp - Patch Support MERC 8116069

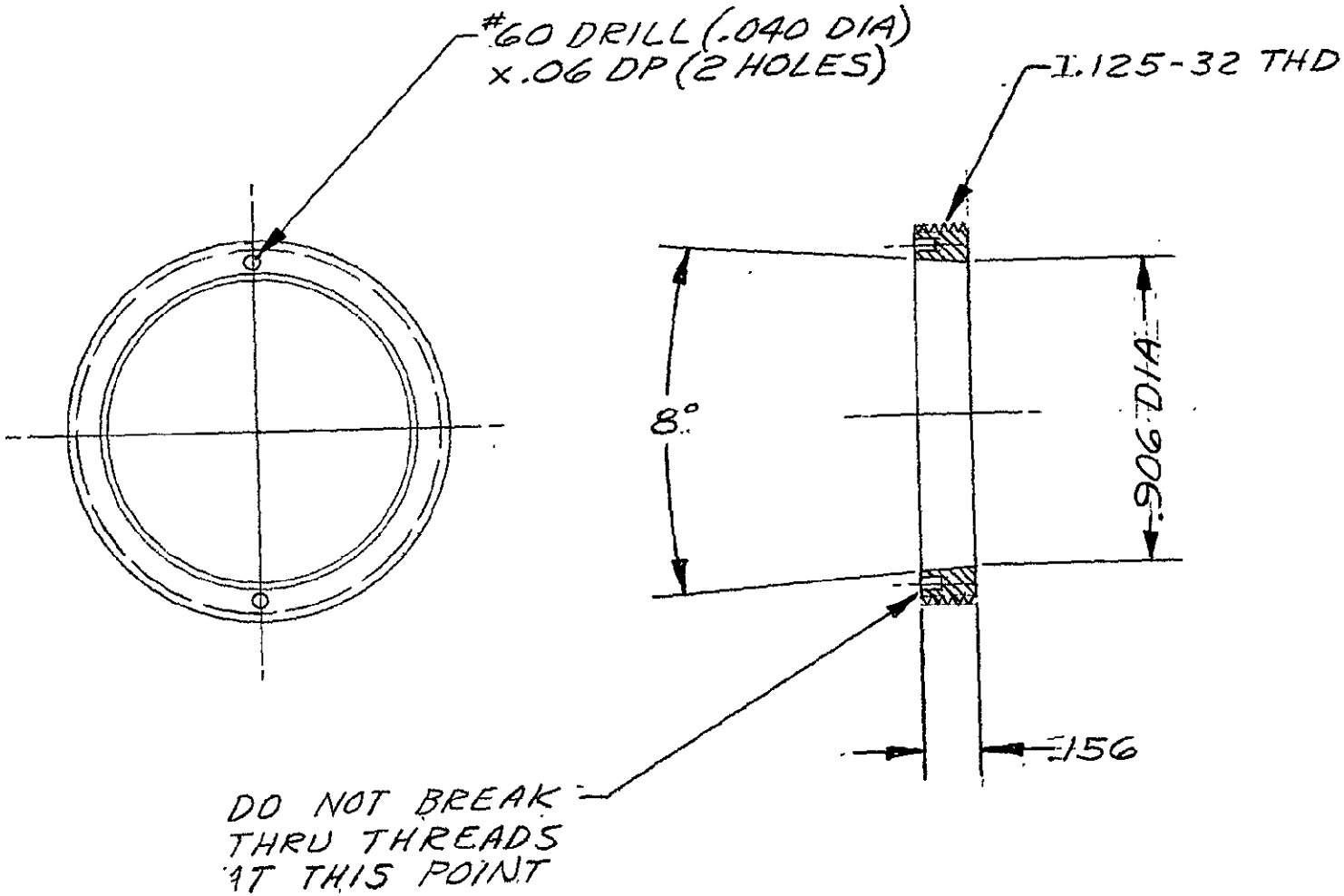

Figure 1-47 Ring, Lens Retainer

8116234

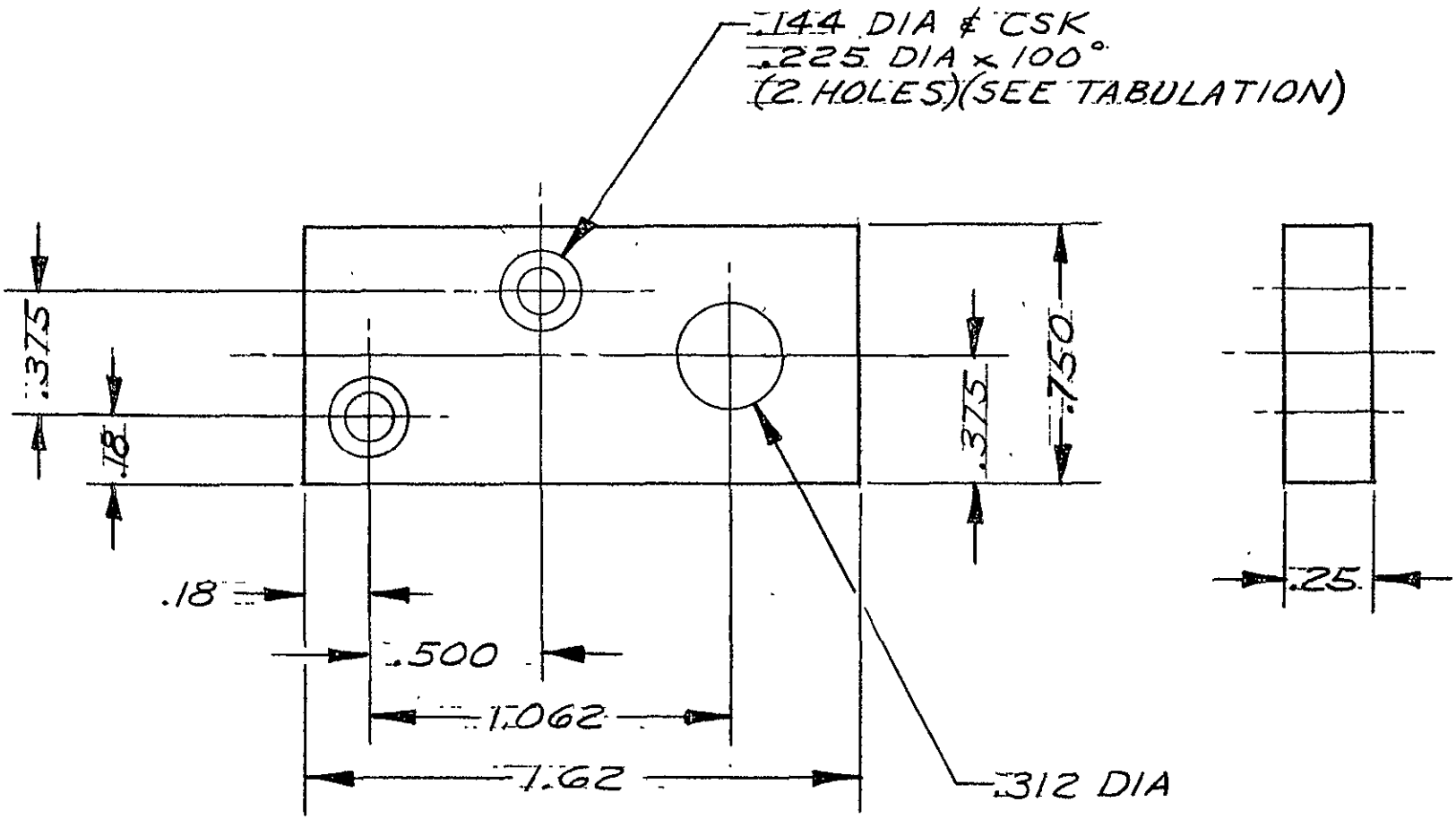

Figure 1-48 Foot Mounting MERC 8116239

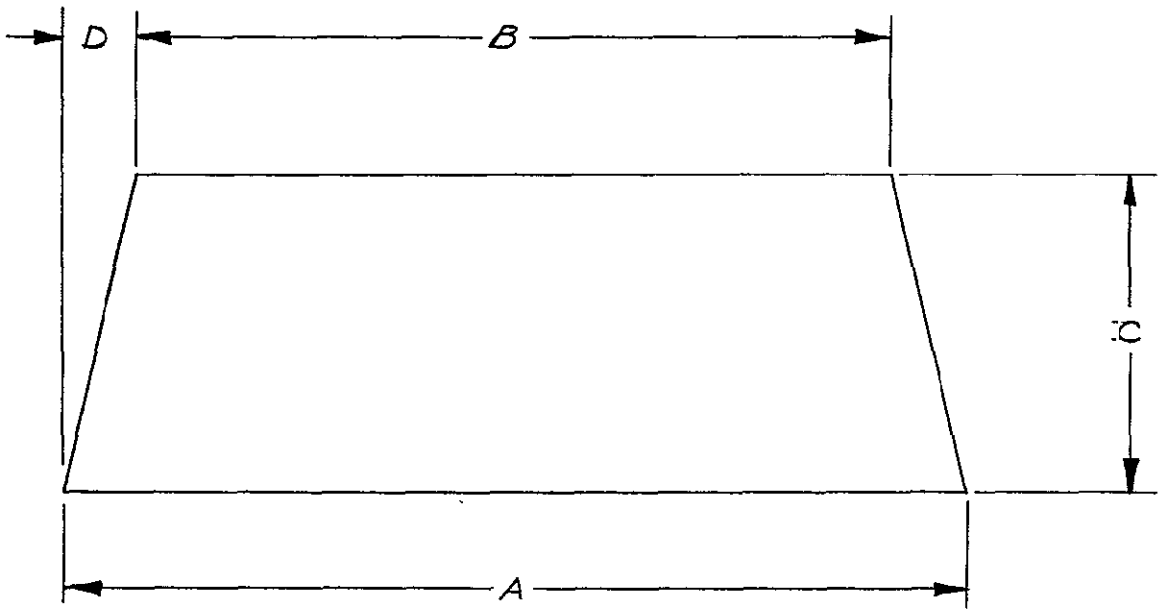

Figure 1-49 Baffle, Insulation 8116243

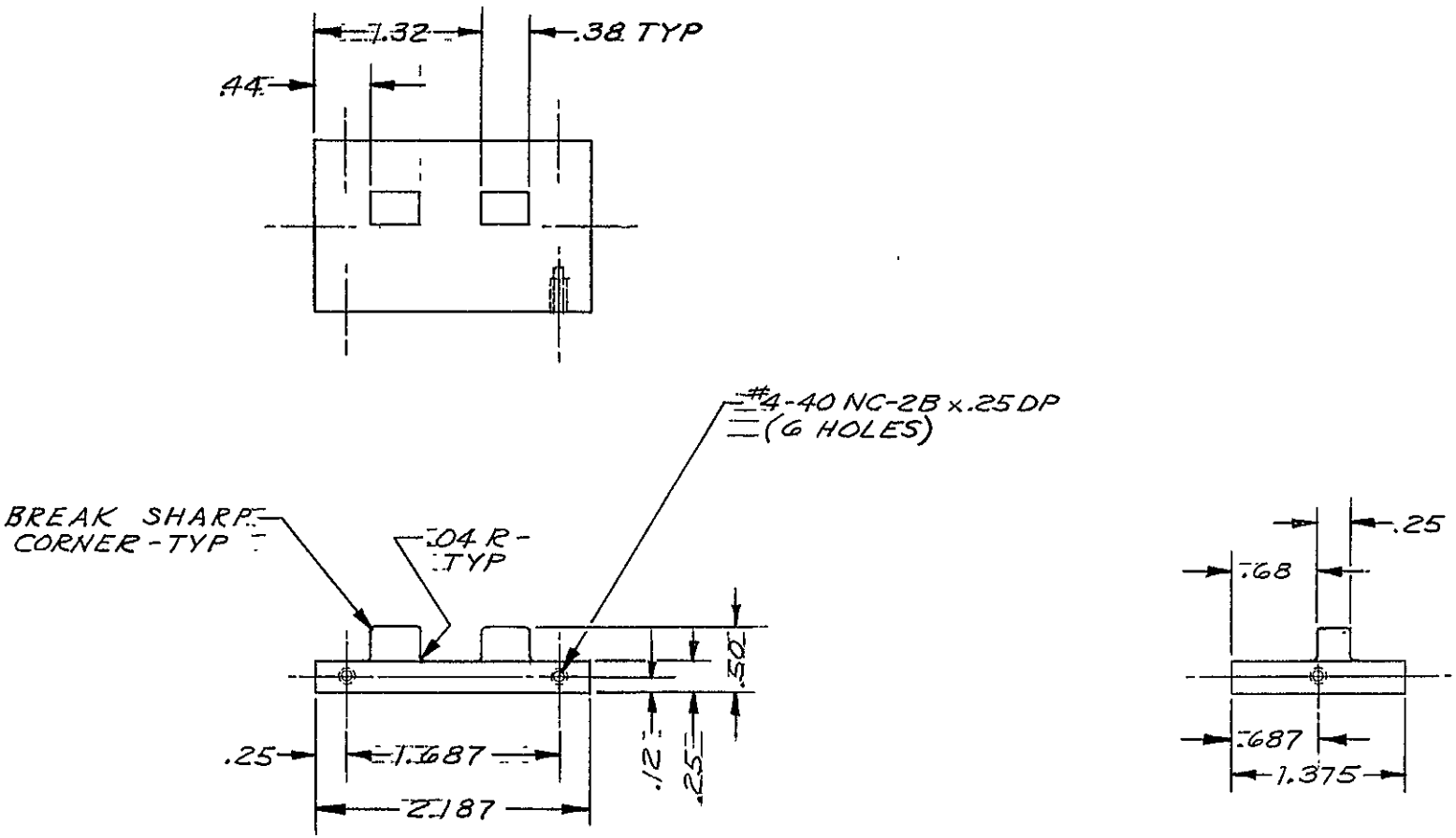

Figure 1-50 Plate, End-Actuator 8338429

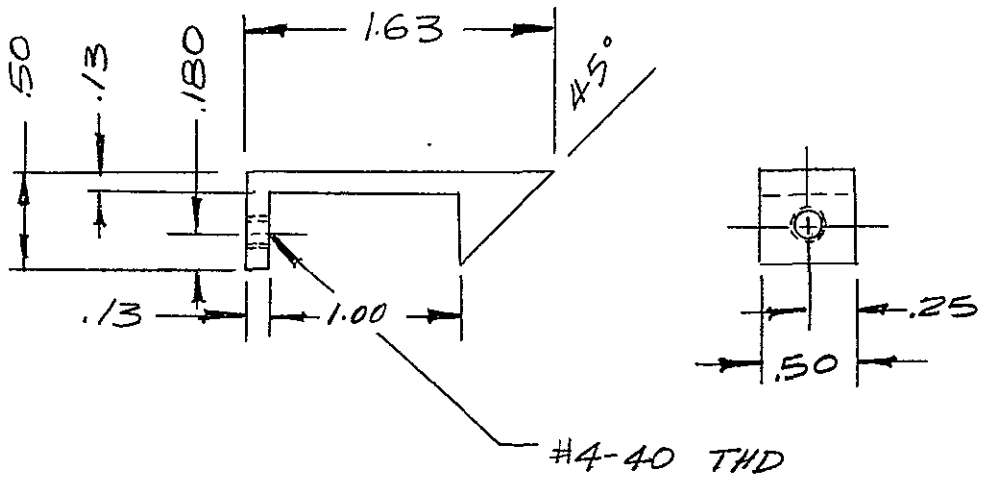

Figure 1-51 Bracket, Bottom - 45 Degree LA Cooler 8113991

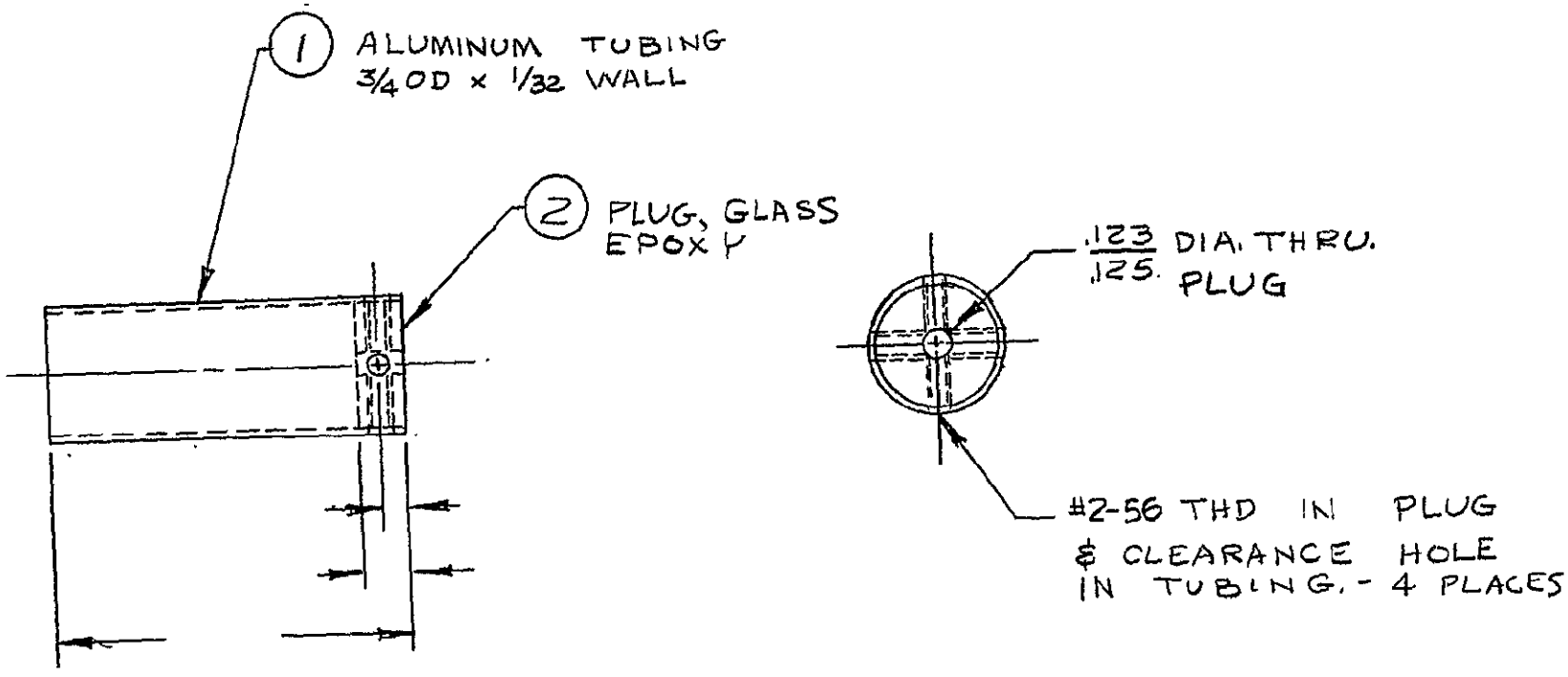

Figure 1-52 Tube, Support - 45 Degree LA Cooler 8113993

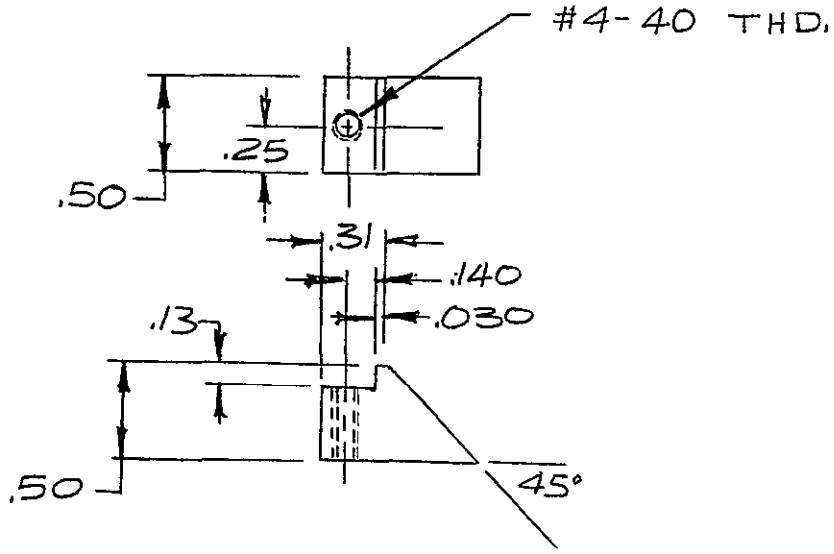

Figure 1-53 Bracket, Top - 45 Degree LA Cooler 8113995

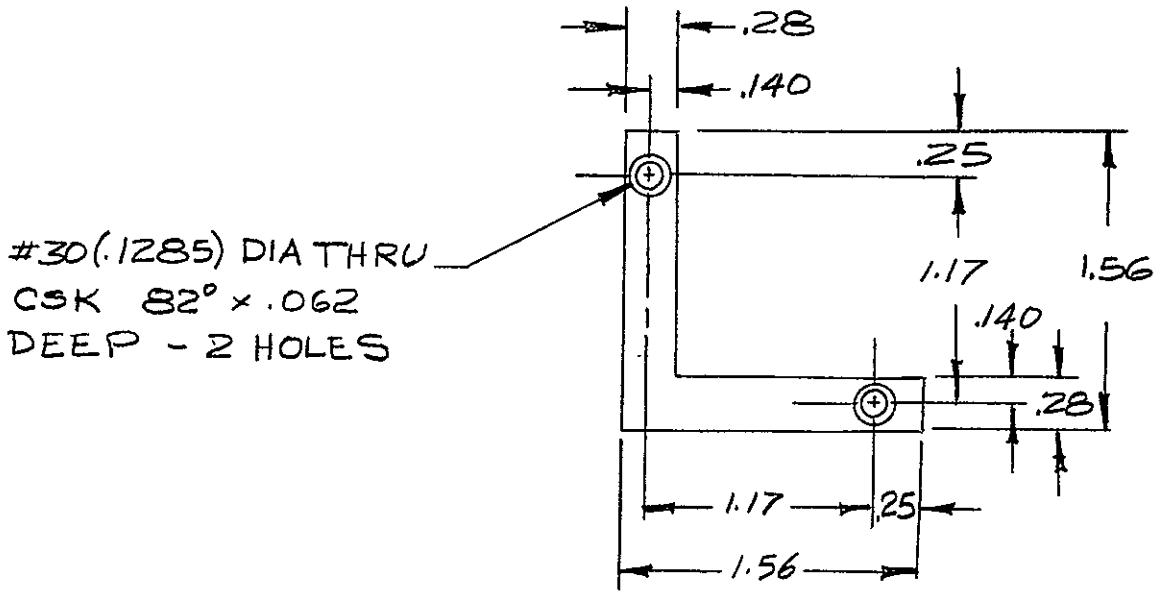

Figu:

Figure 1-54 Angle, Support - 45 Degree LA Cooler 8113996

1.2 Cone Surface Properties

Obtaining a low radiative coupling between the cone walls and patch has been a continuing problem in radiant coolers. Based on specular reflection at the walls, the apparent or effective cone surface emissivity has consistently exceeded the hemispherical emissivity. Analysis of the HRIR single-stage cooler (1) (see list of references in Section 1.2.3) showed that the apparent surface emissivity of the cone walls was in the range from 0.062 to 0.86, considerably above the hemispherical emissivity of a gold-coated surface (0.02 to 0.05). The cone wall surfaces of the two-stage radiant cooler showed an effective emissivity of 0.07 when the hemispherical emissivity was 0.05 (2). This seemed to be largely the result of waves and wrinkles in the aluminzed mylar used as a cone wall reflector.

The design and analysis of radiant coolers after completion of the work described in Reference 2 has therefore been based on an apparent specular emissivity of 0.05 to 0.07. We felt that a maximum value equal to that of wavy aluminized mylar surface should be easy to achieve. Alas, such was not the case. The most recent and best documented example is the single-stage cooler designed for the ITOS radiometer. A careful and accurate analysis was made using the specular reflection model and an apparent cone wall emissivity of 0.07. Experimental results, however, indicated an apparent emissivity about twice this value (3). On top of that, the measured hemispherical emissivity of a reflector prepared according to the procedure used in this cooler had the satisfyingly low value of 0.017 ± 0.0015 (4).

The large relative increase in the apparent cone surface emissivity may be the result of:

a. The increase in emissivity of a metallic reflector with an increase in emission angle relative to the surface normal.

b. A diffuse, or in general non-specular, component of reflection.

c. Surface cavities which introduce additional cone wall reflections.

A study of the first effect has shown that it produces only relatively small increases in the apparent emissivity (Section 1.2.1). Samples of epoxy-coated aluminum with significant surface cavities have been produced (4). The surface looked irregular to the eye. Its emissivity was about four times that of a sample spray-coated with polyurethane varnish (ITOS procedure) and a strong function of the emission angles covered. For example, the emissivity over an entire hemisphere was 0.07, but it decreased to 0.032 when the emission was restricted to angles less than 72° from the surface normal. On the other hand, when the surface irregularities have small slopes, the cavity effect is small or entirely absent. In particular, such cavities were not present in the spray-coated surfaces.

The cause for the large increase in the specular emissivity of cone wall surfaces as seen from the patch in a radiant cooler therefore seems to be non-specular component of reflection at the surfaces. In the limiting (worst) case, if a small

fraction δ of the reflection is diffuse and the hemispherical emissivity is ϵ, the apparent specular emissivity is $\epsilon + \delta$ [5]. Thus for $\epsilon = 0.02$ and $\delta = 0.02$ (2% diffuse reflection), the apparent emissivity is 0.04 or twice the hemispherical value. The limiting case occurs for concentric or coaxial geometries. The radiative exchange is then a minimum for specular reflection at the outer surface and a maximum for diffuse reflection [6].

The nature of the reflection at a surface is a very sensitive function of its roughness (Section 1.2.2). For example, a root-mean-square roughness (the rms deviation of the surface from a plane representing the mean height) of only 0.008 of the wavelength of the incident radiation produces a fractional non-specular reflection component of 0.01 or 1%. The use of optically polished cone surfaces is therefore indicated even for use at the wavelengths associated with cone wall emission. Some experimental verification of this is given in Section 2.0.

The theory and experiments of Bennett and Porteus (Section 1.2.2), provide an explanation of past results with cone wall surfaces. A metallic film evaporated onto a rough surface will, for the most part, replicate the roughness of the surface. The roughness of a rolled, cold drawn, or machined surface [7] will produce a large component of non-specular reflection at the wavelengths of interest. Coating the surface with an epoxy or plastic will reduce the roughness and therefore the non-specular component. At the same time, the apparent specular emissivity as seen from the patch will decrease. However, the epoxy or plastic surface is still rough compared to an optically polished surface. Also, an additional non-specular reflection component is introduced by scattering off bubbles, dust, and other included matter. Finally, the irregularities of the slope must be kept small to prevent the introduction of surface cavities. All these factors indicate that the entire epoxy coating process would tend to by non-reproducible.

The details of surface roughness studied by Bennett and Porteus are described in Section 1.2.2 and are used to make an estimate of the optical finish required for the cone walls of a radiant coller. A specification on the cone walls for the multi-element radiant cooler is given in the Appendix.

1.2.1 Directional Emissivity of a Metallic Reflector

The emissivity of an optically smooth metallic reflector as a function of angle θ from the surface normal may be derived from Fresnel's equations for the reflection of electromagnetic waves. The results for unpolarized radiation are [8]

$$\epsilon(\theta) = 1/2 \cdot \epsilon_{\perp}(\theta) \left[\frac{a^2 + b^2 + \sin^2 \theta}{\cos^2 \theta \cdot (a^2 + b^2 + 2a \sin \theta \tan \theta + \sin^2 \tan^2 \theta} \right]$$

where $\epsilon_{\perp}(\theta) = \dfrac{4a \cos\theta}{a^2 + b^2 + 2a\cos\theta + \cos^2\theta}$

$$a^2 + b^2 = \left[(n^2 - k^2 - \sin^2\theta)^2 + 4n^2 k^2\right]^{1/2}$$

$$2a = \sqrt{2} \times \left[a^2 + b^2 + n^2 - k^2 - \sin^2\theta\right]^{1/2}$$

n = refractive index

k = extinction coefficient.

If $\epsilon(\theta)$ is represented as function of $\sin^2\theta$ using linear coordinates, the area under the resultant curve is equal to the hemispherical emissivity [9]. And, in general, the emissivity over a partial hemisphere from $\sin^2\theta = c$ to $\sin^2\theta = 1$ is given by

$$\epsilon(\Delta\theta) = \frac{1}{1-c} \int_c^1 \epsilon(x) \cdot dx,$$

where $x = \sin^2\theta$.

The values of n and k for good conductors in the infrared wavelength region may be calculated from the Drude-Zener theory [10]. Bennett, Silver, and Ashley[11] show that agreement between their theory and experimental measurements in the case of evaporated aluminum requires that the film be prepared under ultra-high vacuum conditions (10^{-8} to 10^{-9} Torr). The mathematical expressions used by Bennett, et. al., are

$$n^2 - k^2 = 1 - \frac{\omega_p^2}{\omega^2 + \frac{1}{\gamma^2}}$$

$$nk = \frac{1}{2\omega\gamma}\left[\frac{\omega_p^2}{\omega^2 + \frac{1}{\gamma^2}}\right]$$

where ω is the angular frequency and γ the relaxation time. The plasma frequency ω_p is given by

$$\omega_p = \left(\frac{4 \pi \quad N_{eff} e^2}{m} \right)^{1/2}$$

where for a metal N_{eff} is the "effective" free-electron density, e the electronic charge, and m the free electron mass.

The relaxation time is the interval between collisions of an electron with the lattice and is given by

$$\gamma = \frac{m \sigma_o}{N_{eff} e^2}$$

where σ_o is the bulk d-c conductivity.

The penetration of the reflected electromagnetic wave into the metallic film is measured by its optical skin depth

$$\delta = \frac{\lambda}{2 \pi k}$$

or the distance in which the amplitude of the electric vector drops to 1/e of its initial value (and the intensity of the reflected wave to $1/e^2$). For $\lambda = 20$ μm and k = 164, δ is 0.0194 μ m or 7.64×10^{-7} inch.

The directional emissivity $\epsilon(\theta)$ of UHF aluminum was determined for angles (θ) from 0° to 90° using the calculated values of n and k at the wavelength of 20 μ m (81.9 and 164, respectively). The results are listed in Table 1-2 in terms of $x = \sin^2 \theta$.

The partial hemispherical emissivity $\epsilon(\Delta \theta)$ over the range from x = c to x = 1 was calculated using a summation approximation to the integral. The results are given in Table 1-3 for the range from c = 0 to c = 0.50 or $\theta = 45^o$. The value for c = 0 is the emissivity over an entire hemisphere or simply the hemispherical emissivity. It has a value 1.33 times that of the normal emissivity ($\epsilon(\theta)$ at $\theta = 0^o$), the theoretical limiting ratio for a high conductivity metal [16]. The partial hemispherical emissivity over the angular range from 45° to 90° is 23.6% larger than the hemispherical emissivity.

Table 1-2 Directional Emissivity of UHV Aluminum

x	ϵ (x)	x	ϵ (x)
0	0.009701	0.62	0.010841
0.02	0.009702	0.64	0.020974
0.04	0.009703	0.66	0.011124
0.06	0.009706	0.68	0.011292
0.08	0.009710	0.70	0.011483
0.10	0.009715	0.72	0.011700
0.12	0.009721	0.74	0.011948
0.14	0.009729	0.76	0.012233
0.16	0.009738	0.78	0.012565
0.18	0.009748	0.80	0.012956
0.20	0.009761	0.82	0.013421
0.22	0.009775	0.84	0.013984
0.24	0.009792	0.86	0.014678
0.26	0.009810	0.88	0.015559
0.28	0.009831	0.90	0.016715
0.30	0.009854	0.92	0.018313
0.32	0.009880	0.94	0.020695
0.34	0.009908	0.96	0.024750
0.36	0.009940	0.98	0.033961
0.38	0.009976	0.99	0.046836
0.40	0.010015	0.999	0.130358
0.42	0.010058	0.9999	0.273129
0.44	0.010106	0.99995	0.301789
0.46	0.010158	0.99996	0.306524
0.48	0.010217	0.99997	0.308839
0.50	0.010281	0.99998	0.304665
0.52	0.010352	0.99999	0.279402
0.54	0.010430	0.999999	0.136803
0.56	0.010517	1	0
0.58	0.010614		
0.60	0.010721		

Table 1-3 Partial Hemispherical Emissivity of UHV Aluminum

c	ϵ (Δx)	c	ϵ (Δx)
0	0.012941	0.26	0.014068
0.02	0.013008	0.28	0.014186
0.04	0.013076	0.30	0.014310
0.06	0.013148	0.32	0.014441
0.08	0.013223	0.34	0.014578
0.10	0.013301	0.36	0.014724
0.12	0.013382	0.38	0.014877
0.14	0.013467	0.40	0.015040
0.16	0.013556	0.42	0.015212
0.18	0.013649	0.44	0.015396
0.20	0.013747	0.46	0.015590
0.22	0.013848	0.48	0.015796
0.24	0.013955	0.50	0.016020

Table 1-4 Surface Quality Required For Specified Specularity

R_s/R_o	σ/λ
0.99	0.00798
0.98	0.01131
0.97	0.01389
0.96	0.01608
0.95	0.01802
0.94	0.01979
0.93	0.02144
0.92	0.02298
0.91	0.02444
0.90	0.02583
0.80	0.03759
0.70	0.04753
0.60	0.05688
0.50	0.06625
0.40	0.07617
0.30	0.08732
0.20	0.10095
0.10	0.12075
0.05	0.13773
0.02	0.15739
0.01	0.17077

1.2.2 Relation Between Surface Roughness and Specular Reflectance

Davies [17] developed an expression relating specular reflectance and rms roughness by means of a statistical treatment of reflection of electro-magnetic waves from a rough surface. The theory was extended to the optical region (visible and infrared) by Bennett and Porteus [18-20]. The subject is also covered in a book by Beckman and Spizzichino [21]. When multiple reflections (cavity effects) are negligible, the principal effect of surface roughness is to convert part of the specular reflectance into non-specular while maintaining the total reflectance equal to that of a perfectly smooth surface of the same material.

For a root mean square deviation σ of the surface from its mean surface limit and a wavelength λ, the specular reflectance at normal incidence is given by

$$R_s = R_o \exp \left[- (4 \pi \sigma / \lambda)^2 \right]$$

where R_o is the (specular) reflectance when the surface is perfectly smooth. This relation holds for all values of σ / λ when the surface height distribution is Gaussian[21]. Experimentally, it has been shown [19] that ground glass (including Pyrex and fused quartz) has a Gaussian height distribution except for the most finely ground surfaces. And even the most finely ground are approximately Gaussian at small values of σ / λ.

The required values of σ / λ are given in Table 1-4 for specified values of relative specular reflectance R_s / R_o at normal incidence.

The normal reflectivity for metals in the infrared is given by [11]

$$R = 1 - (2 \omega / \pi \sigma_o)^{1/2} \cdot \left[(1 + \omega^2 \gamma^2)^{1/2} - \omega \gamma \right]^{1/2}$$

where σ_o is in electrostatic units. At very long wavelengths ($\omega \gamma \ll 1$), this becomes the Hagen-Rubens relation

$$R = 1 - (2 \omega / \pi \sigma_o)^{1/2}$$

This equation predicts that the emissivity is inversely proportional to the square root of the wavelength, in sharp disagreement with experimental data on metals in the infrared. In fact, the original measurements by Hagen and Rubens showed agreement only at 25.5 μm for heated samples [12].

Experimental measurements [11, 13] show that the emissivity of metallic reflectors varies only slowly with wavelength in the infrared region, a fact noted by Scott [14]. Unfortunately, some theoretical studies of the radiative transfer between low-emissivity specular surfaces at and below room temperature have been based on the Hagen-Rubens relation (e.g., [15].

For aluminum, the d-c bulk conductivity is 3.178×10^{17} esu and the number of effective free electronic/atom, 2.6. The number of atoms in a cubic centimeter of Al (at 20°C) is

$$6.025 \times 10^{23} \quad \frac{\text{atoms}}{\text{gm-moles}} \times \frac{2.70}{26.98} \quad \frac{\text{gm-moles}}{\text{cm}^3} = 6.029 \times 10^{22}.$$

so that

$$N_{eff} = 1.568 \times 10^{23} \text{ electrons/cm}^3 ,$$

The corresponding relaxation time is

$$\gamma = 8.002 \times 10^{-15} \text{ sec}$$

for $m = 9.108 \times 10^{-28}$ gms and $e = 4.803 \times 10^{-10}$ esu, and the plasma frequency

$$\omega_p = 2.230 \times 10^{16} \text{ radians/sec.}$$

As previously noted, the infrared emissivity of a metallic film is a weak function of wavelength. We may therefore select a representative wavelength, say 20 μ m, for the emission from a surface in the temperature range typical of cone walls in a radiant cooler. For aluminum at 20 μ m, we obtain

$$n = 81.9$$

$$k = 164$$

At non-normal incidence to a first approximation, σ is replaced by $\sigma \cdot \cos\theta$ where θ is the incidence angle with respect to the surface normal (3).

The non-specular reflectance pattern is not diffuse in the sense that the radiance is independent of θ. For normal incidence, the fraction of non-specular (called incoherent in [20]) radiation that is scattered into an angle between θ and $\theta + d\theta$ is given by

$$\gamma d(\theta) = R_o \cdot 2\pi^4 \cdot (a/\lambda)^2 \cdot (1 + \cos\theta)^4 \cdot \sin\theta \cdot \left(\frac{\sigma}{\lambda}\right)^2 \times \exp\left[-(\pi a \sin\theta/\lambda)^2\right] \cdot d\theta$$

where a is the autocovariance length or correlation distance. If m is the root mean square slope of profile of the surface, it can be shown that ([18] Appendix)

$$a = \sqrt{2}\,\sigma/m \quad .$$

For small values of σ/λ, the exponential in the equation for $\gamma_d(\theta) \cdot d\theta$ is unity, and the angular dependence is given by $(1 + \cos\theta)^4 \cdot \sin\theta$. The normalized values of this function are plotted in Figure 1-55 together with those for a diffuse reflector ($\sin\theta \cdot \cos\theta$). The difference between the curves is not large. The solid dots show the normalized values of $\gamma_d(\theta) \cdot d\theta$ for $\sigma/\lambda = 0.1$ ($R_s/R_o \approx 0.2$) and m = 1. Increased surface roughness increases the relative non-specular reflectance at small angles to the surface normal (for normal incidence).

The adverse effect on a radiant cooler of even a small amount of diffuse reflection was discussed earlier. This effect apparently extends to other geometrics. For example, Feldmanis [23] found that it was not necessary to considere specularly reflecting surfaces or to use a complex formulation in the thermal analysis of a space vehicle, but that experimental measurements agreed best with a simple diffuse model. The same held for the plane-parallel and perpendicular plate geometries studied by Viskanta, et. al. [22]. Even for R_s/R_o in the range from 0.75 to 0.38, the measured distribution of radiant incidence across the surfaces agreed best with the simple diffuse model. One of the samples studied had a surface of smooth electroplated gold with $\sigma/\lambda \approx 0.007$, which should be highly specular ($R_s/R_o \approx 0.99$). The measurements were compared only with the simple diffuse and non-directional specular models; they agreed better with the diffuse. No explanation was offered for this, but Figure 15 of the report indicates that a directional specular model (i.e., including the emissivity as a function of θ) would account for most of the difference between the simple specular model and the experimental data. Unfortunately, directional specular calculations were not made for the smooth gold sample.

In order to obtain the desired value of R_s/R_o, the surface roughness must be related to the surface optical deviations. If a Gaussian height distribution of surface irregularities is assumed, σ is related to the maximum (peak-to-peak) surface irregularity σ_{pp} by [24]

$$\sigma = \frac{\sigma_{pp}}{2\sqrt{2}}$$

The measurement of σ_{pp} by means of multiple beam fringes of equal chromatic order is described by Dietz and Bennett [24].

Now the cone radiates as an approximately greybody with a representative wavelength of 20 μm. The fraction p of greybody radiation beyond 20 μm is given in Table 1-5 for the usual range of cone wall temperatures T_c.

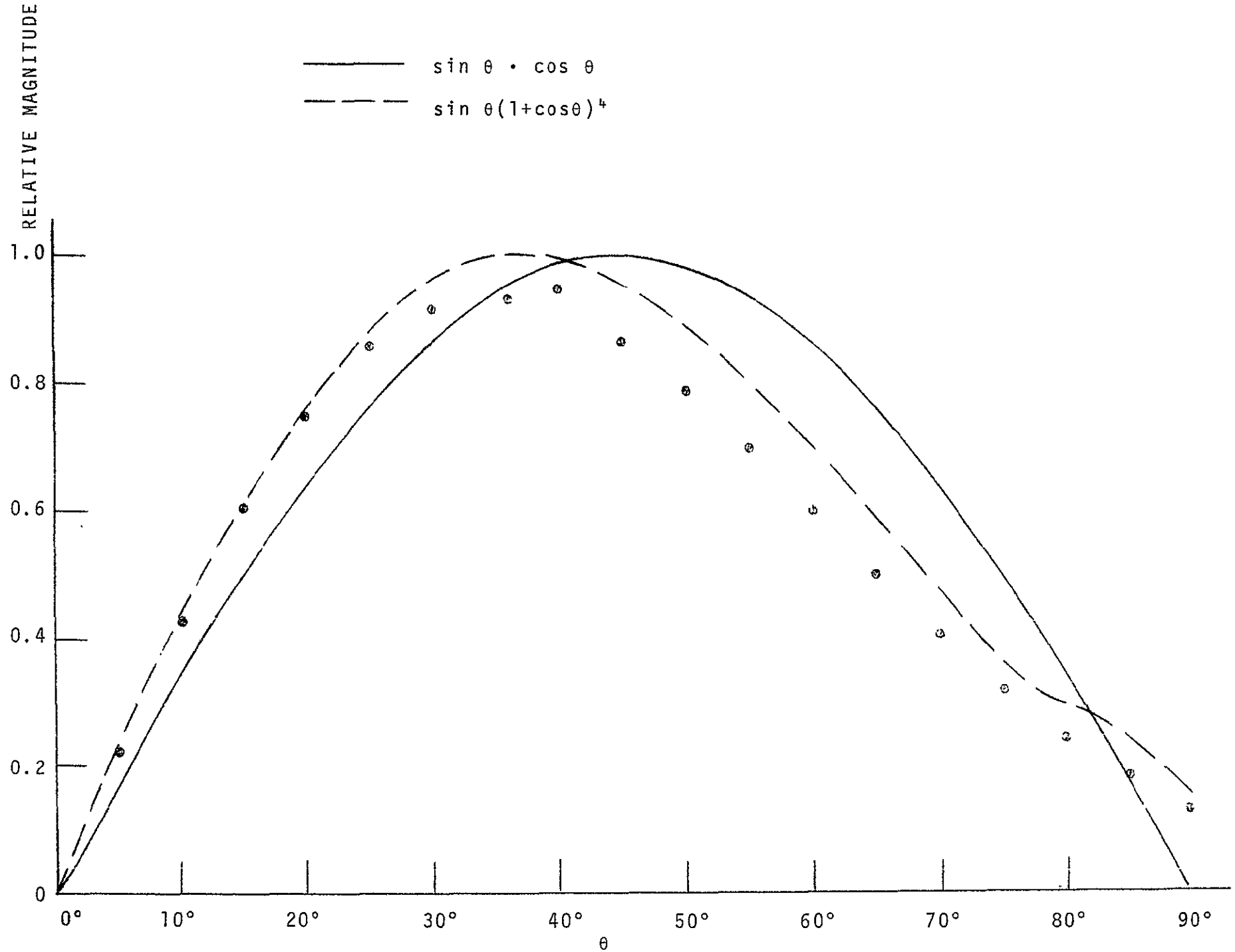

Figure 1-55. Reflectance Distribution Curves

Table 1-5 Fraction of Cone Wall Radiation Beyond 20 μ m

Tc (K)	p ($\lambda > 20\ \mu$ m)
200	0.518
190	0.555
180	0.595
170	0.637
160	0.681
150	0.725

We will use values of $\sigma/\lambda = 20\ \mu$ m as the measuring point for cone wall roughness. Since surface deviations are usually measured in the visible using sodium light at a wavelength λvis of 0.5893 μ m, we need to know the corresponding irregularity σ_{pp}/λvis:

$$\frac{\sigma_{pp}}{\lambda_{vis}} = 2 \cdot \sqrt{2} \cdot \frac{\sigma}{\lambda} \cdot \frac{\lambda}{\lambda_{vis}} = 96.65 \frac{\sigma}{\lambda}$$

The visibly measured surface irregularity corresponding to a specified reflectance ratio R_s/R_o at 20 μ m is given in Table 1-6.

Table 1-6 Required Surface Irregularity in the Visible For Specified Specularity at 20 μ m

R_s/R_o (20 μ m)	$\sigma_{pp}/\lambda_{vis}$ (wavelength)
0.99	0.77
0.98	1.09
0.97	1.33
0.96	1.54

A surface polished to be flat will have an irregularity of about 1/5th to 1/10th its deviation from flatness. Therefore, a surface having an irregularity of 0.77 wavelength must be flat to within 3.85 to 7.7 wavelengths (7.7 to 15.4 fringes).

Rather than specify the surface irregularity (which determines R_s/R_o), we could specify the flatness as measured on the polishing block. The sphericity (overall surface curvature) introduced upon removal from the polishing block is no problem and should not change the irregularity. An on-the-block flatness of I wavelength (of visible light) would then ensure an R_s/R_o value of greater than 0.99 at wavelengths of 20 μ m and larger. In addition, it should be noted that a ratio 0.99 at 20 μ m at normal incidence results in the same ratio at 10 μ m when radiation is incident at 60° from the surface normal.

1.2.3 References

1. R. V. Annable, R. A Harber, and H. A. Leiter, First Quarterly Report (Design Study Report) For a Day-Night High Resolution Infrared Radiometer Employing Two-Stage Radiant Cooling, Contract NAS5-10113, May 1966, Appendix II.

2. R. V. Annable, et. al., Final Report For a Day-Night High Resolution Infrared Radiometer Employing Two-Stage Radiant Cooling, Part I, Contract NAS 5-10113.

3. W. H. Wallschlaeger, et. al., Final Report, Development of a Single Stage Radiant Cooler For the ITOS VHRR, Contract NAS5-10491 (Mod. 12), June 1970, p. 3-13.

4. R. V. Annable, Final Report For Radiant Cooler Design and Emissivity Study, Part II, December 1969, Section 3.0.

5. R. V. Annable, Appl. Opt. 9, 185, 1970.

6. M. Jakob, Heat Transfer, Vol. II, John Wiley, 1957.

7. ASTME Tool Engineers Handbook, McGraw-Hill, 1959, Section 89.

8. E. M. Sparrow and R. D. Cess, Radiation Heat Transfer, Brooks/Cole, 1966, Section 2.3.

9. H. C. Hottel and A. F. Sarofim, Radiative Transfer, McGraw-Hill, 1967.

10. F. Seitz, The Modern Theory of Solids, McGraw-Hill, 1940, p.638.

11. H. E. Bennett, M. Silver, and E. J. Ashley, Jour. Opt. Soc. Am. 53, 1089, 1963.

12. Reference 9, Section 4.10.

13. J. M. Bennett and E. J. Ashley, Appl. Opt. 4, 221, 1965.

14. R. B. Scott, Cryogenic Engineering. D. Van Nostrand, 1959, Section 10.15.

15. V. E. Holt, R. J. Grosh and R. Geynet, Bell Sys. Tech. Jour. 41, 1865, 1962.

16. M. Jakob, Heat Transfer, Vol. I, John Wiley, 1949, pp 34-52.

17. H. Davies, Proc. Inst. Elec. Engrs. 101, 209 (1954).

18. H. E. Bennett and J. O. Porteus, Jour. Opt. Soc. Am. 51, 123 (1961).

19. H. E. Bennett, Jour. Opt. Soc. Am. 53, 1389 (1963).

20. J. O. Porteus, Jour. Opt. Soc. Am. 53, 1394 (1963).

21. P. Beckmann and A. Spizzichino, The Scattering of Electromagnetic Waves from Rough Surfaces, Pergamon Press, Inc., New York, 1963.

22. R. Viskanta, J. R. Schornhorst, and J. S. Toor, Analysis and Experiment of Radiant Heat Exchange Between Simply Arranged Surfaces, AFFDL-TR-67-94, Wright-Patterson AFB, Ohio, June 1967.

23. C. J. Feldmanis, Thermal Test of a Model Space Vehicle, Part II - Experimental Results and Comparison with Analysis, AFFDL-TR-67-42, Wright-Patterson AFB, Ohio, August 1968.

24. R. W. Dietz and J. M. Bennett, Appl. Opt. 5, 881 (1966).

1.3 Anti-Frost Design

The structure and operation of the radiant cooler must be designed to minimize the condensation of water vapor and other contaminants on optical components and sensitive cooler surfaces. To begin with, the compartments within the cooler are sealed from each other and from the instrument housing. For this purpose, windows are placed on the optical ports connecting the housing with the cooler and the cone enclosure with the patch enclosure (Section 1.3.3). Next, each cooler compartment (the cone compartment between the housing and outer cone structure and the patch compartment between the cone structure and patches) must be efficiently outgassed prior to cooler operation. Thirdly, the optical ports must be protected against contamination by residual internal outgassing products and by the ambient spacecraft atmosphere. Finally, provision must be made for driving off contaiminants accumulated on the optics or on sensitive cooler surfaces.

To accomplish the initial outgassing, cooler operation is delayed by means of a cover over the cone mouth (Section 1.1) and by heaters on the cone walls and patches. If possible, the heaters should raise the cooler temperature to above ambient. A 10 percent change in absolute temperature changes the outgassing rate by about 10:1, according to Scialdone and Viehmann (Report of the Findings of the Radiation Cooler Task Group, Appendix VI, Sept 11, 1970). Thus, a temperature of 55 degrees C, or about 10 percent above room temperature on an absolute scale, would be desirable. The patch temperatures, of course, should not exceed the limit set by the detector elements (about 80 degrees C for HgCdTe). After a certain time interval, the materials within the cooler compartments will reach their steady-state or residual outgassing (weight loss) rates. Materials with low residual rates should therefore be used and the surface areas of the multilayer insulation kept as small as possible consistent with the thermal insulation requirements.

With the cooler at its operating temperatures, both the internal residual outgassing and the ambient spacecraft atmosphere are sources of contaminants. The cooler should then be designed to keep deposits off the optical ports on both the patches and cone structure. A cold surface in the vicinity of the optical openings on the patches can be used to trap moisture before it reaches the windows. These traps also serve to divert the gas flow away from the patch opening during the initial outgassing period prior to cooler operation. Baffles can be used to block the flow of residual insulation outgassing products to the optical ports. The cold traps are used in place of the anti-frost enclosure (Section 6.3 of the design study report).

In support of this approach, tests performed on Contract NAS5-21112 (SCMR for Nimbus E) have shown that a polyimide antifrost enclosure acts as a (conductive and radiative) condenser to significantly increase the radiative input through the optical opening from the cone (window) to the patch. The enhancement of radiative coupling was observed during the testing of the enclosure and during the testing of a breadboard model of the SCMR cooler. In the first case, a 220 degree C blackbody at a fixed distance was viewed through a chopper by a cooled PbSe detector. Insertion of the enclosure (including an infrared window) increased the detector signal from the blackbody.

tained not only on the patches but also on the other cooler parts without the presence of cold space targets and shrouds in the immediate vicinity of the cooler.

Previous tests have shown that it is possible to design and operate a radiant cooler so that water vapor or other contaminants from the vicinity of the patch do not impair its operation. For example, extensive testing of radiant coolers for the ITOS-VHRR (patch temperatures of 85 to 100K; Contract NAS5-10491) has never revealed any evidence of ice on the detector optics sufficient to degrade the sensitivity of the instrument. In this design, the detector is in a second-stage patch that is surrounded by a first-stage patch. The first-stage may then act as a simple cold trap for the second-stage. Moreover, the detector package is relatively distant from the major paths for gas leaving the space between the patch assembly and cone structure. In addition, the cone is sealed (by the spectral filter) from the rest of the instrument, so that outside products cannot pass by the cold patches. The chamber pressure is initially reduced to about 2×10^{-6} Torr (it is probably higher in the insulation blankets) and the cryopanels turned on. The final chamber pressure is typically 5×10^{-7} Torr. The operation should be improved further by heating the cooler parts (patches and cones) during pumpdown.

1.3.1 Outgassing of Patch Insulation

The volume below the patches in the multi-element radiant cooler is sealed from the rest of the cooler. As a result, instrument outgassing products that can condense on the patches must come from this volume. The source of outgassing is the multilayer insulation between the patch and the cone structure. If the insulation is allowed to outgas at room temperature for a sufficient length of time prior to cooler operation, the residual outgassing rate will be so small that it will not degrade sensitivity for a long time. For example, we may begin with the data given by Scialdone and Viehmann for an as-received stack of insulation (Figure 3 to Appendix VI of the LaGow Committee Report). If this stack is pumped for 2,000 mins (33.3 hrs) and if the outgassing rate remains constant beyond that time, it is shown below that a 10 percent reduction in signal requires 64 to 310 days, depending on the wavelength. This result assumes that the outgassing product is water that is uniformly deposited as ice on the rear surfaces of the patches. However, the reduction in temperature of the insulation during cooler operation should so reduce the residual outgassing rate that it would not limit the operating time of the radiant cooler.

If G is the outgassing rate in torr-liters cm^{-2} sec^{-1} of equivalent air, the outgassing rate for water in $gm.cm^{-2}$ sec^{-1} is (Scialdone and Viehmann, op. cit.).

$$G \times 1.7 \times 10^{-3} \times 18/29 = 1.1 \times 10^{-3}\ G$$

There are about 20 layers (10 pairs) of multilayer in the main stack between the patches and cone structure. Each layer has an area of about 100 in^4 including the end pieces. Counting both sides of the layers, this is a total of 4×10^3 in^2 or 2.6×10^4 cm^2. The total outgassing rate is then 29G grams of water per second.

In the second case, the insertion of two enclosures produced a thermal input sufficient to increase a 100K SCMR cooler patch to 125K. This was true even when a thin section was removed from each enclosure next to the cone in order to disconnect its conductive paths. There were no spectral filters or germanium windows on the patch during these tests, only black openings. Addition of the germanium should reduce the higher temperature to 117K, still a very large increase. Apparently, the inside of the enclosure would have to be blackened to eliminate the condenser effect. This would, of course, increase the conductive and radiative coupling through the enclosure.

Finally, the operation of the instrument may eventually be impaired either thermally or optically by the accumulation of frost or other contaminants. Cooler operation is then interrupted by closing the cone cover and reheating the cone and patches to drive off the condensed material. A successful anti-frost design would be one in which the time between such interruptions is large, say a significant fraction of the instrument's orbital lifetime.

The initial and residual outgassing of the insulation below the patches are studied in Section 1.3.1. The study indicates that patch contamination from this source should not be a problem if the patch compartment is sealed from the rest of the instrument and well outgassed prior to operation of the cooler. A literature review on the subject of multilayer insulation is discussed in Section 1.3.4. The construction of patch cold traps and insulation baffles are covered in Section 1.3.3. The saturation of cold traps is studied in Section 1.3.2.

Because residual outgassing can be made very small, especially at the operating temperatures of the cooler (Section 1.3.1), we do not recommend that additional paths (e.g., through the cone end radiator) for outgassing to the outside be provided to the patch compartment. However, we do recommend that the insulation before the patch be perforated (This was done in the breadboard cooler; see Section 1.3.4). Moreover, we recommend that baffles not be employed in the patch compartment to block the flow of residual outgassing products to the optical ports. Such baffles restrict the flow during initial outgassing and, if the initial outgassing is done properly, the residual outgassing at operating temperatures will not be the limit on operation time. Rather the limit will be the contamination from the spacecraft atmosphere (Section 1.3.2). For this reason, we also recommend that the cold traps around the patch optical openings be supplemented in future designs by traps around the entire periphery of the patches at the cone opening. Such traps protect the insulation and low-emissivity rear surface of the patch as well as the optical ports.

Finally, it should be pointed out that a proper test of the anti-frost design of a radiant cooler can be carried out in a space chamber with respect to the initial outgassing and the contamination produced by residual internal outgassing. Procedures used during the test must be realistic in the sense that they can also be followed in orbit. However, a proper test with respect to contamination produced by the spacecraft atmosphere is considerably more difficult. It would require the exposure of a cooler to the expected pressures and constituents before and after initiation of cooler operation. During cooler operation, the correct temperatures would have to be main-

We will assume that all of the outgassed water is deposited as ice or frost uniformly on the rear surfaces of the patches. The rear surfaces have an area of about 16.6 in^2 or 107 cm^2 (p. 4-2 of the design study report). Assuming a density of 1 gm cm^{-3}, the ice thickness then increases at the rate of 2.3×10^4 G cm day^{-1}.

A critical review of the data on the absorption coefficient and reflectivity of water and ice was made by W. M. Irvine and J. B. Pollack (Icarus 8,324, 1968). Best values were chosen for the complex index of refraction for wavelengths from 0.7 μm to 200 μm. Hexagonal (ordinary) ice crystallizes at temperatures above about -80 degrees C (193 K). Between -80 degrees C and -130 degrees C (143 K), ice may exist in the cubic form, and below -130 degrees C, it may be amorphous. The absorption data at temperatures below -80 degrees C were usually a hexagonal ice formed above -80 degrees C and then cooled. Qualitatively at least, there is little difference in the spectral absorption of the hexagonal and cubic forms.

Using the data from Irvine and Pollack, we see that the maximum absorption over the wavelength span from 4.5 to 25 μm occurs in the band from 5.9 to 6.7 μm, but is almost as high from 11 to 13 μm. The second band is nearly coincident with an atmospheric window widely used in radiometry. The most strongly absorbing region in the entire ice spectrum, however, is located in the band from 2.9 to 3.2 μm.

The transmission through an ice thickness δ is given by

$$T = \exp(-\alpha\delta) = \exp(-4\pi nk\delta/\lambda)$$

where α = absorption coefficient

n = refractive index

k = extinction coefficient

λ = wavelength of radiation.

Thus, for T = 0.90, we have

$$\delta(3.1\ \mu m) = 7.53 \times 10^{-6}\ cm, \quad \alpha = 1.40 \times 10^4\ cm^{-1}$$

$$\delta(11.5\ \mu m) = 8.36 \times 10^{-5}\ cm, \quad \alpha = 1.26 \times 10^3\ cm^{-1}$$

For 2000 minutes of pumping on as-received insulation at 24 degrees C, G is about 4×10^{-12} torr-liter $cm^{-2} \cdot sec^{-1}$ (Figure 4 of Scialdone and Viehmann). The ice thickness growth rate is then 0.92×10^{-7} cm per day. The times required to attenuate the signals by 10% are then

$$t(3.1\ \mu m) = 81 \text{ days}$$

$$t(11.5\ \mu m) = 909 \text{ days} = 2.49 \text{ years}$$

After the cooler has reached its operating temperature, the insulation will be considerably below room temperature. The reduction in temperature would be expected to reduce the outgassing rate. Scialdone and Viehmann state that a rule of thumb is a 10 percent change in absolute temperature changes the outgassing rate by 10:1. If this rule holds at temperatures down to the 90K to 170K range, there would be a large reduction in the residual outgassing rate. For example, the operating cone temperature of design IIIA is about 170K or 40 percent less than room temperature on an absolute scale. The corresponding reduction in outgassing rate is the order of 10^4. We may therefore conclude that patch contamination by instrument outgassing should not be a problem if the volume between the patch and cone structure is sealed from the rest of the instrument and well outgassed prior to operation of the cooler.

1.3.2 Trapping of Spacecraft Contaminants

The condensation or sticking coefficient of a gas or vapor is the ratio of the rate at which molecules condense on a surface to the rate at which they strike the surface. When the surface is in the temperature range of the patches in the multi-element radiant cooler, the sticking coefficient approaches unity (S. Dushman, Scientific Foundations of Vacuum Techniques, 2nd Ed., ed. by J. M. Lafferty, Wiley, 1962, pp. 18 and 176). At the patch temperatures, the ice vapor pressure is much less then that of the incoming vapor. The time to form one monolayer of ice on a surface exposed to the vapor atmosphere is then (J. J. Scialdone, Appendix II, Enclosure 2 to the Report of the Findings of the Radiation Cooler Task Group, Sept. 11, 1970)

$$\frac{\Delta t}{\Delta N} = \frac{6.31 \times 10^{-8} \sqrt{T}}{P} \quad \text{sec./ monolayer,}$$

where T is the vapor temperature in kelvins and P the vapor pressure in torr. A sticking coefficient of one is assumed.

The incoming vapor molecules will have temperatures from about 300K down to the temperature of the cone, or about 170K. Because of the weak dependence on T, we will use T equal to 300K. For a molecular diameter of 4.8×10^{-8} cm, we then obtain

$$\frac{\Delta t}{\Delta N} = \frac{2.64 \times 10^{-4}}{P} \quad \text{days/cm}$$

The cold trap will become saturated when the ice thickness equals the width of the opening or gap in the trap arrangement. The times to saturation are listed in Table 1-7 for a gap of 0.1 cm or 0.04 inch.

Table 1-7

Time to Saturate a Cold Trap with a 0.1 cm Gap

P (torr)	Δt (days)
1×10^{-5}	2.64
1×10^{-6}	26.4
1×10^{-7}	264
1×10^{-8}	2,640

To prevent accumulation of ice on the low-emissivity cone walls, operation of the cooler must be delayed until the spacecraft atmosphere has a pressure of 1×10^{-6} torr or less. This pressure corresponds to a condensation temperature of 160K (I. L. Goldberg in Appendix VII to the Report of the Findings of the Radiation Cooler Task Group, Sept. 11, 1970). The atmosphere around a spacecraft and its decay with time will depend on the vehicle and the instruments on board. Using the data from OGO II and IV (A. W. Mc Cullock in Appendix VIII, ibid.), a pressure of 1 to 3×10^{-8} torr is reached in about 20 days. If cooler operation were delayed for this period of time, saturation of the 0.1 cm gap would not occur for more than 2.4 to 7.2 years. The cycling time for heating of the cooler (interruption of operation) may then be limited by the efficiency of the trap, i.e., the failure to trap all molecules passing through the trap.

1.3.3 Anti-Frost Devices

A design employing both simple cold traps and baffles to protect the optical openings within the patch enclosure is shown in Figure 1-56. The traps and baffles are designed to divert flow away from the optical parts during initial and residual (steady-state) outgassing. The cold traps are designed to capture contaminants from both the residual internal outgassing and the ambient spacecraft atmosphere. During testing of the breadboard cooler (Section 2.1), the baffles were not used. Moreover, future designs would employ the peripheral cold traps described above.

The cold trap on the upper (120K) patch is metallic and does not contact the insulation blanket. The cold trap on the lower (90K) patch is plastic and penetrates the insulation. However, the insulation temperature at the end of the plastic is the order of 120K or as cold as the upper patch. The inside of the metallic cold trap is painted black. The plastic cold trap and the plastic insulation baffles may be either black or highly transmitting in the infrared. The black could be supplied by a paint or

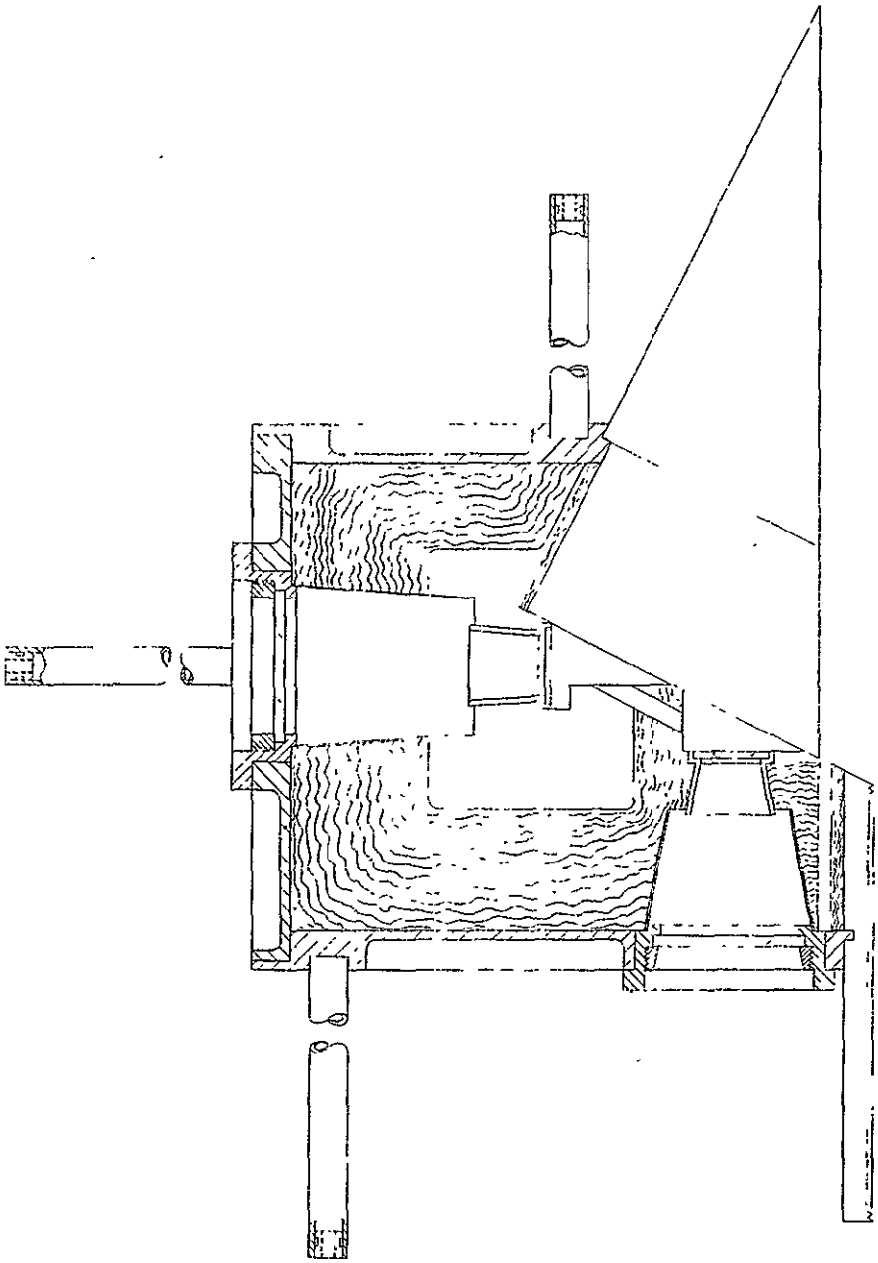

Figure 1-56 Anti-Frost Design

by included carbon particles. A suitable material in either case appears to be high-density polyethylene (see N.W.B. Stone and D. Williams, Appl. Opt. 5, 353, 1966 and J. M. Blea, et. al., Jour. Opt. Soc. Am. 60, 603, 1970). Clear polyethylene was used in the bread-board cooler.

Outgassing of the patch enclosure is aided by perforations in the multilayer insulation .

1.3.4 Optical Port Design

The selection of windows for the optical ports on the cone and patches is discussed in Appendix B to the design study report (July 1970). The cone windows are used to essentially eliminate radiative coupling between the patch and warmer components beyond the cone in the direction of the instrument housing. They also provide mechanical seals for the volume between the patches and cone structure. The optical ports are sealed to prevent outgassing of the instrument and remainder of the cooler through the volume containing the patches.

The cone and patch windows will be the same for the optical ports to the 120K (InAs) patch and the 90K (HgCdTe) patch. The window materials are Intran 2 and germanium, respectively. A germanium window would probably not be used on the 120K patch in an actual instrument. The germanium does not transmit below about 2 μm. However, its thermal performance is comparable to that of a sapphire window, so that it is satisfactory for thermal testing. In addition, the thermal input through the optical opening is not critical to the performance of the 120K patch.

The Irtran 2 cone windows (Eastman Kodak Co.) are 1-inch in diameter and 2 mm thick. The germanium patch windows (Exotic Materials Inc.) are 0.5 inch in diameter and 1 mm thick. All windows have a commercial plate glass finish, 5 wavelengths per inch flatness, and 5 minutes of arc parallelism.

The clear aperture of each patch window will be 0.4 inch after mounting. The divergence angle ψ from the optic axis at the patch window will be based on

$$\tan \psi = 1/2\, f_n = \phi D/2s$$

where f_n = f-number of optics at the patch window

ϕ = instantaneous geometric field of view

D = diameter of entrance aperture

s = side of a detector element sensitive area.

For a typical instrument in the 120K channel,

$$\phi_1 = 0.5 \times 10^{-4}$$

$$D = 25.4 \text{ cm}$$

$$s_1 = 1 \times 10^{-2} \text{ cm}$$

The resultant divergence is

$$\tan \psi = 0.0635$$

To provide for mechanical clearance and tolerance, $\tan \psi_1$ was set at 0.070. In the 90K channel, we used the following values

$$\phi_2 = 1.75 \times 10^{-4}$$

$$D = 25.4 \text{ cm}$$

$$s_2 = 1.5 \times 10^{-2} \text{ cm}$$

In this case, $\tan \psi = 0.148$. Mechanically, a value of 0.150 is used. The field-of-view ratio ϕ_2 / ϕ_1 was set equal to the reciprocal of the detector element ratio (3.5), on the assumption that the channels have the same spatial coverage.

1.3.5 Multilayer Insulation - A Review

We conducted a review of some readily available literature on the subject of multilayer insulation. Some of the articles revealed that the problem of outgassing is not a new one. R. H. Kropschot (Multiple Layer Insulation for Cryogenic Applications, Cryogenics, March 1961, p. 171) discusses the measurement of the effective thermal conductivity of multilayer insulation without perforations or end effects. In his description of the experimental procedure, he states that

> "During evacuation, the sample temperature was maintained at approximately 100 degrees C for about 3 days to help drive the residual moisture from the sample."

J. W. Price (Measuring the Gas Pressure Within a High Performance Insulation Blanket, in Advances in Cryogenic Engineering, Vol. 13, Ed. by K. D. Timmerhaus, Plenum Press, 1968, p. 662) studied the effect of perforations on the performance of multilayer. We tested layers with 1/8 inch diameter holes on 1 inch centers in both directions (1.2 percent areal perforation). The holes were not aligned between layers. He states that

"The (approximately) 1 percent ratio was chosen because analyses showed that this ratio is effective in increasing the evacuation rate and does not materially degrade the thermal efficiency of the insulation."

This was verified by his experiments. He also concludes that the insulation should be preconditioned by means of a vacuum pumpdown, dry gas purge, or both. Finally, he states that there is a problem with insulation evacuation and much of it is a result of material outgassing.

G. C. Vliet and R. M. Coston (Thermal Energy Transport Parallel to the Laminations in Multilayer Insulation, ibid., p. 671) conclude that the lateral conductivity through an insulation blanket depends on its temperature. They studied this effect in samples of crinkled mylar aluminized on one side (NRC-2). The data indicates that radiation transfer along the laminations can be significant and result in much higher parallel conductivity values near room temperature than predicted from conduction through the aluminum film. However, the lateral conductivity drops rapidly with temperature, and below about 100K the "size effect" of the aluminum film limits it to values less than that of the film. From this, we may conclude that radiation transfer along the lamina is important in the insulation of the cone from the instrument housing. When insulating the patches from the cone, however, the temperatures are in the transition region and such radiation "tunneling" is largely gone.

D. O. Murray (Degradation of Multilayer Insulation Systems by Penetrations, ibid, p. 680) discusses techniques for decoupling supports from the insulation blanket. An intermediary insulation (decoupler) is placed around the penetration. The optimum for his setup consisted of a decoupler space on all sides equal to the diameter of the support. Aluminized mylar radiation shields concentric with the support were placed within a concentric wrapping of dexiglas. Unfortunately, the dexiglas or any similar material is a good absorber of water and therefore undesirable. It may be possible to substitute dimpled mylar or other plastic film, possibly with an aluminum coating, or silk veiling, which has a low affinity for water.

2.0 TEST

A series of seven thermal tests were conducted on the breadboard model of the dual patch multi-element radiant cooler (Section 2.1). The cooler was subjected to a preconditioning outgassing period prior to each test, as required by the anti-frost design (Sections 1.3 and 2.3.2). The heat loads during the tests simulated operation in the design orbit (9:30 AM sun synchronous at an altitude of 450 n mi; Section 2.3.2). The cooler contained the optical and electrical connections for a 14 element InAs array on the first (warmer) patch and a 4 element HgCdTe array on the second (cooler) patch.

The cone had temperatures in the range from 178K to 181K. This is at the high end of the values calculated in the design study report (Section 3.0). The cone insulation factors used in the design study (80 to 100) were shown to be unrealistically high (see Sections 2.2.1 and 2.4.1). The first patch had temperatures well below 120K in all tests (except when excessive joule heat was applied to determine conductive coupling). On the other hand, the second patch never reached a temperature of 90K. The closest was 92.5K during test 7 and this was with no joule heat. Adding a nominal 2 m w of heat would increase the temperature to about 95K.

The higher patch 2 temperature was the result of two factors. First was the insulation factor discussed above, and second was the non-black space target (Section 2.3). Because it is in a position to view one end of the insulation blanket, the situation was even worse for patch 2. Experimentally, the insulation factor was only about 43. This problem was solved by shielding most of the rear area of the second patch with a low-emissivity shield attached to the first patch. The non-black target produced a thermal load on the second patch estimated to be 3.8 mw. Without this input, but with 2 mw of bias heat, patch 2 would have reached a temperature of about 90.3K.

However, the thermal tests on the cooler may have been quite realistic when the effect of a diffuse component of cone wall reflection is considered (Section 2.2.4). Such a diffuse component could result in an indirect (in-orbit) coupling between the patch and external sources that produces an input almost as large as that from the non-black space target. In order to resolve this problem and increase the confidence in our thermal tests, we need to determine the magnitude of diffuse reflectivity at the cone wall for both infrared and solar radiation.

In addition to the radiant cooler tests, we conducted experimental programs to determine the thermal properties of multilayer insulation and low-emissivity surfaces as they apply to radiant coolers (Sections 2.4, 2.5, and 2.6). The tests showed that simple radiative decoupling can provide an insulation factor equal to or higher than that of the multilayer insulation (again, within the constraints imposed by a radiant cooler or similar structure). The tests also confirmed some results from the cooler test. First, they showed that an effective cone wall emissivity in the vicinity of 0.04 can be obtained. And secondly, they demonstrated that a very high absorptivity (> 0.99) cold target is needed for the accurate determination of radiative properties.

2.1 Radiant Cooler Thermal Tests

Because of fabrication problems with the optically finished earth shield, thermal tests were begun with an aluminized mylar covered shield. The cone walls were optically finished and covered with vacuum deposited aluminum. The results of the first test are listed in Table 2-1.

Table 2-1
Thermal Test 1

	Housing	Shield	Cone	Patch 1	Patch 2
		Final Equilibrium Temperatures			
A.	22.2°C	15.0°C	177.2K	112.3K	131.3K
B.	22.3°C	15.0°C	178.5K	112.9K	101.1K
		Heater Power (mW)			
A.	0	0	2.19	0	49.1
B.	0	0	59.3	0	1.68

As you can see, the heater powers to the cone and patch 2 were reversed during Test 1A. This was traced to a mixup in the lead wires to the terminal board located on the outside of the cooler housing. Unfortunately, thest leads were also reversed during the outgassing that preceded the operation of the cryogenic targets (See Section 2.3). As a result, there was approximately 4W rather than 1W applied to patch 2 during the 20-hour outgassing period. Inspection of the radiant cooler after the completion of test 1 showed that a diffuse coating had been evaporated on portions of all three cone walls.

Identical platinum sensor/bridge combinations were used to measure the temperatures on patches 1 and 2. Although the sensors are not calibrated above 173K, it should have been immediately evident that patch 2 was much hotter than patch 1. However, one of the leads to the sensor on patch 1 had broken. This had the effect of increasing the apparent resistance of the patch 1 sensor and therefore also its apparent temperature. As a result, the patch 1 bridge output seemed to show that it was at a higher temperature than patch 2 at all times. The true situation was discovered when what was thought to be the cone power was increased by about 1/4 watt during test 1 and produced a rapid increase in the temperature of patch 2. The patch 1 temperatures shown in Table 2-1 were determined from electronic Wheatstone bridge measurements of the sensor and lead wire resistances.

Following the completion of test 1, we cleaned the cone walls with a Freon spray. This restored the walls to their original (visual) appearance. The heater lead wires were corrected and the broken wire to patch 1 repaired. The thermal test was then repeated, including the initial 20 hour outgassing period. The results are given in Table 2-2.

Table 2-2
Thermal Test 2

	Housing	Shield	Cone	Patch 1	Patch 2
			Final Equilibrium Temperatures		
A.	24.3°C	20.0°C	180.9K	110.6K	101.1K
B.	24.3°C	20.0°C	181.2K	141.3K	104.9K
			Heater Power (mW)		
A.	0	0	57.5	0	2.88
B.	0	0	57.5	78.0	2.89

The effect of cleaning the cone walls can be seen in the improved thermal performance. Patch 1 cooled an additional 1.7K with a cone temperature 3.7K higher. And patch 2 remained at the same temperature with the higher cone temperature and an additional joule heat of 1.2 mW.

However, the temperature of patch 2 was still about 5K higher than we would like. Before terminating the test, we applied about 85 mW to patch 1 to test the thermal isolation between the patches (test 2B). The temperature of patch 1 increased by 30.7K but that of patch 2 by only 3.8K (see Section 2.2.2).

Next, we disassembled the cooler and inspected the patch compartment. A diffuse coating had been deposited on both the germanium (patch) window and Irtran 2 (cone) window in the optical opening to patch 2. Again this would seem to have resulted from the excessive power applied to patch 2 during the outgassing before test 1. As a result, we also suspected that the multilayer insulation below the patches had been contaminated. The patch insulation blanket was therefore replaced before starting test 3. It was also noted that gold had been evaporated on the outside of the plastic cold trap (cone) attached to patch 2. The cone penetrates into the insulation blanket and was wedged against one side of the insulation (optical) opening. It therefore may have reduced the insulation factor between the cone structure and the back of the patch. The plastic cone was removed before starting test 3. In addition, the tops of both patches were repainted with 3M black velvet.

The final equilibrium temperatures of test 3 are listed in Table 2-3 and the cooling curves for the cone and patch 1 shown in Figure. 2-1. Following the outgassing phase, the baseplate to which the cooler housing was mounted was set at 30°C, the cone power level set to the in-orbit value, and all patch power turned off. The cooler temperatures were then allowed to stabilize before the cold targets were turned on (time zero in Figure 2-1).

Table 2-3
Thermal Test 3

	Housing	Shield	Cone	Patch 1	Patch 2
	Final Equilibrium Temperatures				
A.	23.3°C	18.1°C	181.1K	111.1K	107.3K
B.	23.0	17.9	180.95	109.8	104.85
C.	23.0	17.8	181.3	141.2	108.8
	Heater Power (mW)				
A.	0	0	58.1	0	0
B.	0	0	58.1	0	0
C.	0	0	58.1	79.5	0

Although we cleaned the optical ports and replaced the patch insulation blanket for test 3, the temperature of patch 2 increased above its value in test 2. This seemed to demonstrate the sensitivity of the second patch to the mounting of the insulation blanket. In order to cover the gap in insulation below patch 2 and adjacent to the rear of the cone end radiator, we attached an aluminum shield covered with gold tape to the cone end. This shield extended between the top of the insulation blanket and the bottom of patch 2 and included an opening for the optical beam.

We then ran thermal test 4. There was a sharp break in the cooling curve for patch 2 at about 165K. After that, patch 1 cooled to below patch 2, and the test was terminated. Final (but not equilibrium) temperatures are given in Table 2-4. The results indicate that a significant thermal path between the shield (at cone temperature) and patch 2 was created at a patch temperature of about 165K. This apparently was the result of thermal contractions and small mechanical clearances.

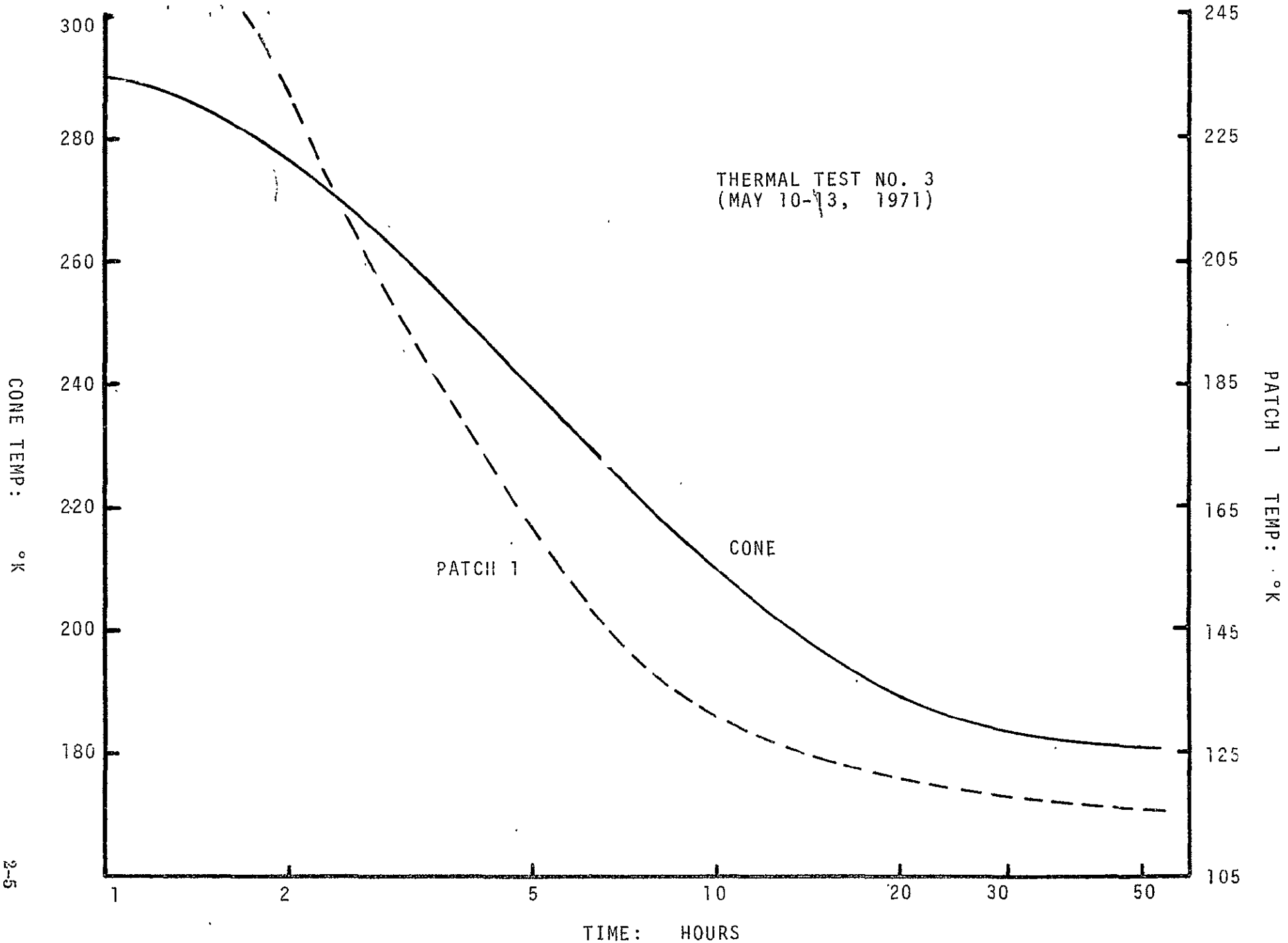

Figure 2-1 Thermal Test No. 3

Table 2-4
Thermal Test 4

Final Temperatures (Heater Powers)				
Housing	Shield	Cone	Patch 1	Patch 2
17.2°C	-11.9°C	182.3K (57.8 mW)	118.8K	123.1K (2.9 mW)

The shield attached to the cone end was then removed. In its place we put a shield attached to patch 1 that extended to the same region between patch 2 and the insulation blanket (again, with an optical opening). The idea here was to divert some of the thermal load from patch 2 to patch 1. Patch 1 had consistently run below its nominal operating temperature of 120K. Most of the rear areas of patch 2 (all except the ends and cutouts needed for the supports) then view a low-emissivity surface at the temperature of patch 1. Gold tape was again used on the shield. In addition, gold tape was attached to regions of patch 1 that had lost their gold coating as a result of the modification.

Thermal test 5 was then run. The temperatures achieved indicated there was an additional thermal path between the cone and patch 1. This was confirmed by inspection following termination at the (non-equilibrium) temperatures listed in Table 2-5. Some of the tape had peeled off and formed thermal patches among the patch, insulation, and cone structure. The tape adhesive had apparently failed at low patch temperatures. Such failure has been observed in the past when temperature sensors were attached to a liquid nitrogen shroud using a similar metallic tape. Moreover, it was found that the gold tape used in tests 4 and 5 had an outer surface of mylar rather than evaporated gold (i.e., it was a mylar-gold-mylar sandwich). This, of course, reduced the effectiveness of the shields.

Table 2-5
Thermal Test 5

Final Temperatures (Heater Powers)				
Housing	Shield	Cone	Patch 1	Patch 2
17.8°C	9.8°C	175.7K (57.8 mW)	129.9K	109.2K (2.9 mW)

All the gold tape was removed. The shield was sprayed with polyurethane, cured, and covered with vacuum deposits of rhodium and gold. In addition, the patches were stripped of their gold surfaces and cleaned. The rear surfaces were then recovered with rhodium and gold and the front surfaces repainted with black paint.

Unfortunately, the temperature sensor and heater leads on patch 2 were cut during the cleaning operation. The remaining tests were therefore conducted without heat on patch 2. The temperature of patch 2 was measured by means of a chromel-constantan differential thermocouple referenced to the platinum sensor on patch 1. Finally, the aluminum cone was replaced with the gold coated one.

However, some screws were left out of the cone supports at the housing when the cooler was re-assembled. As a result, the edge of the cone structure (cone end) rested on the housing during the next test, and the cone did not reach its proper temperature. Nevertheless, the cooler temperatures were allowed to come to equilibrium (Table 2-6) in order to show what patch temperatures could be achieved in the presence of a relatively warm cone.

Table 2-6
Thermal Test 6

Final Equilibrium Temperatures				
Housing	Shield	Cone	Patch 1	Patch 2
25.4°C	6.2°C	~238K	138.6K	109.5K
Heater Power				
0	0	81 mW	0	0

Following the completion of test 6, the cone was properly attached to the cooler housing. At this time, the optically finished earth shields had been completed, so the aluminized-mylar covered shield was replaced with a gold coated shield. We then ran thermal test 7 (Table 2-7). The cooling curves for the cone and patch 2 are shown in Figure 2-2. The difference between tests 6 and 7 and tests 1 through 3 is the much larger temperature difference between the patches. The addition of a nominal 2 mW of bias heat to patch 2 (in test 7) would increase its temperature to about 95K. The increase in patch emission is given by (Section 2.2.3)

$$E_p \sigma A_p \Delta (T_{p2}^4) = \Phi_j - K_{p2} \Delta (T_{p2})$$

where E_p = total patch emissivity = 0.95

A_p = patch black area = 6.4 in^2

T_{p2} = patch 2 temperature

Φ_j = joule heat

K_{p2} = conductive coupling between patches = 1.4×10^{-4} $W \cdot K^{-1}$ (Section 2.2.2)

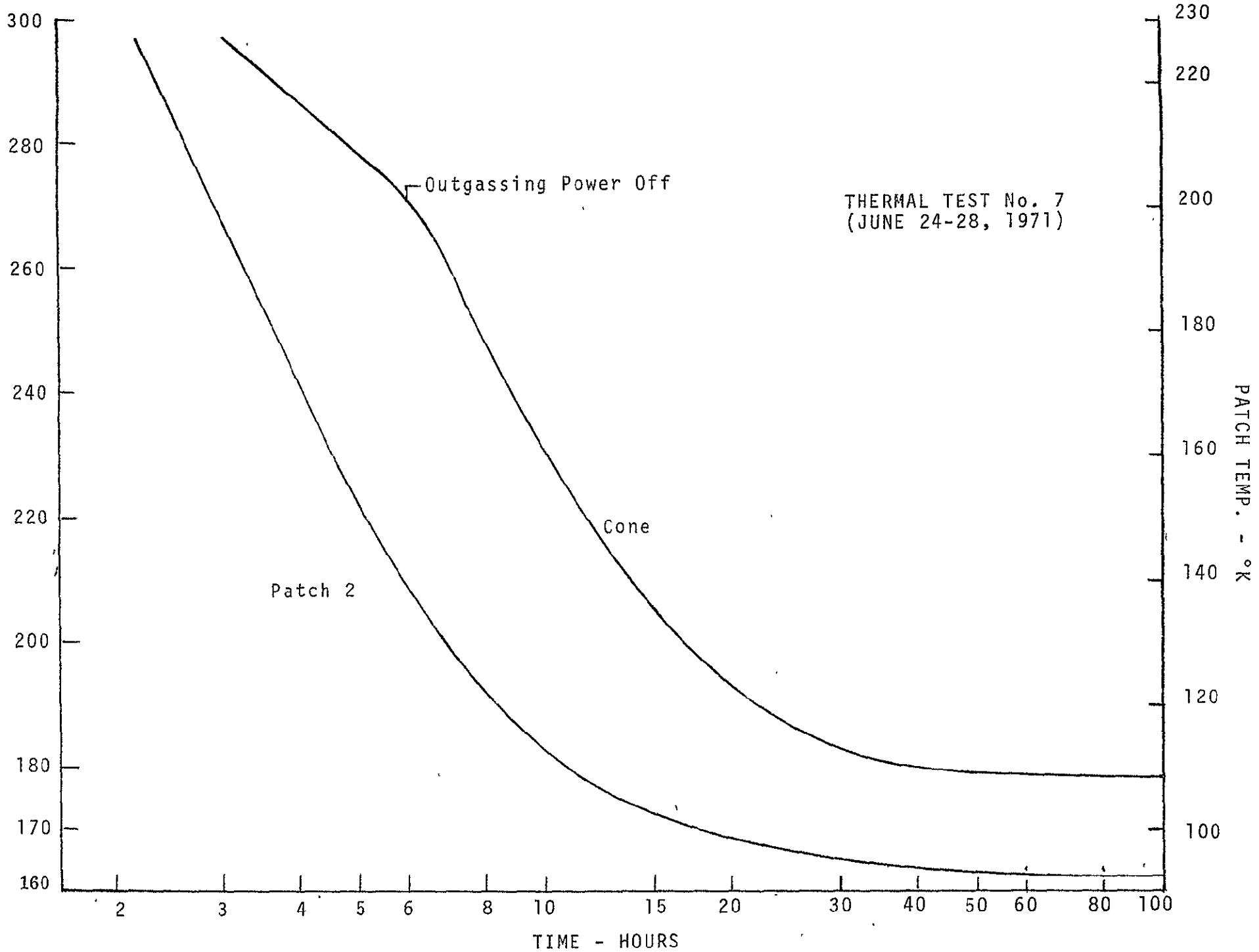

Figure 2-2 Thermal Test No. 7

For an initial patch temperature of 92.5K and a bias heat of 2 mW, the final patch temperature is

$$T_{p2}\ (\text{final}) = 94.8\text{K}$$

Table 2-7
Thermal Test 7

(Begun at 0800, June 24)

Time	Date	H	S	C	P1	P2
1430	June 26	24.3°C	13.8°C	178.7K	112.6K	93.0K
1800	June 27	24.6°	14.0	178.6	112.4	92.5
0735	June 28	24.7°	14.2	178.65	112.5	92.6

H = housing

S = earth shield

C = cone

P1 = patch 1

P2 = patch 2

Cone heater power = 84.2 mW

2.2 Analysis of Cooler Tests

An analysis of the radiant cooler tests showed that the multilayer blankets around the cone and around patch 1 had insulation factors in the range from 60 to 65 (Sections 2.2.1 and 2.2.3). This compares favorably with the best results obtained in separate tests on insulation blankets (Section 2.4.1). However, the factor for patch 2 was only about 43 (Section 2.2.3). This decrease was attributed to the position of the patch relative to the ends of the insulation blanket. The insulation of patch 2 from the cone structure was improved by radiatively shielding most of its back surface with a low-emissivity, close-spaced surface attached to patch 1 (tests 6 and 7).

The experimentally determined conductive couplings to the two patches were 20 to 30 percent higher than the calculated values. The emissivity of the front surface of a patch was in the range from 0.93 to 0.94 (Section 2.2.2).

The effective specular emissivity of the inner cone walls was in the vicinity of 0.04 (Section 2.2.3). The uncertainty in this value is largely the result of the uncertainty in the radiative coupling through the optical opening to each patch.

The accuracy of the thermal tests, especially when used to determine thermal coupling factors, is limited by the effects of a non-black space target (Section 2.3.3). This is particularly true for patch 2 which reached temperatures below 95K in the final test. However, a diffuse component of reflection at the cone wall produces an indirect external load (during in-orbit operation) that may reach the magnitude of the load produced by the non-black target (Section 2.2.4). To improve the accuracy of radiant cooler tests, we need to establish more exactly the magnitude of this diffuse coupling.

2.2.1 Cone Insulation

The results of thermal test 7 will be used to estimate the insulation factor of the blanket between the cone and housing. This can be done using the steady-state thermal balance equation given in Section 3.0 of the design study report (July 1970). The connections between the housing and cone are given in Table 2-8.

Table 2-8

Connections Between Housing and Cone

Quantity	for	Dia. (in.)	Length (in.)	Material
2	Support	1/4 x 3/16	1.51	Synthane
1	Support	1/4 x 3/16	1.66	
2	Support	1/4 x 1/8	3.00	
15	InAs	3×10^{-3}	1.51	Chromel
4	Patch Heat	3×10^{-3}	1.66	
1	Cone Diff. Temp.	3×10^{-3}	1.66	
1	Cone Diff. Temp.	3×10^{-3}	1.66	Constantan
12	Temp. Sensors	2×10^{-3}	1.66	Nickel
2	Cone Heat	2×10^{-3}	1.66	
5	HgCdTe	2×10^{-3}	1.51	

$K_c = 6.73 \times 10^{-4}$ W/K

We will assume a shield emissivity ϵ_h of 0.05 and a cone end emissivity of 0.97 (30 degrees v-grooves with a surface emissivity of 0.92). The cone end area A_d is 25.7 in^2. Using the results of test 7 and the analysis in the design study report we obtain an insulation factor of

$$s_i = 65.3$$

for an insulated area A_i of 158 in^2. Experimental measurements (Sections 2.2.3 and 2.5) indicate that the shield emissivity is less than 0.05, perhaps as low as 0.03. In this case, S_i is reduced to 62.0 in the above calculation. In any case, the insulation factor for the cone is as high as the best results obtained during separate testing of insulation blankets (Section 2.4.1).

2.2.2 Patch Conductive Coupling

The results of thermal tests 2 and 3 can be used to estimate the conductive coupling coefficient between patches. To a first approximation, the increase in power emitted by patch 2 is equal to the increase in power conducted from patch 1.

$$\epsilon_p \sigma A_p \Delta (T_{p2}) = K_{p2} \Delta (T_{p1} - T_{p2})$$

where ϵ_p = emissivity of top of patch 2 = 0.92

A_p = high emissivity area of patch 2 = 6.4 in^2

T_{p2} = temperature of patch 2

T_{p1} = temperature patch 1

K_{p2} = thermal conductance between patches

Using the results from test 2, we obtain

$$K_{p2} = 1.33 \times 10^{-4} \ WK^{-1}$$

This is about 20 percent higher than the calculated value of 1.13×10^{-4} WK^{-1} (Table 2-10). The difference may be a result of the small radiative coupling between the back areas of the patches that was not included in the calculations of cooler performance. If ϵ_p is increased to 0.94, we obtain $K_{p2} = 1.36 \times 10^{-4}$.

The small increase in cone temperature between test 2A and 2B can be used to obtain an estimate of the thermal conductance between the cone and first patch. The increase in cone temperature is the result of a decrease in conductive power transfer to the first patch,

$$\epsilon_d \sigma A_d \Delta (T_c^4) = -K_{p1} \Delta (T_c - T_{p1})$$

where A_d is the cone end area (25.7 in^2), T_c the cone temperature, and ϵ_d the cone end emissivity (0.97). Using the results of test 2, we obtain

$$K_{p1} = 2.1 \times 10^{-4} \text{ W} \cdot \text{K}^{-1}$$

This is about 25 percent higher than the calculated value of 1.7×10^{-4} W · K^{-1} (Table 2-9).

Table 2-9

Connections Between Cone and Patch 1

Quantity	for	Dia. (in.)	Material
15	InAs	3×10^{-3}	Chromel
4	Patch Heat	3×10^{-3}	Chromel
8	Patch Temp.	3×10^{-3}	Chromel
5	Hg.CdTe	2×10^{-3}	Nickel
4	Support	1/8 x 3/32	Synthane

All lengths = 1.6 inches, $K_{p1} = 1.71 \times 10^{-4}$ W/K

Table 2-10

Connections Between Patches

Quantity	for	Dia. (in.)	Material
5	HgCdTe	2×10^{-3}	Nickel
4	Patch Temp.	3×10^{-3}	Chromel
2	Patch Heat	3×10^{-3}	Chromel
2	Support	1/8 x 3/32	Synthane

All lengths = 1.2 inches; $K_{p2} = 1.126 \times 10^{-4}$ W/K

Using the results of test 3 in a similar manner, we obtain

$$K_{p2} = 1.5 \times 10^{-4} \text{ W} \cdot \text{K}^{-1}$$

$$K_{p1} = 2.4 \times 10^{-4} \text{ W} \cdot \text{K}^{-1}$$

As a rough check on the above results, we can use the experimental values for K_{p2} to estimate the front emissivity of patch 2. During the first test, the power to heater circuit of the second patch was decreased by 58.0 mW. However, only part of this heat was dissipated in the patch because of the relatively high lead resistance (Table 2-11). Because the resistivity of the chromel wire used changes very little with temperature, the measurements could be made at ambient. The total resistance was calculated from voltage and current measurements at the input.

Table 2-11

Heater Circuit Parameters

Test	Patch	Leads	Heater	Total Power
1A	2	118 ohms	534 ohms	60.0 mW
1B	2	118	583	2.0
2A	1	101	--	0
2B	1	101	112.3	85.1

The decrease in joule heat to patch 2 during Test 1 was then

$$\Delta \phi_j = 534/652 \times 60.0 - 583/701 \times 2.0 = 47.5 \text{ mW}$$

To a good approximation, this decrease was balanced by decreases in the emitted and conducted powers,

$$\Delta \phi_j = K_{p2} \Delta (T_{p2} - T_{p1}) + \epsilon_{p2} A_p \sigma \Delta (T_{p2}^4)$$

where K_{p2} = thermal conductance between patches = $(1.3 - 1.5) \times 10^{-4}$ W · K^{-1}

T_p = patch temperature

ϵ_p = patch front emissivity

A_p = patch front area = 6.4 in^2

The temperature of patch 2 decreased from 131.3K to 101.1K between tests 1A and 1B. The temperature of patch 1 went from 112.3K to 112.9K during the same period. The calculated patch emissivity is then 0.95 -0.96. Because the rear area of the patch emits through the multilayer insulation between the patch and cone structure, this result should be reduced by the factor

$$1 + Ai_p/S_i A_p$$

where A_{ip} is the rear area and S_i the radiative insulation factor between the rear area and the cone structure. For $A_{ip} = 8.9\ in^2$ and $S_i = 60$, we obtain

$$\epsilon_{p2} \approx 0.93 - 0.94$$

2.2.3 Patch Radiative Coupling

The steady-state thermal balance equation of the first patch may be written in the form (See Section 4.0 of the design study report)

$$\sigma E_p A_p T_{p1}^4 = K_{p1} (T_c - T_{p1}) + \sigma A_p E_{pc} T_c^4 + \Phi_{j1} - K_{p2} (T_{p1} - T_{p2})$$

where E_p = total patch emissivity

E_{pc} = total patch-cone radiative coupling factor

Φ_{j1} = joule heat

E_p includes the total patch emission, i.e., from the front and rear surfaces including the optical opening. Similarly, E_{pc} includes all radiative coupling to the cone structure, i.e., to the cone walls, through the insulation blanket, and through the optical opening. Values of E_{pc} were calculated from the thermal test measurements using

$$K_{p1} = 2.25 \times 10^{-4}\ W \cdot K^{-1}$$

$$K_{p2} = 1.4 \times 10^{-4}\ W \cdot K^{-1}$$

$$E_p = 0.95$$

The results are listed in Table 2-12.

Table 2-12

Total Patch-Cone Radiative Coupling for Patch 1

Test No.	E_{pc}
1A	0.0784
2A	0.0749
3A	0.0741
3B	0.0678
6	0.0849
7	0.0982

Not corrected for non-black space target.

The increased patch-cone radiative coupling produced by the added shield (under patch 2) is readily apparent from the results. The value of E_{pc} from test 3A is close to the average prior to the attachment of the shield. The temperatures from tests 3A and 7 were corrected for the non-black space target (Section 2.3.3), and the values of E_{pc} recalculated (Table 2-13). Because of the weak dependence on conductive coupling and the uncertainty in the absorptivity of the space target, the corrections given in Section 2.3.3 were applied to both patches. Moreover, the corrections used are for a surface emissivity of 0.91, which is close to an experimentally determined value (Section 2.5).

Table 2-13

Corrected Radiative Coupling Factors for Patch 1

Test No.	T_{p1}*	T_{p2}*	T_c	E_{pc}
3A	108.3	104.3	181.1	0.0587
7	109.6	88.0	178.6	0.0822

* Corrected for non-blank space target.

The corrected value of E_{pc} for test 7 is close to the uncorrected value from test 6. The most important correction is to T_{p1}, and this correction is small for the relatively high temperature in test 6. The patch-cone radiative coupling factor may be considered the sum of three smaller factors, ϵ_{pc} to the cone walls, a_o through the optical opening and $A_i/A_d \cdot S_i$ through the insulation blanket. The quantity A_i is the area being insulated and S_i the insulation factor. The coupling through the optical opening is approximately (Appendix B to the design study report)

$$a_o = 1/2\ \epsilon_o\ A_o/A_p$$

where ϵ_o = effective absorptivity of patch window = 0.6

A_o = area of patch window = 0.28 in^2

A_p = area of top of patch (black area) = 6.4 in^2

We then have

$$a_o = 0.013$$

The value of ϵ_{pc} for a cone wall emissivity ϵ_c of 0.05 is 0.0287 (Section 5.0, Table 37, of the design study report). If ϵ_c is 0.04 instead, ϵ_{pc} is reduced to 0.023. Using the corrected values of E_{pc}, we obtain an insulation coupling factor of 0.023 from test 3A and 0.046 from test 7. Since the value of A_i in test 3A was about 1.39 times A_p and about twice as large in test 7, both tests indicate a patch insulation factor of

$$S_i = 60.4$$

As with the other parameters, this is only an estimate. The calculated results are sensitive to the corrections made. However, the result is quite believable. It shows that the cone wall emissivity is below 0.05, a result confirmed by separate measurement and analysis (Sections 2.5 and 2.6), and that the back of patch 1 is as well insulated as the cone (Section 2.2.1) and similar structures (Section 2.4.1). It also confirms that a very high absorptivity space target is needed to determine thermal parameters (See Section 2.6).

In a similar manner, we can determine the cone-patch radiative coupling for patch 2. For the first three tests, the thermal balance equation has the form

$$\sigma E_p A_p T_{p2}^4 = K_{p2} (T_{p1} - T_{p2}) + \sigma A_p E_{pc} T_c^4 + \Phi_{j2}$$

For tests 6 and 7, we should add a term (to the right side) of the form $\sigma A_p E_{pp} T_{p1}^4$ to account for the significant radiative coupling between patches. Or the test results can be integrated as a reduction in E_{pc} using the above equation. This was done to obtain the results listed in Table 2-14.

Table 2-14

Total Patch-Cone Radiative Coupling for Patch 2

Test No.	E_{pc}
1A	0.0851
B	0.0837
2A	0.0807
B	0.0751
3A	0.103
B	0.104
C	0.105
6	0.037
7	0.057

The increase coupling in test 3 is readily apparent. The only difference between this test and tests 1 and 2 was the replacement of the insulation blanket below the patch. Unlike patch 1, portions of the rear area of patch 2 have a good view to one end of the blanket. The reduction produced by adding the shield to patch 1 is even more pronounced.

Test 2A is representative of the results from the first two thermal tests. First we will correct the measured temperatures for the effect of the non-black space target. The results are T_{p1} = 107.7K1 T_{p2} = 97.4 K, and E_{pc} = 0.0625. At this point, it is necessary to correct some results given in the design study report. The values of ϵ_{pc} for area 2 (patch 2) given for design IA (III A) in Table 37 (p. 5-4) are in error. This is a result of the incorrect value of the view factor ($F_{p-m(1)}$) given in Table 36 for the view from the patch to the first-reflection image of the cone mouth. The correct values are shown in Table 2-15.

Table 2-15

Corrected Values of Cone Coupling Factors from Second Patch

$F_{p-m(1)}$	=	0.29648
ϵ_{pc} (0.05)	=	0.02095
ϵ_{pc} (0.07)	=	0.0292

For a cone wall emissivity of 0.04, ϵ_{pc} is approximately 0.017. Using a_o = 0.013, we find that the insulation factor of the blanket behind the second patch is approximately

$$S_i = 427$$

Performance during the first three tests was therefore limited by the relatively poor radiative insulation of the rear surfaces of patch 2. This problem was, of course, solved by adding the low-emissivity shield to patch 1 that covered most of the rear areas of patch 2.

Instead of correcting the patch temperatures, we considered the non-black space target as a source of thermal input. If the surface (black paint) on the target has an emissivity of 0.91, the input equals 3.82 mW. In addition, a term of the form $\sigma A_p E_{pp} T_{p1}^4$ was added to the thermal balance equation. For close-spaced surfaces whose emissivity is 0.03 and for an area ratio A_i/A_p equal to 1.39, E_{pp} is about 0.021. The calculated values of E_{pc} is then 0.030 for test 6 and 0.037 for test 7. Using 0.033 as an average value and subtracting the above values of a_o (0.013) and ϵ_{pc} (0.017), we obtain a residual coupling 0.003. This represents the radiative coupling between the rear surfaces of patch 2 and the cone structure (mostly the end areas) not covered by the shield from patch 1.

2.2.4 The Effects of a Diffuse Component of Cone Wall Reflection

A diffuse component of reflection not only produces an increase in radiative coupling between the cone and patch (Sections 1.2 and 2.6) but also produces a weak direct coupling between external sources and the patch. It is shown below that the magnitude of the indirect external load at the patch may reach the magnitude of the indirect load produced by a non-black space target (Section 2.3.3). The thermal tests on the radiant cooler may therefore be entirely realistic. In any case, the magnitude of the diffuse (or, in general, non-specular) component of cone wall reflection is relatively uncertain, especially for earth-reflected sunlight. In order to increase the confidence in our test results, we need either direct or indirect (i.e., surface properties) measurements on the cone wall materials or on the assembled cone.

The inner cone wall surfaces are finished to 5 wavelengths (visible) of flatness over any 2-inch diameter area (Appendix). A representative flatness for a cone wall is about 10 wavelengths. The corresponding irregularity is then 1 to 2 wavelengths. If we use $20\mu m$ as a representative wavelength λ for infrared radiation from the earth, the irregularity σ_{pp} is related to the rms deviation σ of the surface from its mean limit (i.e., roughness) by (Section 1.2.2)

$$\frac{\sigma_{pp}}{\lambda_{vis}} = 96.65 \frac{\sigma}{\lambda}$$

For the above irregularity, the roughness in terms of the representative wavelength is then

$$\sigma/\lambda = 1.035 \times 10^{-2} \text{ to } 2.07 \times 10^{-2}$$

For blackbody emission, the value of λ may be calculated from

$$\lambda^2 = \frac{\int_0^\infty R(\mu)\, d\mu}{\int_0^\infty \mu^{-2} R(\mu)\, d\mu}$$

where $R(\mu)\, d\mu$ is the fraction of power emitted by a blackbody at a temperature T in the wavelength interval μ to $\mu + d\mu$. The earth has an equivalent (infrared) temperature of about 250K. The above equation then yields a representative wavelength of about $13\ \mu m$.

The fraction of diffuse (normal incidence) reflection at the cone walls for $(4\pi\sigma/\lambda)^2 \ll 1$ is then (Section 2.6)

$$g = (4\pi\sigma/\lambda)^2 = 1.69 \times 10^{-2} \text{ to } 6.77 \times 10^{-2}$$

Also, from the above section, the ratio of effective specular ϵ_c to hemispherical emissivity ϵ_h is given by

$$\frac{\epsilon_c}{\epsilon_h} = 1 - g + \frac{g}{F_{cs}}$$

when the hemispherical emissivity is much less than one. The value $1/F_{cs}$ is about 1.4. We then have

$$\frac{\epsilon_c}{\epsilon_h} = 1 + 0.4\,g = 1.0068 \text{ to } 1.027$$

That is, the effective specular emissivity is less than 3 percent greater than the hemispherical emissivity. This does not include directional effects (Section 1.2.1) or the scattering from dust on the walls.

In order to study external source scattering at the cone wall, consider the analysis given in the design study report (July 1970, Section 3.0). The earth infrared power leaving the cone walls after the first reflection is

$$\Phi_r = A_m F_{me} W_e (1 - \epsilon),$$

where A_m = cone mouth area = 36.55 in^2

F_{me} = view factor from cone mouth to earth = 0.079735

W_e = infrared exitance of earth = 2.1×10^{-2} $w \cdot cm^{-2}$

$(1 - \epsilon)$ = infrared reflectance of a cone wall

For $\epsilon = 0.03$, $\Phi_r = 383.3$ mW. The fraction of Φ_r reaching the patch is approximately $1/2\ g\ F_{cp}$, where F_{cp} is the view factor from the cone to the patch. The factor 1/2 accounts for the fact the upper part of the cone wall receives more earth radiation than the lower part. The value of F_{cp} is 0.1223 for patch 2 and 0.1721 for patch 1. The diffusely reflected components reaching the patch are then

Φ_{d2} = 0.40 to 1.6 mW

Φ_{d1} = 0.56 to 2.2 mW

for patch 2 and patch 1, respectively. By comparison, the non-black space target used in the testing of the radiant cooler produces a patch input in the range from 2.3 to 3.8 mW (Section 2.3). We may therefore conclude that this input more than compensates for the absence of the infrared input produced by diffuse coupling to internal sources.

To illustrate the effect of diffusely reflected (or scattered) sunlight from the earth, we will estimate the fraction g_s of diffuse relatively needed to increase the temperature of patch 2 by 1K at 95K. The power leaving the cone walls after the first reflection is

$$\Phi_s = A_m F_{me} W_r (1 - \alpha)$$

where W_r = reflected sunlight exitance of earth = 1.41×10^{-2} W · cm^{-2} for specified orbit

$1 - \alpha$ = solar reflectance of a cone wall = 0.78 for gold

We then have

$$\Phi_s = 206.8 \text{ mW}$$

and the value of g_s is given by

$$g_s = \frac{4 \times 10^{-2} \times 17.5}{206.8 \times 1/2 \times 0.1223} = 5.5 \times 10^{-2}$$

2.3 Chamber Test Equipment

The chamber simulation of the in-orbit environment is described in Section 7.0 of the design study report (July 1970). The operation of the cold targets and cooler heaters is described in this section.

2.3.1 Cold Targets

Prior to the start of the thermal tests on the radiant cooler, we ran the liquid nitrogen cooled shroud used to radiatively shield the helium (cold space) target (see Section 7.0 of the design study report, July 1970). The platinum temperature sensor on the shroud showed that it was well above liquid nitrogen temperature. Various arrangements for feeding liquid to the shroud were tried, but none improved the temperature reading. However, inspection of the sensor showed that it was not making good thermal contact with the shroud. The contact area was then carefully cleaned and the sensor repotted to the shroud. During subsequent tests, the shroud maintained a temperature of 78.3K $\pm$ 0.1K. The normal boiling point of nitrogen is 77.4K.

Now that we knew the shroud was operating properly, we could test the helium cooled space target. The space target temperature was about 23K $\pm$ 1K with the breadboard radiant cooler in its test position. The temperature was measured with a chromel-constantan differential thermocouple referenced to the platinum sensor on the shroud.

During the initial testing of the shroud, the pressure within the chamber did not go down as expected but remained at about 2×10^{-5} torr. We then leak checked the chamber and found a small opening at the ion gauge itself. When this leak was sealed, the chamber pumped down to about 5×10^{-6} torr without cryopumping. When the shroud and cold space target were operating and the radiant cooler was in its test position, the pressure decreased to less than 3×10^{-7} torr. The ion gauge used to measure the pressure is located at the top of the space chamber.

The thermocouple on the helium target is located on the center plate about one-fourth of the way toward its end. From the design study report (Section 7.0), the thermal resistance between this point and the refrigerator head is about 0.29 $K.W^{-1}$. The opening to the target is 11.5 inches by 10.5 inches. When viewing a blackbody, surrounded at 300K, it then receives a load of about 36 W. Under this condition (i.e., without the cooler in place), the target ran at 27.2K. The second cold exchanger of the helium refrigerator then has a temperature Te given by

$$Te + 0.29 \times 36 \approx 27.2K$$
$$Te \approx 17K$$

The value of Te can also be estimated from the refrigeration curves for the Norelco A-20 (Third Quarterly Report on Contract NAS5-10113, 1 Oct. 1966 - 1 Jan 1967, Appendix II). The result is

$$Te \approx 14.6K \pm 2.9K$$

The second cold exchanger therefore ran near the high-end of its expected range. This appears to be the result of the relatively low helium gas pressure used during the test

2.3.2 Heaters

During the testing of the radiant cooler, heaters are required on the cone and two patches for:

a. Initial outgassing prior to cooler operation (Section 1.3)

b. Simulation of earth load on the cone and bias load on the second (90K) patch.

c. Variation of cone and patch temperatures to study thermal couplings within the cooler.

Heaters that meet the requirements of (a) and (b) will, in general, also meet those of (c).

The cone, patches, and baseplate (instrument housing) will be raised to 55 degrees C during the initial outgassing. At that time, the space target will be at room temperature. The cone end and patches will therefore be radiating to a blackbody at approximately 20 degrees C. The cone heater power required is very nearly

$$\Phi_1 = A_d \sigma (T_c^4 - T_o^4)$$

where A_d = Cone end area = 25.7 in ^{2}

T_c = Cone temperature = 328 K

T_o = space target temperature = 293 K

The result is

$$\Phi_1 = 3.95 \text{ W}$$

Reducing the baseplate temperature to 25 degrees C has little effect on the heater power needed to maintain the cone at 55 degrees C. Specifically, it increases it by less than 0.1 W.

The earth radiation absorbed in the cone walls is given by (Section 3.0 of the design study report and the monthly report for September 1970).

$$\phi_c = A_m (\alpha_{me} W_r + \epsilon_{me} W_e)$$

where A_m = cone mouth area

α_{me} = cone mouth solar absorptivity

ϵ_{me} = cone mouth infrared absorptivity

W_r = reflected sunlight exitance of earth = 1.41×10^{-2} W · cm^{-2}

W_e = infrared exitance of earth = 2.1×10^{-2}W· cm^{-2}

For a cone wall solar absorptivity of 0.22 (gold) and infrared absorptivity of 0.05, we have (Section 5.0 of the design study report).

α_{me} = 1.84×10^{-2}

ϵ_{me} = 4.21×10^{-3}

For a solar absorptivity of 0.13 (aluminum), α_{me} is 1.09×10^{-2}. The cone mouth area is 36.55 in^2, so that the above power becomes

ϕ = 0.0820 W (Au), 0.0571 W (Aℓ)

For a cone wall infrared absorptivity of 0.07, ϕ_e is increased to 0.0903W for gold and 0.0654 W for aluminum.

A 1 inch x 5 inch area heater will be used on the cone. It has a nominal electrical resistance of 1×10^3 ohms. The nominal voltages (V_c) needed for initial outgassing and for in-orbit simulation are given in Table 2-16.

Table 2-16Cone Heater Power and Voltage Requirements

ϕ(Watts)	V_c (Volts)
3.95	62.8
0.0820, 0.0571	9.06, 7.56
0.0903, 0.0654	9.50, 8.09

Nominal heater resistance = 1×10^3 ohms

The maximum nominal cone heater current is about 63 mA. Such a current is easily carried in vacuum by 2×10^{-3} inch diameter nickel wire.

The heater power needed on each patch during the initial outgassing is given by

$$\phi_2 = \sigma A_p (T_p^4 - T_o^4)$$

where A_p = black radiating area of patch = 6.40 in^2

T_p = patch temperature = 328 K

T_o = space target temperature = 293 K

This assumes the cone is also at 328 K (55 degrees C). The result is

$$\phi_2 = 0.984 \text{ W}$$

This bias heat of the detector array on the 90K patch is replaced by dissipation in the patch heater. This requires a thermal load from about 2×10^{-3} to 4×10^{-3} W. Each patch heater is 1×10^3 ohm, 1 W resistor. The voltages required are given in Table 2-17.

Table 2-17 Patch Heater Power and Voltage Requirements

ϕ(Watts)	V_p (Volts)
0.984	31.4
0.002	1.41
0.004	2.00

Nominal heater resistance = 1×10^3 ohms.

1.5-volt batteries are used to provide bias heat. For the 1×10^3 ohm resistance, a 1.5-volt potential results in a dissipation of 2.25×10^{-3} W. Two batteries in series with a 470 ohm dropping resistor will give 4.2×10^{-3} W. Heater leads of 3×10^{-3} inch diameter chromel can be used in all cases.

2.3.3 Corrections for the Non-Black Space Target

The non-black space target provides paths not present in outer space by which radiation from the cone can reach the patches in the multi-element radiant cooler. The patch temperatures measured in the space chamber are therefore higher than those achieved in space and should be corrected to a condition of zero space target reflectivity.

The hemispherical emissivity of the 3M black velvet (101-C10) used on the space target is in the range 0.91 to 0.93. This is shown by heat transfer and emittance measurements (First Quarterly Report, Section 4.2; D. L. Stierwalt, Appl. Opt. 5, 1914, 1966). Hemmerdinger and Hemback list a hemispherical emissivity for 3M black velvet over zinc chromate primer of 0.92 at 228K on alodined aluminum sheets (Chap. 20 in Handbook of MIL. Infrared Techn., ed. by W. L. Wolfe, Off. of Naval Res. 1965). We will consider emissivities of 0.91, 0.93, and 0.95. It should be noted that the 401 series of black velvet has a hemispherical emissivity of 0.89 (Reflective Products Div., 3M Co., Product Bulletin #26-4, Dec. 1, 1968; AFFDL-TR-67-62, Part I, Thermal Test of a Model Space Vehicle, O.W. Clausen and T. Ishimoto, June 1967, Appendix II).

The analysis below shows that the increases in patch 2 temperature corresponding to surface emissivities of 0.91 to 0.95 are 2.5 to 4.2K for the patch at 95K and 2.0 to 3.3K for the patch at 105K.

The surface of the cold target is covered with an array of hexagonal cavities (honeycomb). Each cavity may be approximated by a cylinder whose diameter is equal to its length. This ratio of diameter to length produces a limiting value of cavity hemispherical emissivity for a diffusely reflecting wall of 0.9 or higher emissivity (E. M. Sparrow and R. E. Cess, Radiation Heat Transfer, Brooks/Cole, 1966, pp 164-165). The emissivity of a cavity may be obtained from a linear interpolation of Figure 6-2 of Sparrow and Cess or from the Limiting value formula of Treuenfels (J. Opt. Soc. Am. 53, 1162, 163),

$$\epsilon_c = \frac{\epsilon}{\epsilon + 0.238\,(1-\epsilon)}$$

where ϵ is the wall hemispherical emissivity. The results are listed in Table 2-18 for wall (black velvet) emissivities of 0.91, 0.93 and 0.95.

Table 2-18

Hemispherical Emissivity
of Honeycomb Cavity

ϵ	Sparrow	Treuenfels
0.91	0.9770	0.9775
0.93	0.9824	0.9825
0.95	0.9876	0.9875

Each cavity of the honeycomb target has a flat wall area associated with it. The ratio of wall-end area to total surface area is (A. R. Karoli, H. R. Hickey and R. E. Nelson, Appl. Opt. 6, 1183, 1967)

$$\frac{4\,A_w}{A_t} = \frac{4\,A_w}{4\,A_w + A_c},$$

where

$$A_w = t\left(d - \frac{t}{3}\right)$$

$$A_c = 2.25\left(d - \frac{2t}{\sqrt{3}}\right)$$

d = semi-diagonal of hexagon = 0.0625 inch

t = wall thickness = 0.0025 inch

We then have

$$\frac{4 A_w}{A_t} = 0.0455$$

The surface emissivity of the space target is then

$$\epsilon s = \epsilon \frac{4 A_w}{A_t} + \epsilon_c \left(1 - \frac{4 A_w}{A_t}\right)$$

The corresponding values of surface reflectivity, $\rho_s = 1 - \epsilon_{s\,1}$, are given in Table 2-19.

Table 2-19

Space Target
Surface Reflectivity

ϵ	ρ_s	ρ_o
0.91	0.0238	0.0221
0.93	0.0199	0.0185
0.95	0.0142	0.0132

The space target itself is in the form of a shallow cavity (Design Study Report, Fig. 13). For a high emissivity surface, the shallow cavity emissivity at the opening seen by the radiant cooler is approximately

$$\epsilon_o = 1 - (1 - \epsilon_s) F_{so},$$

where

F_{so} = view factor from surface of target to opening = A_o/A_s

A_o = area of opening = 148.5 in^2

A_s = area of surface = 159.7 in^2

The reflectivity of the space target as seen from the radiant cooler is then

$$\rho_o = 1 - \epsilon_o = 0.93\ \rho_s.$$

Values of ρ_o are given in Table 2-18.

If we assume that the cone end emission is uniformly incident on and diffusely reflected from the space target, the cone end power absorbed in a patch is

$$\Delta\Phi = \epsilon_p \sigma A_d \epsilon_d \rho_o F_{op},$$

where

ϵ_p = patch absorptivity = 0.94

ϵ_d = cone end emissivity = 0.97 (30° v-grooves)

A_d = cone end area = 25.70 in^2

F_{op} = view factor from cone mouth (space target as seen from patch) to patch.

Because the cone walls are highly reflective, the view factor from the patch to the space target (cone mouth) is effectively unity. By reciprocity, the view factor from the cone mouth to the patch is then

$$F_{op} = \frac{A_p}{Am} = 0.192,$$

where A_m is the cone mouth area.

The thermal input to the patch produced by the non-black space target is balanced by an increase in patch emission and a reduction in the conduction to patch 1,

$$\Delta\Phi = \Delta(\epsilon_p \sigma A_p T_p^4{}^2) = K_p 2 \cdot \Delta T_p 2,$$

where $K_p 2$ is the thermal conductance between patches (1.33×10^{-4} $W \cdot K^{-1}$, monthly report for April 1971, Section 2.2). For a small temperature increase $\Delta T_p 2$, we then have

$$\frac{\Delta T_p 2}{T_p 2} = \frac{\Delta\Phi}{4\epsilon_p \sigma A_p T_p^4 + K_{p2} T_{p2}}$$

The relative temperature increases are given in Table 2-20 for patch temperatures from 90 to 120K and a cone temperature of 180K. The corresponding temperature increases for the three values of black velvet emissivity are also listed in Table 2-20. A reduction in cone temperature to 175K would reduce ΔT_{p2} by about 11 percent.

Table 2-20

Patch 2 Temperature Increase
Produced by a Non-Black Space Target

T_{p2} (K)	$\Delta T_{p2}/T_{p2}$	ΔT_{p2} for ϵ Equal to 0.91	0.93	0.95
90	2.44 ρ_o	4.8K	4.1K	2.9K
95	2.01 ρ_o	4.2	3.5	2.5
100	1.67 ρ_o	3.7	3.1	2.2
105	1.40 ρ_o	3.3	2.7	2.0
110	1.18 ρ_o	2.9	2.4	1.7
120	0.850 ρ_o	2.2	1.9	1.3

All for T_c = 180K

2.4 Radiative Insulation Tests

Tests were run to determine the thermal properties of radiative insulation used to thermally shield the rear surfaces of the cone and patches within a radiant cooler. Measurements were made on blankets of multilayer insulation (Section 2.4.1) and on close-spaced, low-emissivity surfaces (Section 2.4.2).

2.4.1 Multilayer Insulation Tests

The insulation value of the multilayer may be expressed as a shielding factor s_i or an equivalent thermal conductivity k_i. The shielding factor is the reciprocal of the effective emissivity or radiative coupling coefficient. The two parameters are related by

$$(1/s_i)\ (T_h^4 - T_c^4) = (k_i/t_i)\ (T_h - T_c)$$

where T_h = Temperature of warm boundary

T_c = Temperature of cool boundary

t_i = Thickness of layer

The multilayer experiments were directed toward obtaining techniques and parameters applicable to insulation of the space between the housing and outer cone walls.

The thermal balance equation of the high-emissivity radiating plate in the first insulation test fixture (Figure 2-3) is

$$\epsilon_p\ \sigma A_p\ (T_p^4 - T_o^4) = K_c\ (T_b - T_p) + (\sigma A_p/s_i) \cdot (T_b^4 - T_p^4)$$

where ϵ_p = effective emissivity between plate and liquid nitrogen target

A_p = top radiating area of plate

T_p = temperature of plate

T_o = temperature of liquid nitrogen target

T_b = base temperature

K_c = thermal conductance between plate and base

s_i = shielding factor of multilayer insulation

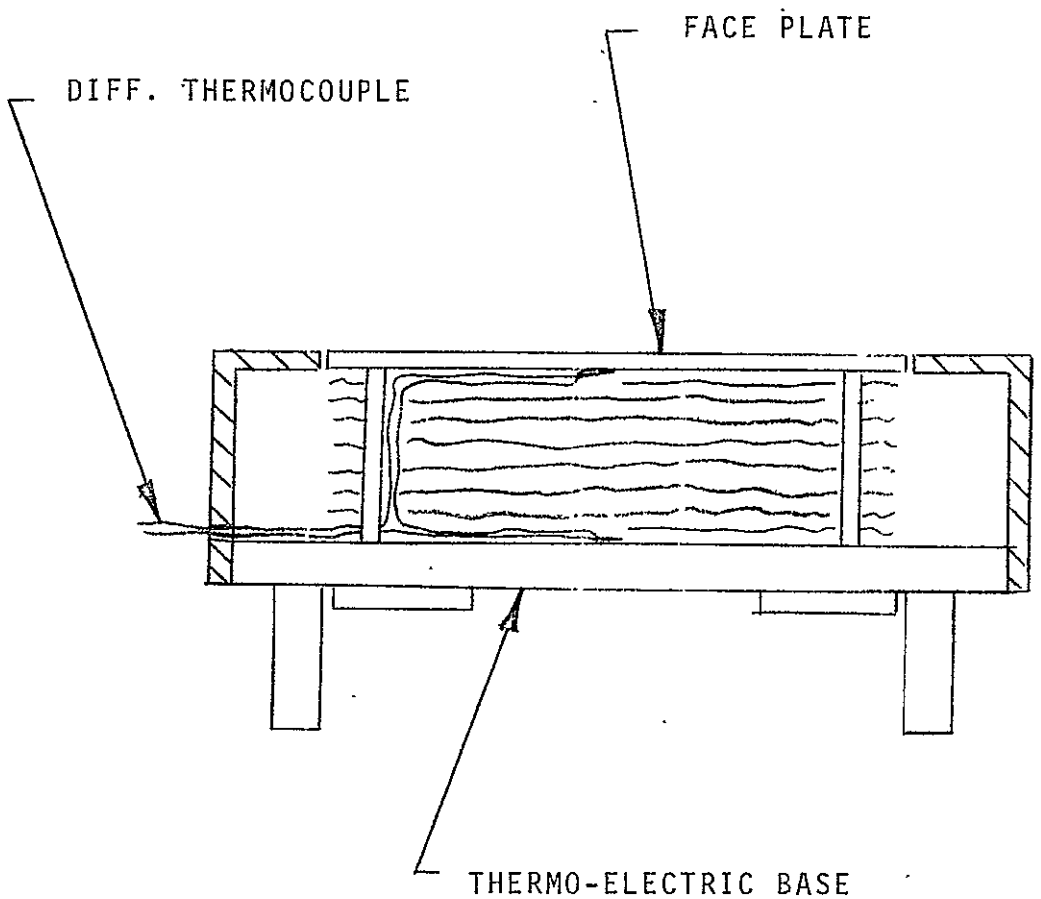

Figure 2-3 Multilayer Insulation Test Apparatus

The plate is supported from the base by two fiberglass-reinforced epoxy tubes of 1/4 inch OD, 1/8 inch ID, and 1 inch length. The thermal conductivity of the material is about 3.5×10^{-3} W/cm^{o}C. Including the effect of the nylon screws used for mounting, the supports have a thermal conductance of about 6.94×10^{-4} W/K. The thermocouple leads between the plate and base consist of one chromel wire and one constantan wire, each of 5×10^{-3} inch diameter and 1 inch length. These have thermal conductivities of 0.13 and 0.23 W/cm^{o}C, respectively, and contribute a total conductance of 0.18×10^{-4} W/K. The value of K_c is therefore approximately 7.12×10^{-4} W/K.

For $\epsilon_p = 0.84$ (Section 2.5.1) and $A_p = 40$ in^2, the thermal balance equation then yields

$$1/s_i = 0.84\,(T_p^{\,4} - T_o^{\,4}/T_b^{\,2} - T_p^{\,4}) - 4.867 \times 10^5\,(T_b - T_p/T_b^{\,4} - T_p^{\,4})$$

An initial series of three tests were run. In the first two, a 1 inch blanket of multilayer was simply stacked below the plate, as shown in Figure 2-3 . The blanket consisted of alternate layers of smooth and dimpled aluminized mylar sheets. The open ends of the blanket viewed a machined, but unanodized, aluminum surface. For the first test, there were 17 smooth and 16 dimpled sheets. The final (equilibrium temperatures were

$$T_o = 94K$$

$$T_p = 151K$$

$$T_b = 298K \text{ (regulated)}$$

and the resultant shielding factor

$$s_i = 25$$

For the second test, the number of insulation sheets was increased by about 50 percent. However, this increased the shielding factor by less than 1 percent.

For the third test, the side walls seen by the open ends of the insulation blanket were covered by a smooth layer of insulation followed by a dimpled layer and a second smooth layer. The final temperatures were

$$T_o = 94K$$

$$T_p = 134K$$

$$T_b = 298K$$

and the resultant shielding factor

$$s_i = 60$$

The nature of the surface seen by the open ends of the insulation blanket therefore has a very large influence on the effectiveness of the multilayer. The ends apparently act as a black receiver whose radiative input is efficiently conducted down the aluminum film on the insulation sheets. Because of the importance of the open ends, the test fixture was modified to more accuately represent an actual cooler cone. The ratio of blanket end area to insulated cone wall area is about 0.65 in the initial insulation test fixture. On the other hand, the ratio in a typical cooler is only 0.25. The insulated area was therefore increased by attaching a box to the underside of the plate. (Figure 2-4). This modification has the additional advantage of reducing the influence of thermal conductance through the support tubes and thermocouple wires.

A series of tests were run with the modified multilayer insulation test fixture. The thermal balance equation of the high-emissivity plate in the new arrangement (Figure 2-4) is

$$\epsilon_p \sigma A_p (T_p^4 - T_o^4) = K_C (T_b - T_p) + (\sigma A_i/s_i) \cdot (T_b^4 - T_p^4)$$

where ϵ_p = effective emissivity between plate and cold space = 0.89

A_p = top radiating area of plate = 40 in^2

T_p = temperature of plate

T_o = temperature of cold space target

T_b = base temperature

K_c = thermal conductance between plate and base = 3.34×10^{-4} W/K

A_i = insulated area at T_p = 103 in^2

s_i = shielding factor of multilayer insulation

The flat plate faced a honeycomb cold target in this set of experiments. The emissivity of the paint (and therefore also of the plate) is about 0.91 (Section 2.5.1). The length to diameter ratio of the honeycomb cavities is sufficiently large that the limiting value of hemispherical emissivity is attained (See E.M. Sparrow and R.D. Cess, Radiative Heat Transfer, Brooks/Cole 1966, p. 165). The emissivity of a cavity may be estimated from the results of Sparrow or calculated from the formula of Treuenfels (Jour. Opt. Soc. Am. 53, 1162, 1963). The result of 0.977 for a paint emissivity of 0.91. About 8.2 percent of the space target is flat and remainder cavities. Its average emissivity is therefore 0.972, and the effective emissivity between the plate and target is about 0.89.

The plate is supported from the base by two synthane tubes of 1/4 inch OD, 1/8 inch ID, and 1.89 inch length. The thermal conductivity of the material is about 3.3×10^{-3} W/cm · K and the thermal conductance of the supports, 3.265×10^{-4} W/K. The remainder of the conductance is produced by the thermocouple leads to the plate.

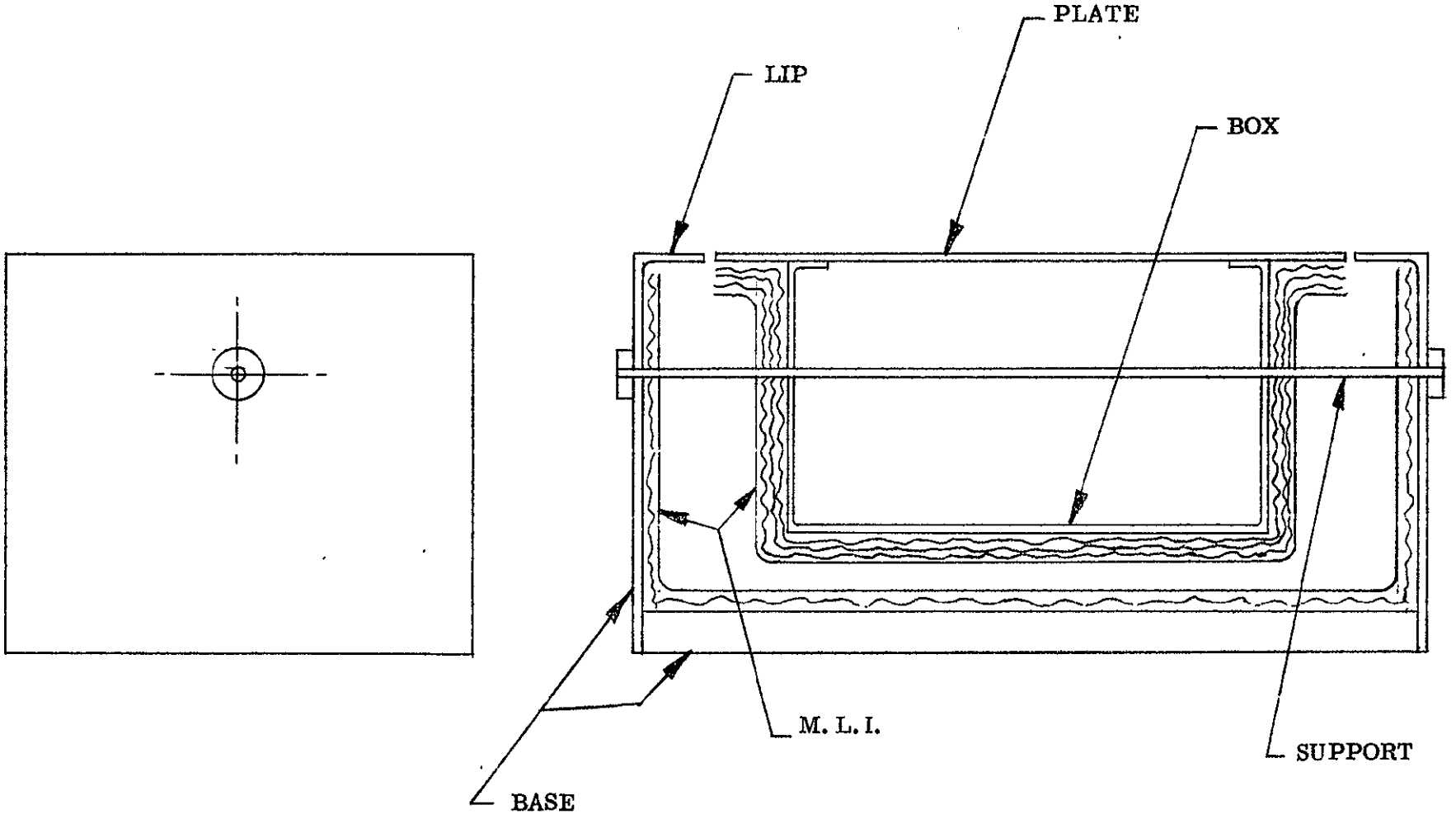

Figure 2-4. Multilayer Insulation Test Fixture Modification 1

The tests run are listed in Table 2-21. For the first test, smooth sheets of aluminized mylar were attached to the inside of the base and the outside of the box, including the adjacent inside plate area. The results are given in Table 2-21. The theoretical improvement for perfect radiation shields, when the number of shields is increased fro n_1 to n_2, is $n_2 + 1/n_1 + 1$. This ratio and the actual improvement are also shown in Table 2-22.

Table 2-21 Multilayer Insulation Tests in Modified Fixture

Test No.	Pairs* of Insulation on Base	Pairs* of Insulation on Box
1	0	0
2	0	2
3	0	4
4	2	4

* One pair is a smooth and a dimpled layer of mylar aluminized on both sides.

Table 2-22 Results of Insulation Tests

Test No.	T_o	T_p	T_b	s_i	Improvement Actual	Improvement Ideal
1	27.8	164.4	298.7	30.1	-	-
2	28.0	148.0	293.4	45.4	1.51	3
3	28.0	144.0	294.4	52.5	1.16	1.67
4	40.9	139.7	291.0	58.0	1.10	1.40

Following the fourth test, an additional 7 pairs were added to the base. This increased s_i by 1.18X (to 68.4) compared with an ideal of 2X. However, the open ends of the blanket on the base were pushed up against the lip (Figure 2-4) because of the increased bulk. In the actual cooler, this situation was remedied by backing the insulation blanket away from the surface (lip) and covering the surface with a low-emissivity coating (gold on rhodium on polyurethane spray).

2.4.2 Radiative Decoupling

The stack of multilayer insulation below the patch of the cone wall test equipment (Section 2.5.1) was replaced by a close-spaced geometry of gold plated aluminum surfaces (rear of patch and facing surface of base). The two patch supports were provided with coaxial low-emissivity shields of gold tape.

The modified equipment was used to determine the effective emissivity of the gold surfaces and therefore the insulation factor of the close-spaced geometry. Based on a set of three experiments, the gold surfaces have an emissivity of 0.042. The corresponding shielding factor is 47.3 between the rear of the patch and the adjacent base (cone structure). The emissivity compares favorably with a previously measured value of 0.048 for a gold plated aluminum surface (Final Report, Part II, on Contract NAS5-11683, 8 April - 15 December, 1969). We may therefore conclude that the close-spaced geometry behaves as expected. The arrangement provides an insulation factor of $2/\epsilon$, where ϵ is the hemispherical emissivity of either surface. Surfaces prepared according to the procedure used on the larger cooler cone for the ITOS radiometer have a hemispherical emissivity of approximately 0.02 (ibid). If such surfaces were used on the facing areas of a close-spaced geometry, they would provide an insulation factor of about 100.

The effects of departures from close-spaced geometry can be estimated from Christiansen's formula (M. Jakob, Heat Transfer, Vol. II, John Wiley & Sons, 1957, p. 5),

$$\frac{1}{\epsilon} = \frac{1}{\epsilon_1} + \left(\frac{1}{\epsilon_2} - 1\right)\frac{A_1}{A_2}$$

where

ϵ = radiative interchange factor or effective emissivity

ϵ_i = emissivity of surface i

A_i = area of surface i

The subscript 1 refers to the inner surface and 2 to the outer. The equation is exact for diffusely reflecting concentric spheres and infinitely long coaxial cylinders. In general, the distance between the two surfaces should not vary much over all the surface. For infinite plane-parallel plates or close-spaced geometry, $A_i/A_2 \rightarrow 1$. We then have

$$\frac{1}{\epsilon} = \frac{1}{\epsilon_1} + \frac{1}{\epsilon_2} - 1$$

This result also holds for specularly reflecting parallel plates, long coaxial cylinders, and concentric spheres. The distinction between diffuse and specular reflection is therefore eliminated for closely spaced surfaces. In terms of shielding factors, the above formula becomes

$$s = s_1 + s_2 - 1$$

If either surface is black (emissivity of one), the overall shielding factor is equal to that of the non-black surface.

2.4.2.1 Test Results

The thermal balance equation of the patch in the test fixture is

$$\sigma\epsilon_p A_p (T_p^4 - T_o^4) = \frac{\sigma A_i}{2} \epsilon_g (T_b^4 - T_p^4)$$
$$+K_p(T_b - T_p) + \Phi_h + \Phi_s$$

where

ϵ_p	=	effective emissivity for interchange between front of patch and cold target
ϵ_g	=	emissivity of gold plated surfaces on rear of patch and base
A_p	=	front (black) area of patch
A_i	=	side and bottom (gold) area of patch
T_p	=	patch temperature
T_o	=	cold target temperature
T_b	=	base temperature
Φ_s	=	radiative input from support shields
Φ_h	=	joule heat on patch

An approximate formula for Φ_s is derived in Section 2.4.2.2 in terms of the shield emissivity ϵ_s, the support outer area A_s, and the temperature T_b and T_p. Because of the approximate nature of the formula for ϵ_s, we will assume that ϵ_s equals ϵ_g and therefore obtain an average emissivity for all gold surfaces. In addition, we will use a value of ϵ_p (0.89) based on a previous determination of the black paint emissivity (Section 2.5.1). A variation of $\pm$ 0.03 in ϵ_p results in a variation of about $\pm$ 6 percent in ϵ_g, comparable with the variation in the experimental results.

The thermal conductance K_p is equal to 0.0407 mW/K. The conductive paths are those through the two synthane supports (1/8 inch OD and 3/32 inch ID), two chromel heater leads (3×10^{-3} inch diameter), and two chromel-constantan thermocouple leads (3×10^{-3} inch). The length of all paths is 2.5 inches.

The test measurements are listed in Table 2-23. Each temperature is the average of from four to six readings taken after thermal equilibrium had been reached.

Table 2-23
Test Measurements

Test No.	T_b	T_p	T_o	Φ_h
1	300.4	149.7	85.6	25.286
2	301.0	158.3	86.8	52.692
3	301.1	141.5	87.0	0

Temperature in kelvins; power in milliwatts.

For the set-up used,

$$A_p = 5.944 \text{ in}^2$$
$$A_i = 6.822 \text{ in}^2$$
$$2A_s = 1.963 \text{ in}^2$$

The calculated values of gold surface emissivity (ϵg) are listed in Table 2-24 for an effective patch emissivity (ϵp) of 0.89.

Table 2-24
Emissivity of Gold Surfaces

Test No.	ϵ_g
1	0.0422
2	0.0401
3	0.0445
Average	0.0423

2.4.2.2 Radiative Input to Supports

The geometry of a patch support and its coaxial shield is shown in Figure 2-5. We will assume a linear temperature distribution between the base and patch. In addition, we will assume that all the net radiative input to the outer surface of the support is conducted into the patch. An area element on the outer surface of the support at a distance x from its connection to the base, absorbs a net radiant power given by

$$d\Phi x = \pi D \epsilon_s \sigma (T_b^4 - T_x^4)\, dx$$

where D is the other diameter of the support, ϵ_s the emissivity of the shield, and Tx the temperature at X. The support is assumed to be black.

For the linear temperature drop, we have

$$Tx = T_b - (T_b - T_p) \frac{x}{\ell}$$

where ℓ is the length of the support between the base and patch. Inserting this into the expression for $d\Phi x$ and integrating from 0 to ℓ, we obtain the radiant power absorbed in the outer surface of the support tube.

Simplifying and rearranging, we obtain an expression for the radiative input to the support,

A = SUPPORT

B = GOLD SHIELD

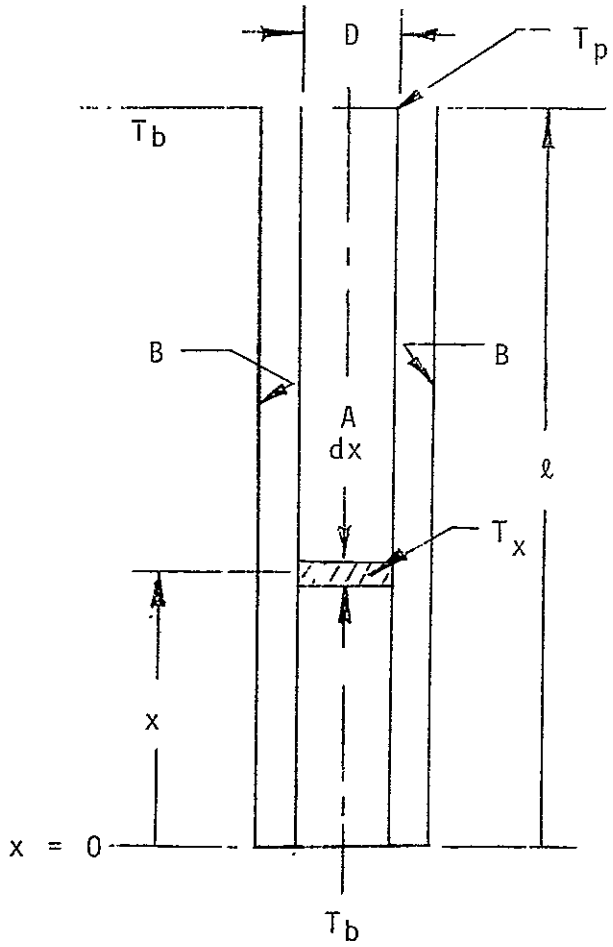

Figure 2-5 Patch Support and Coaxial Shield

$$\Phi_s = \sigma A_s \epsilon_s (T_b^4 - T_p^4) \left[\frac{T_b}{T_b + T_p} - \frac{(T_b - T_p)^4}{5 (T_b^4 - T_p^4)} \right]$$

where A_s is the outer support area, $\pi D \ell$. At the temperatures measured, the expression within the square brackets has a value of 0.654 ± 0.010 and is therefore very nearly constant.

2.5 Cone Emissivity Measurements

The emissivity of the inner cone walls of a radiant cooler were determined in both a 45 degree test cone (Section 2.5.1) and in a bell jar emissometer (Section 2.5.2). The test cone results are expressed as an effective specular emissivity and the emissometer results as a hemispherical emissivity. An analysis of the cone emissivity measurements is made in Section 2.6. It is shown that the greater than 2:1 ratio of effective to hemispherical emissivity can be largely explained as the result of (a) a directional increase, (b) a non-specular reflection component and (c) a non-black space target.

2.5.1 Effective Cone Wall Emissivity

Previous experimental measurements have shown that techniques and materials used to prepare inner cone wall surfaces result in a low value (<0.02) for the hemispherical emissivity (Final Report on Contract No. NAS5-11683, Part II, 8 April - 15 December 1969). These measurements, however, did not include any indication of deviations from specular reflectivity at the surface. Such deviations increase the apparent specular surface emissivity (ϵ_c), as discussed in Section 1.2.

A cooler cone of simple geometry was therefore designed for the purpose of obtaining a measure of the (effective) cone wall emissivity that includes the influence of deviations from specular reflectivity. Although the values obtained strictly apply only to the exact cone geometry employed in the experiment, they provide a direct and meaningful comparison between various cone wall surfaces. Photographs of one of the test cones are shown in Figures 2-6 and 2-7. Figure 2-6 shows the insulation box and support enclosure mounted below the cone. The polished, hardcoated aluminum inner surfaces are shown in Figure 2-7. The hardcoat is obtained by means of an anodic oxidation process.

A second test cone was constructed of optically polished, electroless nickel plated aluminum. The polished walls were covered with evaporated aluminum. This surface has been advocated as an inner cone wall surface by several workers, including those at A.D. Little, Inc. (F. Gabron, "Design Study of Passive Detector Cooling Techniques", Final Report on Contract NAS5-21009, August 29, 1969). The average surface flatness of the nickel-plated walls was about 17 wavelengths of visible light.

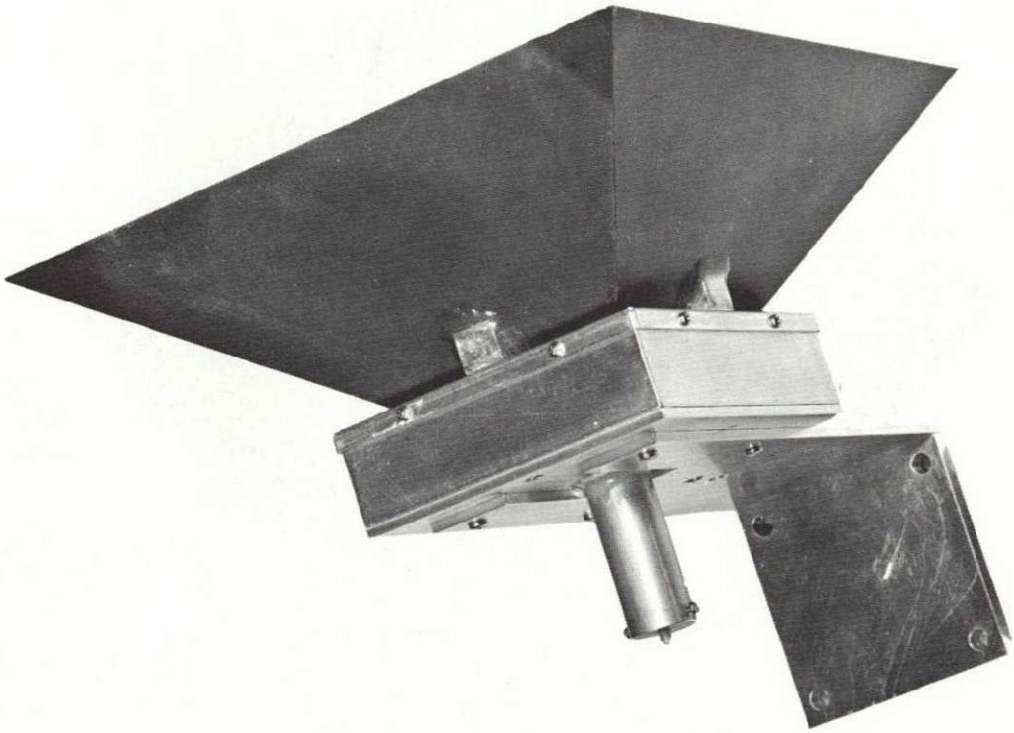

Figure 2-6 Insulation Box and Support Enclosure

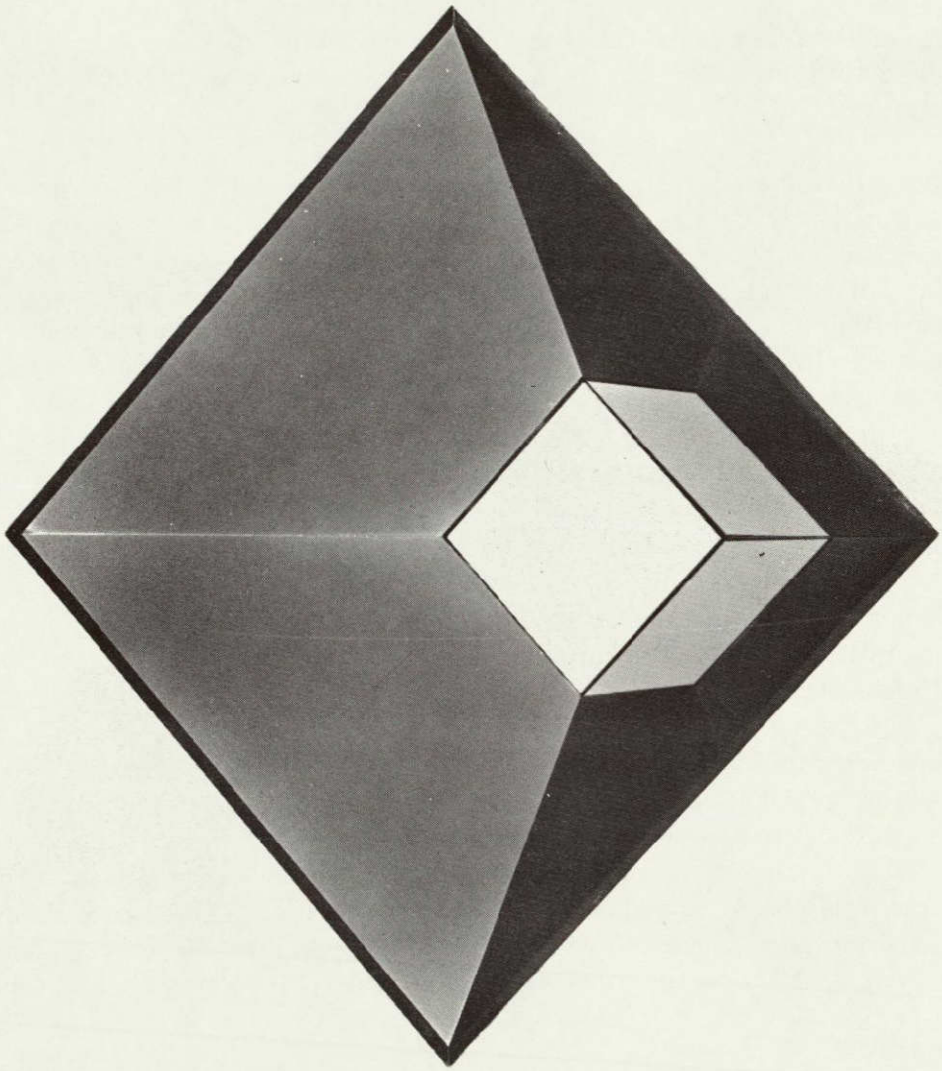

Figure 2-7 Polished, Hard Coated Aluminum Inner Surfaces of Cone

The value of ϵ_c was about 0.048 for both vacuum aluminized hardcoated aluminum and vacuum aluminized electroless nickel-plated aluminum. The results must be considered estimates for at least two reasons:

a. The coupling between the rear of the patch and the cone structure was large in comparison with the coupling between the cone walls and the (black) front of the patch.

b. The space target had a relatively high reflectivity that produced an undesirably large coupling between the walls and patch by way of the target.

In spite of (a), the values determined for ϵ_c were quite consistent among several experiments run, especially for the hardcoated walls. This is a direct result of the apparently high accuracy (at least, repeatability) in the determination of both the coupling to the back of the patch and the effective emissivity for the patch to space target radiative interchange. Because of (b), the results must also be considered upper limits on the value ϵ_c. Repeating the test with a lower reflectivity space target should reduce the value of ϵ_c determined by means of the thermal balance equations.

The space target surface is an array of pyramids (two sets of v-grooves cut at right angles to each other). It may be considered an early (circa 1960) model in the development of satellite-borne radiometer technology. The array has little cavity enhancements. Moreover, the pyramid points are difficult to paint. The target was replaced by a honeycomb cavity array attached directly to the liquid nitrogen reservoir by means of copper-filled epoxy. The improved target was used in the study of radiative transfer between close-spaced surfaces (Section 2.4.2).

The insulation below the patch is a simple stack of multilayer. It was designed for good outgassing properties. However, it has a large ratio of open end area (effectively black sides) to insulated area. This has previously been shown to be a poor arrangement from the standpoint of thermal isolation (Section 2.4.1). We can do better with a simple closed spaced geometry of low-emissivity surfaces between the rear of the patch and the cone structure and low-emissivity shields concentric with the two patch supports. Tests on the close-spaced geometry are described in Section 2.4.2.

2.5.1.1 Test Results

The thermal balance equation of the patch in the test cone fixture is given by (assumes specular cone wall reflection)

$$\sigma\epsilon_p A_p (T_p^4 - T_o^4) = \sigma\epsilon_p^4 A_p \epsilon_{pc} (T_c^4 - T_o^4)$$
$$+ (\sigma A_i/s_i)(T_c^4 - T_p^4) + K_p (T_c - T_p) + \phi_h \qquad (2\text{-}1)$$

where ϵ_p = effective emissivity for radiative exchange between patch and space target

ϵ_{pc} = effective patch-to-cone emissivity

A_p = black radiating area of patch

A_i = rear and side area of patch insulated from the cone structure

T_p = patch temperature

T_o = space target temperature

T_c = cone temperature

s_i = shielding factor of insulation

K_p = thermal conductance of supports and electrical leads

ϕ_h = patch heater power

The effective cone-to-patch emissivity is related to the effective specular cone wall emissivity by

$$\epsilon_{pc} = F_{pc} \cdot \epsilon_c$$

where F_{pc} is the view factor from the patch to the cone walls. The view factor can be calculated exactly by means of view factor algebra. The necessary formulas are given in Appendix VI to the Fourth Quarterly Report on Contract NAS5-10113 (15 April 1967). The result is

$$F_{pm} \quad 0.7173$$

For the set-up used

$$A_p = 5.944 \text{ in}^2$$

$$A_i = 6.822 \text{ in}^2$$

$$K_p = 3.91 \times 10^{-5} \text{ W} \cdot \text{K}^{-1}$$

A value of σ equal to 3.657×10^{-11} W · in^{-2} · K^{-4} was used in the calculations.

The temperature measurements for two tests on each of the cone wall assemblies are given in Table 2-25.

Table 2-25 Test Cone Measurements

Test No.	Cone Substrate	T_o	T_p	T_c	ϕ_h
1	Hardcoated	91.5	183.6	287.8	0
2	Hardcoated	92.3	197.9	288.5	0.08234
3	Nickelplated	91.4	187.4	293.4	0
4	Nickelplated	91.9	202.5	293.7	0.09821

Temperatures in kelvins; heater power in watts.

The temperatures are averages of from 4 to 7 readings taken over a period of several hours after the system had reached thermal equilibrium. The temperature of the test fixture was raised to at least 55 degrees C and pumped for at least 20 hours prior to cooling the space target with liquid nitrogen. Also, the test fixture was reheated to well above the frost point for the ambient chamber pressure prior to heating the space target back to room temperature. The cone structure (cone and box around the rear of the patch) was connected to a temperature controlled baseplate. The temperature was measured with a copper-constantan thermocouple and a Leeds and Northrup temperature potentiometer (Cat. No. 8692). The patch and space target temperatures were measured with differential chromel-constantan thermocouples to the cone. The heater and differential thermocouple voltages were measured on a Doric Model DS-100 integrating microvoltmeter. The heater current was measured on a Weston Model 902 milliammeter (0-15mA scale).

Next, the tests were repeated without a cone in order to determine the values of ϵ_p and s_i (equation 2-1 with $\epsilon_{pc} = 0$). The patch was heated in all cases to stay close to the temperatures encountered during the cone tests. The results of the measurements and calculations are given in Table 2-26 .

Table 2-26 Determination of ϵ_p and S_i

Test No.	T_o	T_p	T_c	ϕ_h	ϵ_p	s_i
5	94.5	208.5	289.0	0.17317		
					0.847	8.085
6	94.35	192.7	289.2	0.06221		
					0.831	8.30
7	94.2	186.1	289.2	0.02422		

The following values were used to calculate ϵ_{pc} from equation 2-1 and the data in Table 2-25.

$$\epsilon_p = 0.84$$

$$s_i = 8.19$$

If we assume both the patch and the space target have the same emissivity ϵ, we obtain

$$\epsilon_p = \epsilon/2-\epsilon$$

For ϵ_p equal to 0.84, ϵ is then 0.91.

The values of ϵ_{pc} and ϵ_c are given in Table 2-27. The value of F_{pc} is 0.2827.

Table 2-27 Cone Wall Emissivities

Test No.	ϵ_{pc}	ϵ_c
1	1.31×10^{-2}	0.0463
2	1.33×10^{-2}	0.0470
3	1.50×10^{-2}	0.053
4	1.25×10^{-2}	0.044

The reproducibility of the tests was considereably greater for the hardcoated sample. The average value of ϵ_c for all four tests is about 0.048.

2.5.1.2 Effect of Non-Zero Space Target Reflectivity

In addition to decreasing the value of ϵ_p, a non-zero value of space target reflectivity provides alternate paths by which cone wall emission can reach the patch. An estimate of the fraction of cone wall emission that reaches the patch by way of the space target is made below. A black patch is assumed and losses in the cone wall are neglected. In addition, specular reflectivity at the cone walls is assumed.

The fraction of diffuse cone wall emission that reaches the space target directly or by one specular cone wall reflection is

$$F_{cs} + F_{cc}(1 - \epsilon_c) = F_{cs} + F_{cc} = 1 - F_{cp}$$

when cone wall losses are neglected ($\epsilon_c \ll 1$). The factor F_{ij} is the view factor from i to j. The letter c refers to the cone walls, s to the space target (cone mouth), and p to the patch. The fraction reaching the patch after one space target reflection is then $(1 - F_{cp})\ \rho_s\ E_{sp}$, where ρ_s is the diffuse reflectivity of the target and E_{sp} the exchange factor from the target (cone mouth) to the patch. The exchange factor E_{ij} is the fraction of diffusely distributed flux from surface i that reaches surface j directly and by all possible intervening specular reflections (E. M. Sparrow and R. D. Cess, Radiation Heat Transfer, Brooks/Cole, 1966, pp. 140-149). The total fraction of cone wall emission that eventually reaches the patch by reflection in the space target is then

$$r = (1-F_{cp})\,\rho_s E_{sp}\,[1 + (1-E_{sp})\,\rho_s + (1-E_{sp})^2 \rho_s^2 + \cdots]$$

$$r = \frac{(1-F_{cp})\,\rho_s E_{sp}}{1 - (1-E_{sp})\,\rho_s}$$

By the reciprocity relation, we have

$$A_s E_{sp} = A_p E_{ps}$$

We also have

$$E_{ps} = F_{ps} + (1 - \epsilon_c)\,F_{pc}$$

$$E_{ps} = F_{ps} + F_{pc} = 1$$

For ϵ_c much less than unity and F_{pp} equal to zero. We then obtain

$$E_{sp} = A_p/A_s$$

The fraction r may be compared with the fraction F_{cp} of cone emission that reaches the patch within the cooler (i.e., without reflection from the space target). The result is

$$\frac{r}{F_{cp}} = \frac{(1-F_{cp})_{ps}\,\dfrac{A_p}{A_s}}{F_{cp}\left[1 - \left(1 - \dfrac{A_p}{A_s}\right)\rho_s\right]}$$

For the test cone, we have

$$F_{cp} = 0.025$$

$$\frac{A_p}{A_s} = \frac{1}{9}$$

Then, for ρ_s equal to 0.07, we obtain

$$\frac{r}{F_{cp}} = 0.32$$

If ρ_s is reduced to 0.02, this ratio is reduced to 0.088.

The design of the multielement radiant cooler is less sensitive than the test cone to reflections from the space target. First, the cone to patch coupling within the cooler is increased by smaller cone wall angles and multiple reflections. Secondly, the patch to cone wall area ratio is considerably larger.

2.5.2 Hemispherical Emissivity

The space chamber used for the experimental studies was modified to allow the measurement of the hemispherical emissivity of flat samples. The technique utilized is basically a calorimetric one in which the sample temperature is fixed. It is described in detail in Part II to the final report on Contract NAS5-11683 (8 April - 15 December 1969). The honeycomb liquid nitrogen target was modified to a shallow cylindrical cold cavity by the addition of a honeycomb skirt. A measuring plate or disk was constructed of aluminum foil and honeycomb. It was suspended from the cold cavity by means of two thermocouple leads and two additional support wires. The sample (cone wall) is attached to a temperature regulated baseplate. The sample base permits, the measurement of a wide range of wall sizes and shapes (Figure 2-8).

The basic equation of the experiment relates the emissivity of the sample (ϵ_1) to the measured temperatures of the sample (T_1), measuring plate (T_2), and cold cavity (T_3). For only radiative coupling between surfaces and for thermal equilibrium, the equation is (Section 2.0 of the above report).

$$\epsilon_1 = 0.95 \frac{T2^4 - T3^4}{T_1^4 - T_2^4}$$

This result holds for a low emissivity sample ($\epsilon_1 \ll 1$) and for honeycomb facing honeycomb between the disk and cavity. Both sides of the disk and the cavity are assumed to be covered with black paint whose emissivity is 0.91 (Section 2.5.1.1)

For T_1 = 300K and T_3 = 85K, T_2 = 121.5K when ϵ_1 = 0.02. The net power emitted (or received) by the disk is

$$\Phi_{2-3} = 0.95 \, (T_2^4 - T_3^4) \, \sigma A_2,$$

where A_2 is the high emissivity area of either side of the disk (the sides of the disk are covered with low-emissivity material as described in Part II of the final report on Contract NAS5-11683). The disk has a 1.50 inch diameter, so that for the above temperatures, it radiates a net thermal equilibrium power of 10.19 mW. If the supports are to conduct no more than 2 percent of this amount (corresponding to a 2 percent error in the emissivity measurement; Section 4.3 of the above report), their thermal conductance cannot exceed

$$K_W = \frac{2.04 \times 10^{-4}}{36.5} = 5.59 \times 10^{-6} W/K$$

A = POSITION OF BLACK DISK ABOVE BASE

B = THERMOCOUPLE SLOT

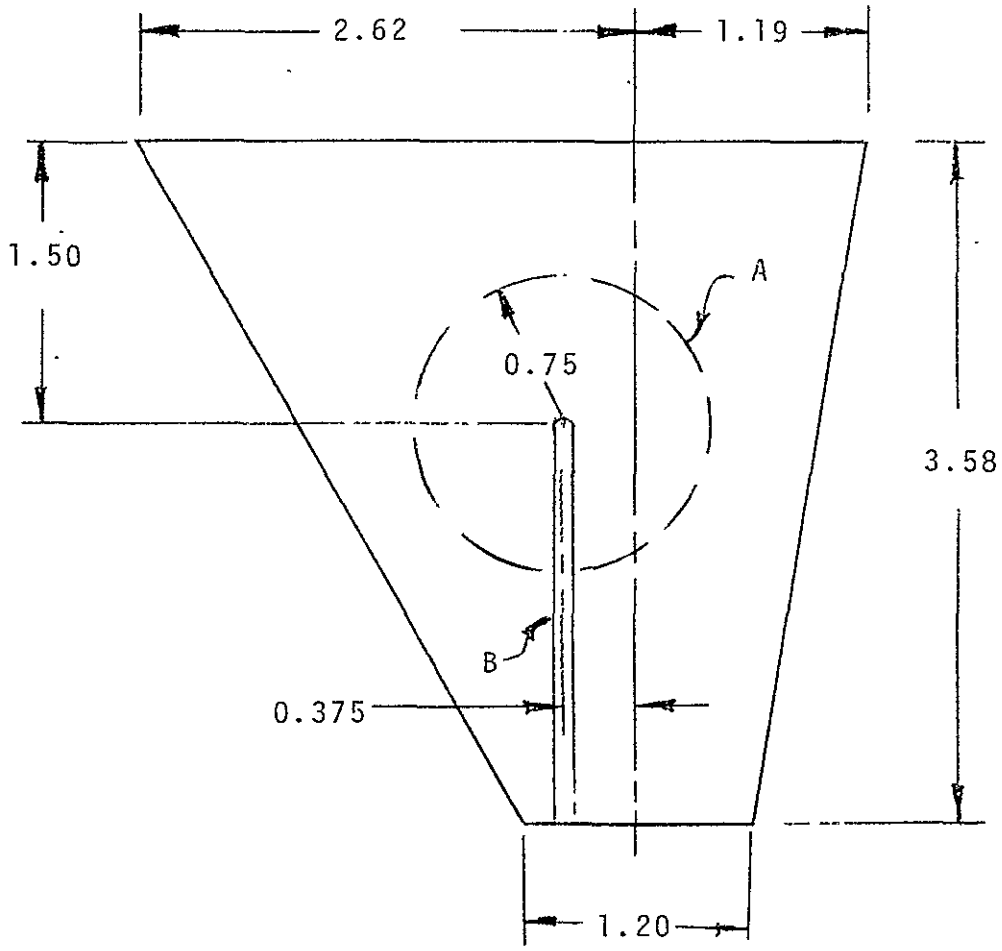

Figure 2-8 Cone Wall Base For Emissionmeter (Dimensions in Inches)

The support wires are all 2 inches long between the disk and cavity. They consist of three chromel and one constantan, all 3×10^{-3} inch in diameter. The resultant thermal conductance is 5.57×10^{-6} W/K.

Measurements were made on the following samples:

A. An aluminized hardcoated aluminum cone wall from the 45 degree test cone.

B. A sheet of smooth aluminized mylar used in multilayer insulation.

C. A plate of clean, mill-finished 6061 aluminum alloy.

The sample temperature (T_1) was measured with a copper-constantan thermocouple and a Leeds & Northrup temperature potentiometer (Cat. No. 8692). The measuring plate (T_2) and cold cavity (T_3) were measured with chromel-constantan differential thermocouples referenced to a liquid nitrogen bath. In addition, the temperature (T_4) of honeycomb skirt was measured with a differential thermocouple referenced to the main cold cavity.

Sample B was attached to an aluminum substrate by means of two-way tape. The temperature sensor for the sample was on the substrate. The measurements with this sample showed that the temperature of the measuring plate (and therefore the apparent sample emissivity) was a strong function of how well the sample was attached to the substrate. The aluminized surface apparently had a temperature below that of the sample as a result of the thermal resistance across the tape and mylar. The measurements on sample B are therefore not reported.

The measured equilibrium temperatures and calculated emissivities are given in Table 2-28 for samples A and C.

Table 2-28

Hemispherical Emissivity Measurements

Sample	T_1	T_2	T_3	T_4	G_1
A	295.0	122.9	87.4	112.2	0.022
C	296.4	164.5	88.5	112.9	0.091

All temperatures in kelvins.

The large difference between the hemispherical emissivity (0.022) of the test cone wall and the effective emissivity (0.047) in a cooler configuration is explained in Section 2.8.

2.6 Analysis of Emissivity Measurements

The large ratio of effective cone wall to hemispherical emissivity in the 45 degree test cone can be explained (at least for the most part) by:

a. An increase produced by directional effects (Section 1.2.1).

b. An increase produced by a diffuse component of reflection (Sections 1.2.2 and 2.6.2).

c. An apparent increase produced by a non-black space target (Section 2.5.2.2).

2.6.1 Estimate of Emissivity Increase

The test cone had a temperature of about 290K (Section 2.5.1). The representative wavelength λ is therefore about 15 times the visible wavelength λvis used to measure surface flatness and irregularity (i.e., λ is about 8.8 μm). The ratio of rms roughness to wavelength for cone wall radiation is then (Section 1.2.2)

$$\frac{\sigma}{\lambda} \qquad \frac{(\sigma_{pp}/\lambda_{vis})}{30\sqrt{2}}$$

where ($\sigma_{pp}/\lambda_{vis}$) is the surface irregularity in visible wavelengths. The test cone walls have a flatness of about 17 wavelengths and an average irregularity of about 2.5 wavelength.
We then have

$$\frac{\sigma}{\lambda} = 0.059$$

From Section 1.2.2, the resultant fraction of diffuse reflectivity at the representative wavelength is

$$g = 1 - \exp\left[-\left(\frac{4\pi\sigma}{\lambda}\right)^2\right] = 0.423$$

From Section 2.6.2, the increase in effective specular cone wall emissivity over hemispherical emissivity is then approximately

$$1 + 0.336g = 1.14$$

In the test cone, the patch sees the cone at angles from 45 degrees to 90 degrees from the wall normals. The directional properties of a metallic reflector then result in an increase in emissivity over the hemispherical value by a factor of about 1.24 (Section 1.2.1).

Finally, the non-black space target used in the measurements on the test cone increased the apparent wall emissivity (i.e., the cone-patch radiative interchange) by a factor of about 1.32 (Section 2.5.2.2). The overall increase in wall emissivity compared with the hemispherical value is then

$$1.14 \times 1.24 \times 1.32 \cong 1.87$$

The measured hemispherical emissivity of a test cone wall is 0.022 (Section 2.5.2). The apparent (effective) test cone emissivity would then be $1.87 \times 0.022 \cong 0.041$. This is reasonably close to the measured value of 0.047 (Section 2.5.1).

2.6.2 Sensitivity of Cone Designs to Diffuse Reflection

The preliminary experimental determination of the effective cone wall emissivity ϵ_c in a 45 degree test cone is described in Section 2.5.1. The upper limit to ϵ_c was estimated to be 0.048 for vacuum deposited aluminum. The average surface flatness of the nickel plated walls was about 17 wavelengths of visible light. To obtain a comparable performance in the radiant cooler cones for the SCMR and ATS-F VHRR in terms of the level of diffuse reflectance requires a finer optical finish (~8 wavelengths). The test cone is less sensitive to deviations from specular reflectance because of the larger view to cold space from the cone walls. On the other hand, the multi-element radiant cooler (MERC) has a view from the cone to space nearly as large as the test cone. As a result, the surface finish required for the same performance is comparable to that of the test cone (~15 wavelengths).

The test cone is more sensitive than the other three designs to directional emissivity effects (Section 1.2.1). Incidence angles at the cone walls for patch radiation are limited to the range from 45 degrees to 90 degrees in the test cone. On the other hand, patch rays in the other design either go down to or approach normal incidence (10 degrees, 7.5 degrees, and 0 degrees). Thus cone walls finished to obtain the same cooler specularity as in the test cone should result in a lower value of ϵ_c because of the decrease in average cone wall incidence angle.

A non-specular component of reflection at the cone walls increases the apparent specular emissivity ϵ_c, as discussed in Section 1.2. We will approximate the non-specular component as pure diffuse (Lambertian). Based on the specular model used in the experimental analysis, the presence of patch radiation returned to the patch and the increase in patch radiation absorbed in the cone walls as a result of diffuse reflectivity are both interpreted as increases in ϵ_c. For diffuse reflection at the cone walls, the increase is

$$M = 1+(1-\epsilon_h)\, f + (1-\epsilon_h)^2 \cdot f^2 + \cdot = \frac{1}{1-(1-\epsilon_h)\, f}$$

where ϵ_h is the hemispherical emissivity and f the fraction of patch radiation diffusely reflected at the cone walls that does not reach the space target (cone mouth).

The fraction f is given by

$$f = F_{cc} + F_{cp} = 1 - F_{cs},$$

where

F_{ij}	=	view factor from i to j
c	=	cone walls
p	=	patch opening
s	=	visible space target (cone mouth).

Using the relationships (reciprocity and sum of view factors equals unity)

$$F_{cs} = \frac{A_s}{A_c} F_{sc}$$

$$F_{sc} = 1 - F_{sp}$$

$$F_{sp} = \frac{A_p}{A_s} F_{ps},$$

this becomes

$$1 - F_{cs} = \frac{1}{A_c} (A_c - A_s - A_p F_{ps}),$$

where A_k is the area of surface k.

For ϵ_h much less than unity, we have

$$M = \frac{1}{1-f} = \frac{1}{F_{cs}}$$

Neglecting directional effects, a hemispherical emissivity ϵ_h on a cone wall surface at which a fraction g of the reflection is diffuse, then results in an effective specular emissivity given by

$$\epsilon_c = \epsilon_h \left[(1-g) + \frac{g}{F_{cs}} \right]$$

Note that for $F_{cs} = 0$, $f = 1$, and $M - \frac{1}{\epsilon_h}$. This is the limiting case of maximum sensitivity to diffuse reflectance (R.V. Annable, Appl, Opt. 9, 185, Section IV). We then have $\epsilon_c = \epsilon_h (1-g) + g$ or $\epsilon_c = \epsilon_h + g$ for g much less than one. The values of $1/F_{cs}$ are given in Table 2-29 for the test cone (TC) and for the other three cooler designs.

Table 2-29

Apparent Cone Wall Emissivity

Increase Produced by Diffuse Reflection

Cone Design	$\frac{1}{F_{cs}}$	Compared With TC
TC	1.366	1
SCMR	2.515	1.841
ATS-F	2.602	1.905
MERC	1.445	1.058

The design values for the test cone are

$$\frac{A_s}{A_c} = \frac{9}{8\sqrt{2}}$$

$$\frac{A_p}{A_c} = \frac{1}{8\sqrt{2}}$$

$$F_{ps} = 0.7173$$

The design values for the other cooler designs were taken from their respective design study reports. The factor F_{ps} is equal to the factor $F_{p-m}(0)$ given in the reports.

The SCMR and ATS-F designs are considerably more sensitive to a diffuse component of reflection than the TC and MERC designs. To obtain the value of ϵ_c obtained in the test cone, it is necessary to maintain the value of $[(1-g) + \frac{g}{F_{cs}}]$ constant by reducing g. The fraction g of diffuse reflection can be related to the surface finish on the cone walls by (See Section 1.2.2).

$$g = 1 - \exp\left[-(4\pi\sigma/\lambda)^2\right]$$

where

σ = rms deviation of surface from its mean surface limit (roughness)

λ = wavelength of radiation

In general, the argument of the exponent is much less than unity, so that the right side of the equation may be expanded to give

$$g = 1 - [1 - (\frac{4\pi\sigma}{\lambda})^2 + \frac{1}{2} (\frac{4\pi\sigma}{\lambda})^4 - \cdots]$$

$$g = (\frac{4\pi\sigma}{\lambda})^2 \cdots$$

The required surface finish (as measured by σ) is then proportional to the square root of g. We may assume a linear relationship between σ and the surface flatness (ibid). The resultant surface finishes needed in the other designs for an effective emissivity equal to that of the test cone are listed in Table 2-30. It is assumed that directional effects are not present and that the evaporated materials have the same properties.

Table 2-30

Required Surface Flatness

For Equal Values Of Effective

Wall Emissivity

Design	$(g/gTC)^{1/2}$	Surface Flatness (Visible Wavelengths)
SCMR	0.492	~ 8
ATS-F	0.477	~ 8
MERC	0.907	~15

In the above analysis, we did not distinguish between diffusely reflected radiation going to the patch and going to the cone. In addition, we did not account for multiple reflections in the case of specular wall reflection. These refinements have little effect on the calculations for the test cone in which the view factor from cone to patch is very small and in which there are no multiple specular reflections.

For specularly reflecting cone walls, the radiative coupling factor between the patch and cone is

$$\epsilon_{pc} = 1 - F_{p-m} (n) (1-\epsilon_h)^n$$

where

$F_{p-m(n)}$ = view factor from patch to images of cone mouth formed by n specular wall reflections

ϵ_h = hemispherical emissivity of cone walls.

For $\epsilon_h^2 \ll 1$, we have

$$(1 - \epsilon_h)^n = 1 - n\,\epsilon_h + \frac{n(n-1)}{2}\,\epsilon_h^2 - \cdots$$

And for $\epsilon_h\,(n-1) \ll 2$, i.e., $\epsilon_h \ll 1$ when $n \ll 3$, this becomes

$$(1 - \epsilon_n)^n = 1 - n\,\epsilon_h.$$

Then, using

$$\sum F_{p-m(n)} = 1,$$

we obtain

$$S = \frac{\epsilon_{pc}}{\epsilon_h} = \sum nF_{p-m\,(n)}$$

Values of this ratio are given in Table 2-31for the four radiant cooler designs of interest.

Table 2-31

Ratio of Effective to Hemispheric Emissivity for Specular Reflection

Design	$F_{p-m(1)}$	$F_{p-m(2)}$	$\sum nF_{p-m(n)}$
TC	0.2827	0	0.2827
SCMR	0.5078	0.1691	0.8460
ATS-F	0.5170	0.1613	0.8396
MERC*	0.3653	0.673	0.4999

*Total patch opening.

The view factors from the patch to space (cone mouth) and from the patch to cone are listed in Table 2-32.

Table 2-32

View Factors from the Patch

Design	$F_{ps}=F_{p-m(0)}$	$F_{pc}=1-F_{ps}$
TC	0.7173	0.2827
SCMR	0.3231	0.6769
ATS-F	0.3217	0.6783
MERC	0.5674	0.4326

For diffusely reflecting cone walls, we will first consider the fraction of patch radiation absorbed in the cone walls (i.e., the patch-cone radiative coupling factor). It is given by

$$\epsilon_{pc} = \epsilon_h F_{pc} [1+(1-\epsilon_h)F_{cc} + (1-\epsilon_h)^2 F_{cc}^{\ 2} + \cdots]$$

$$= \frac{\epsilon_h F_{pc}}{1-(1-\epsilon_h) F_{cc}}$$

where F_{cc} is the view factor from the cone to itself. For $\epsilon_h \ll 1$, we obtain

$$D = \frac{\epsilon_{pc}}{\epsilon_h} = \frac{F_{pc}}{1-F_{cc}}$$

Secondly, consider the patch radiation returned to the patch as a result of diffuse reflection at the cone walls. The fraction is given by

$$r = F_{pc} \cdot F_{cp} [1+(1-\epsilon_h) F_{cc} + \cdots]$$

$$r = \frac{F_{pc} F_{cp}}{1-(1-\epsilon_h)F_{cc}}$$

For $\epsilon_h \ll 1$, this becomes

$$r = \frac{F_{pc} \cdot F_{cp}}{1 - F_{cc}}$$

Values of the view factors are given in Table 2-33 together with 1-r, the efficiency of patch emission in the presence of diffusely reflecting cone walls.

Table 2-33

Efficiency of Patch Emission
for Diffuse Cone Reflection

Design	F_{pc}	F_{cp}	$F_{pc} \cdot F_{cp}$	1-r	F_{cc}
TC	0.2827	0.02499	0.007065	0.99067	0.2429
SCMR	0.6769	0.04901	0.03317	0.92573	0.5534
ATS-F	0.6783	0.05593	0.03794	0.91381	0.5598
MERC	0.4326	0.1472	0.06368	0.92414	0.1606

If the radiative input to the patch from the cone is much larger than the sum of all other thermal loads, the degradation factor produced by diffuse cone wall reflection becomes D/S (1-r). The values of this ratio are given in Table 2-34.

Table 2-34

Degradation Factor
for Cone Wall Radiative
Coupling

Design	D/S (1-r)
TC	1.333
SCMR	1.935
ATS-F	2.008
MERC	1.116

It is seen that the ratio for the test cone (TC) is very nearly the same as that given in Table 1 (1.366). The values are lower for the other designs. However, thermal inputs to the patch other than cone wall radiation are generally not negligible compared with wall radiation. The two degradations produced by diffuse wall reflection cannot then be combined into a single factor.

Finally, diffuse cone wall reflection can produce a coupling between external sources and the cold patch that is not present for specular reflection. This is an especially important consideration when direct sunlight irradiates the cone mouth as in the ATS-F cooler during about 2 months of the year. The external thermal loads are generally simulated by heaters during cooler tests. A separate chamber test is therefore necessary to determine the source-patch coupling produced by non-specular reflections in a given cooler cone (See Section 2.2).

3.0 NEW TECHNOLOGY

No items which are considered new technology according to NASA form 1162 were developed during the second phase of the contract. However, the dual patch arrangement reported in the first phase (Design of A Dual Patch Multi-Element Radiant Cooler, July 1970, Section 8.0) was reduced to practice.

4.0 RECOMMENDATIONS

Based on the results of this program, we recommend that improvements be made to increase the accuracy and confidence level of the thermal testing of both radiant coolers and separate radiative components. Specifically, we recommend that (See Sections 2.2.4, 2.3.3, 2.6, and 1.2.2)

A. The cold targets used in thermal tests be designed to have an infrared absorptivity greater than 0.99.

B. The diffuse reflectivity of the inner cone walls be experimentally determined for both infrared and solar radiation.

A cavity that has a length to opening ratio of at least one and that has walls of 30 degree v-grooves or of honeycomb arrays will have an absorptivity greater than 0.99 when its surfaces are covered with black paint (See Final Report, Part II, on Contract NAS5-11683, 8 April - 15 Dec. 1969, Section 1.3). In general, this will require additional space within the test chamber. The measurements of diffuse reflectivity could be done on separate cone walls or on the assembled cooler. The values are needed to determine the indirect patch to external source coupling produced in orbit by the non-specular component of reflectivity. Such measurements can then be used to increase the accuracy of chamber simulation of orbital operation.

The accuracy of the tests on both the radiant cooler (Section 2.1) and the thermal components (Sections 2.4 and 2.5) was limited by the non-black space target (Sections 2.3.3 and 2.6). In the case of the cooler tests, the errors produced by the space target were at least partially offset by the absence of the indirect patch to earth coupling produced by the non-specular component of cone wall reflection (Section 2.2.4). Improvements are needed in these areas, as discussed in Section 4.0.

5.0 CONCLUSIONS

The construction and test phase of the dual patch, multi-element radiant cooler project was generally successful. Conservatively, we could expect to operate in orbit with the 14 element InAs array in the temperature range from 115 to 120K and the 4 element HgCdTe array in the range from 95 to 100K. Initial performance (Section 2.1) was limited by the radiative insulation of the cone and second patch. The insulation of patch 2 was improved by providing a shield that operated at the temperature of patch 1. Rather than attempt to improve the insulation factor of the cone blanket, it may be better to thermally isolate the cooler housing from the main instrument structure and thus provide a generally cooler environment (See, for example, Final Report, Part I, on Contract NAS5-10113, 1 Dec. 1967, Section 2.1.2).

The construction and test of the dual patch cooler were realistic. Vibration tests on the patch assembly showed that the (thermally) critical mechanical assembly was sound (Section 1.1). Electrical and optical connections (with their attendant thermal paths) were provided to both patches. The in-orbit thermal load on the cone was simulated with a heater (Section 2.3.2). The construction and test included provisions for anti-frost devices and techniques (Section 1.3). And finally, any indirect, in-orbit coupling between the patches and external sources produced by a diffuse component of cone wall reflection (Section 2.2.4) was more than compensated for by the non-black space target (Section 2.3.3).

The study of anti-frost requirements showed that the period of unimpaired operation (i.e., time between decontaminations) would be limited by contamination from the spacecraft atmosphere in a properly constructed and properly operated radiant cooler. Loss of signal estimates were based on the absorption coefficients of ice in the wavelength regions of interest.

Both theoretical (Sections 1.2.2 and 2.2.4) and experimental (Sections 2.2 and 2.5) evidence point to the need for optically finished cone walls. Highly specular walls are needed to reduce the direct cone to patch coupling and the indirect earth to patch coupling. The optically finished cone had an effective specular emissivity in the vicinity of 0.04 (Sections 2.2, 2.5, and 2.6).

Separate tests on radiative insulation (Section 2.4) showed that the insulation factors of 60 to 65 obtained for the cone and first patch are about the best that can be expected within the constraints imposed by the cooler construction. The insulation blankets have large end areas that are thermally coupled to the surroundings and thereby reduce the effectiveness of the entire blanket. The tests also showed that radiative decoupling using close-spaced, low-emissivity surfaces of emissivity ϵ provides the theoretically expected insulation factor of $2/\epsilon$. Such surfaces therefore provide insulation factors equal to or greater than those of a multilayer blanket (again, within the constraints of the cooler structure).

APPENDIX

SPECIFICATION FOR COOLER CONE WALL PROCESSING

APPLICATION	
NEXT ASSY	USED ON
	61202

REVISIONS			
LTR	DESCRIPTION	DATE	APPROVED

"EXCEPT AS MAY BE OTHERWISE PROVIDED BY CONTRACT, THESE DRAWINGS AND SPECIFICATIONS ARE THE PROPERTY OF ITT AEROSPACE/OPTICAL DIVISION, ARE ISSUED IN STRICT CONFIDENCE, AND SHALL NOT BE REPRODUCED, OR COPIED, OR USED AS THE BASIS FOR THE MANUFACTURE OR SALE OF APPARATUS WITHOUT PERMISSION."

SHEET SIZE																									
REV LETTER																									
SHEET NO.	1	2	3	4	5	6	7	8	9	10	11	12	13	14	15	16	17	18	19	20	21	22	23	24	25

UNLESS OTHERWISE SPECIFIED DIMENSIONS ARE IN INCHES AND INCLUDE CHEMICALLY APPLIED OR PLATED FINISHES DO NOT SCALE PRINT

TOLERANCES

DECIMALS		ANGLE
2 PLACE	3 PLACE	
±.02	±.010	±½°

CONTRACT NO.
NAS5-21132

APPROVALS

DRAWN	
CHECKED	
ENGR	4/6/70
ITTAOD	
OTHER	

ITT AEROSPACE/OPTICAL DIVISION
FORT WAYNE, INDIANA, U.S.A.
INTERNATIONAL TELEPHONE AND TELEGRAPH CORPORATION

SPECIFICATION FOR COOLER CONE WALL PROCESSING

SIZE	CODE IDENT NO.	
A	31550	8116057
SCALE		SHEET 1 of 3

FORM NO. FW ITTAOD D 101

A-2.

LINCOLN-GRAPHIC CORP. 10 5155 1M 4-70

DRAWINGS AND SPECIFICATIONS ARE THE PROPERTY OF ITT AEROSPACE/OPTICAL DIVISION, ARE ISSUED IN STRICT CONFIDENCE, AND SHALL NOT BE REPRODUCED, OR COPIED, OR USED AS THE BASIS FOR THE MANUFACTURE OR SALE OF APPARATUS WITHOUT PERMISSION."

1.0 GENERAL

This specification covers the processing of cone wall sections to be optically finished for cone wall tests. The general process envisioned consists of 5 steps

1. Machining the wall pieces
2. Rough polishing of reflective surface
3. Plating of electroless Nickel (Kanigen® or equivalent)
4. Optical polishing of reflective surface
5. Evaporative coating of reflective layer

The reflective surface is the inner cone wall when the pieces are assembled. This is called out on each drawing.

The goal of this process is to produce an assembled cone that has an extremely low scatter polished surface with high reflectivity. Extreme care will be exercised to protect the surface finish after polishing and reflective coating. Cone assembly will be done by ITT-A/OD.

2.0 APPLICABLE DOCUMENTS

2.1 MIL-I-45208A, "Inspection System Requirements".

2.2 GSFC Spec S-320 - ATS-2, "Environmental Test Specification for Components and Experiments".

2.3 This specification.

3.0 REQUIREMENTS

3.1 Mechanical

3.1.1 Each cone assembly consists of 3 pieces. Each piece is one wall of the cone. The material will be 6061 aluminum processed for stress relieving.

3.1.2 After the wall pieces are machined, the reflective surface will be ground (optical rough polished) to .0002" TIR. The purpose of this step is to provide a flat surface for electroless nickel application to eliminate chance of polishing thru the Ni.

3.1.3 Each piece will be overcoated with a layer of electroless nickel (Kanigen® or equivalent) thick enough to preclude polishing thru to the substrate. Electroless Nickel will be applied over the entire surface of each piece.

REV
DRAWING NUMBER 8 6057
"EXCEPT AS MAY BE OTHERWISE PROVIDED BY CONTRACT, THESE DRAWINGS AND SPECIFICATIONS ARE THE PROPERTY OF ITT AEROSPACE/OPTICAL DIVISION, ARE ISSUED IN STRICT CONFIDENCE, AND SHALL NOT BE REPRODUCED, OR COPIED, OR USED AS THE BASIS FOR THE MANUFACTURE OR SALE OF APPARATUS WITHOUT PERMISSION."

3.2 Optical

3.2.1 The reflective surface of each piece will then be optically polished to provide an extremely low scatter microfinish. The flatness of the polished side will be to within 5 wavelengths of visible light (10 fringes) over any 2 inch diameter area.

3.2.2 Edge roll off will be limited to within less than 1/16" of the edge.

3.2.3 A highly reflective durable coating of aluminimum will be evaporated onto reflective surface of each piece. No protective overcoat will be applied. The reflectivity of the surface will be .90 or greater at 5500 Å. The reflectivity of one piece in each vacuum run will be measured and supplied to ITT-A/OD. A witness plate processed with each batch may be used for measurements applying to that batch.

3.2.4 There will be no scratches (including hairline scratches), fingerprints, or other defects on the polished surface when viewed with a 10X microscope. There will be no more than 5 pits or digs on each polished surface.

4.0 DOCUMENTATION

The manufacturer shall provide documentation containing the results of all tests and inspections performed on each unit. Data required to comply with Section 3 shall also be provided.

5.0 PREPARATION FOR DELIVERY

Shipping containers shall be entirely suitable to protect each unit shipped during the handling, shipment and storage periods. Packaging and shipment shall conform to "best commercial practices".

VENDOR ACCEPTANCE TEST DATA REPORT

Specification Paragraph No.	Specification Measurement	Part Measurement
3.1.3	Electroless nickel not polished thru	
3.2.1	≤ 10 fringes	
3.2.2	≤ 1/8" on 3 sides; ≤ 1/16" on short side	
3.2.4	View with 10X microscope	

ITT AEROSPACE/OPTICAL DIVISION
FORT WAYNE, INDIANA, U.S.A.
INTERNATIONAL TELEPHONE AND TELEGRAPH CORPORATION

DWG	CODE IDENT NO.	
A SIZE	31550	8116057
SCALE		SHEET 3 of 3